RAIN–WIND-INDUCED CABLE VIBRATION THROUGH WIND TUNNEL TESTS AND NUMERICAL ANALYSIS

JING HAIQUAN

Ph.D

The Hong Kong Polytechnic University

2016

The Hong Kong Polytechnic University

Department of Civil and Environmental Engineering

Rain–Wind-Induced Cable Vibration through Wind Tunnel Tests and Numerical Analysis

Jing Haiquan

A thesis submitted in partial fulfillment of the requirements for the

degree of Doctor of Philosophy

May 2016

DECLARATION

I hereby declare that this dissertation entitled "***Rain−Wind-Induced Cable Vibration through Wind Tunnel Tests and Numerical Analysis***" is my own work and that, to the best of my knowledge and belief, it reproduces no material previously published or written, nor material that has been accepted for the award of any other degree or diploma, except where due acknowledgement has been made in the text.

_____

Signed

Haiquan JING

To My Family

ABSTRACT

The large vibration of stay cables has been observed in many cable-stayed bridges under the simultaneous occurrence of rain and wind, which is referred to as rain−wind-induced vibration (RWIV). The RWIV has become a great concern to bridge engineering and wind engineering communities over past three decades. Although extensive researches have been conducted to investigate the RWIV through field measurements, wind tunnel tests, and theoretical analyses, the excitation mechanism of the RWIV remains unclear and many divergences and debates exist. The wind tunnel test is an effective method to investigate the excitation mechanism of the RWIV because many parameters such as the wind speed and direction could be well controlled. In this thesis, the RWIV is investigated in detail through wind tunnel testing and numerical analysis, aiming to better understand the excitation mechanism of the RWIV.

RWIV of a cable model with the external diameter of 160 mm was successfully reproduced in a wind tunnel using simulated water rivulets. The effects of different parameters such as the wind speed, rivulets, and damping ratio on the RWIV have been investigated. The wind speed in the wake field of the stationary cable model was measured to study the effect of water rivulets on the wake flow.

The digital image processing technique is developed to identify the rivulet's

movement and thickness during the RWIV for the first time. The cable displacement is also extracted simultaneously. The relationship between the cable vibration and rivulet oscillation is thus obtained and investigated.

A numerical model is derived based on the quasi-static assumption using the measured upper rivulet information. Numerical analyses are conducted using the aerodynamic force coefficients measured by Prof. Y.L. Xu and other researchers considering the three dimensionality of the cable geometry. The numerical results are compared with the wind tunnel testing results.

From the obtained rivulet information and cable vibration, a new excitation mechanism of the RWIV is proposed based on the interaction between the upper rivulet, air boundary layer, and cable vibration. When the cable vibrates upward, the upper rivulet, as an obstacle, changes the cable's cross-section and induces the air boundary layer to asymmetrically attach on the upper side of the cable, generating the significant upward aerodynamic force. The aerodynamic force excites the cable to vibrate at large amplitude. The large cable vibration, in turn, changes the attacking angle of the wind and provides inertial force on the upper rivulet, exciting the upper rivulet to steadily and circumferentially oscillate on the cable surface. Besides, the cable vibration also enhances the coherence of the upper rivulet along the cable and harmonizes the attachment of the air boundary layer along the cable, resulting in a larger resultant force on the cable. Finally, a single degree of freedom numerical model is established to verify the proposed excitation mechanism and an energy-based criterion is developed to predict the steady amplitude of the RWIV.

PUBLICATIONS

Journal Papers:

Jing Haiquan, Xia Yong, Li Hui, Xu Youlin and Li Yongle (2015). "Study on the role of rivulet in rain–wind-induced cable vibration through wind tunnel testing", *Journal of Fluids and Structures,* Volume: 59, Pages: 316-327. (JCR: 1, IF: **2.021**)

Jing Haiquan, Xia Yong, Xu Youlin and Li Yongle (2015). "Measurement of rivulet movement and thickness on inclined cable using videogrammetry", *Smart Structures and Systems*. (accepted) (JCR: 2, IF: **1.368**)

Li Yongle, **Jing Haiquan**, Xia Yong and Xu Youlin (2015). "Measurement of rivulet movement on inclined cables during rain-wind induced vibration", *Sensors and Actuators: A Physical*, Volume: 230, Pages: 17–24. (JCR: 1, IF: **1.903**)

Jing Haiquan, Xia Yong, Li Hui, Xu Youlin and Li Yongle (2015). "Study on the excitation mechanism of rain-wind induced cable vibration in wind tunnel", *Journal of Fluids and Structures*. (In review) (JCR: 1, IF: **2.021**)

Li Hui, Laima Shujin and **Jing Haiquan** (2014). "Reynolds number effects on aerodynamic characteristics and vortex-induced vibration of a twin-box girder", *Journal of Fluids and Structures*, Volume: 50, Pages: 358–375. (JCR: 1, IF: **2.021**)

Conference Papers:

Jing Haiquan, Xia Yong, Li Yongle, Xu Youlin and Xiang Huoyue (2014). "Experimental study on the role of rivulets in rain-wind induced cable vibration", *Symposium on the Dynamics and Aerodynamics of Cables*, Lyngby, Denmark, September 25-26.

Jing Haiquan, Xia Yong, Li Yongle, Xiang Huoyue and Xu Youlin (2014). "Measure the rivulet movement using digital image processing technic in wind tunnel tests", *5th Asia-Pacification Workshop on Structural Health Monitoring*, Shenzhen, China, December 4-5.

Xia Yong, **Jing Haiquan** and Xu Youlin (2015). "Measurement of rivulet movement on inclined cables using digital image processing", *7th Internationl Conference on Structural Health Monitoring of Intelligent Infrastructure*, Torino, Italy, July 1-3.

ACKNOWLEDGMENT

CONTENTS

LIST OF FIGURES

LIST OF TABLES

A^k matrix of the *k*-th grayscale image without background

A_0^k matrix of the *k*-th grayscale image with background

A_j^k vector the *j*-th column of A^k

c column number of the reference point

C damping force coefficient

c_r possibility of the upper rivulet's formation

c_u uniform coefficient

c_θ amplitude ratio of the rivulet oscillation to the cable vibration

C_l, C_d lift and drag force coefficients, respectively

$C_{L,\max}$ maximal lift force

C_T scale factor of the rivulet thickness

D diameter of the cable

E total input work to the cable

E_a input work done by the aerodynamic forces to the cable

E_L, E_D input work done by the lift and drag forces to the cable, respectively

E_S energy consumed by the damping

f fundamental frequency of the cable

f_s frequency of vortex shedding

F_G	gravity
F_G^t, F_G^n	tangent and radial components of the upper rivulet's gravity, respectively
F_l, F_d	lift and drag forces, respectively
F_l^r, F_d^r	lift and drag forces of the upper rivulet, respectively
F_v, F_h	resultant forces in the vertical and horizontal directions
g	acceleration of gravity
h	height of the upper rivulet
H	relative grayscale intensity of the rivulet
I^k	matrix of the k-th digital image
I_R^k	matrix of the reference area of the k-th image
K	stiffness of the spring
l	width of the upper rivulet
l_c	clear spacing between the cables
m	cable mass per unit length
P_u, P_l	wind pressure on the upper and lower rivulets, respectively
Q	flow rate of the water rivulet
r	row number of the reference point
R	cable radius
R_e	Reynolds number
$RL(k, j)$	rivulet location at the j-th colum of the k-th image
S	cross-sectional area of the real rivulet
S_m	cross-sectional area of the measured rivulet

S_t	Strouhal number
S_u, S_l	reaction of the on the upper and lower rivulets, respectively
T	period of the cable vibration
T_r	thickness of the upper rivulet
U	incoming wind speed
U_N	relative wind speed normal to the cable axis considering the cable and rivulet vibrations
U_{N0}	wind speed normal to the cable axis
U_{rel}	resultant wind speed considering the cable and rivulet vibrations
U_{crit}	critical wind speed
V	flow speed of the rivulet
y	cable displacement
Y	cable vibration amplitude
α, β	inclined and yawed angles
β^*	effective yawed angles
γ_u, γ_d	upstream and downstream contact angle, respectively
ΔA^k	difference between the k-th and (k-1)-th grayscale images
ΔA_j^k	vector of the j-th column of ΔA^k
Δp	target moving pixel in the image
Δy	moving distance of the cable
δ_D	coefficient of Den Hartog
θ	rivulet angle

θ_0 Initial or neutral rivulet angle

θ_r relative rivulet angle

θ_r^d dynamic component of the relative rivulet angle

θ_s rivulet angle from the stagnation point

θ_v dynamic rivulet angle

ξ_{ae} aerodynamic damping ratio

ξ_s structural damping ratio

ξ_t total damping ratio

ρ density of the air

ρ_w density of the water

φ attacking angle considering the cable and rivulet vibrations

φ' total attacking angle induced by the cable and upper rivulet vibrations

φ_0 attacking angle

φ_y attacking angle induced by the cable vibration

φ_θ attacking angle induced by the rivulet vibration

ϕ phase difference between the upper rivulet and cable vibrations

Ψ, Ψ^* occurrence function of the air boundary layer attachment

ω circular frequency of the cable

CHAPTER ONE

INTRODUCTION

1.1 Background

To meet the needs of modern transportation system, many long-span bridges have been built around the world in the past three decades. Cable-stayed bridge is one of the most common long-span bridge types. It has the advantages when the span ranges from 300 m to 1000 m. In general, a cable-stayed bridge mainly contains three components as Figure 1-1 shows:

1. A girder system with the bridge deck;
2. Cables supporting the girder; and
3. Towers supporting the cable system.
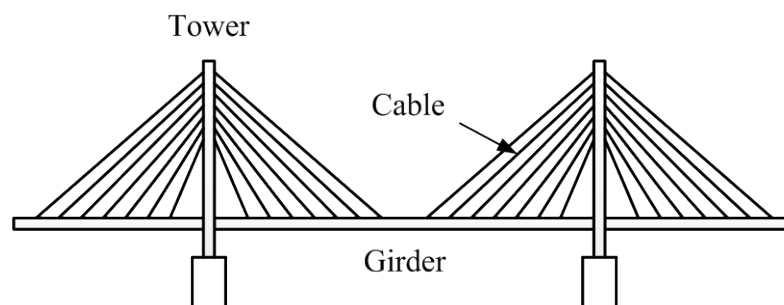
Figure 1-1. Sketch of a cable-stayed bridge

The cable system plays the critical role in the cable-stayed bridge. It connects the tower and main deck, transferring the load of the main deck to the tower. It is important to ensure the stay cables working at a stable and safe state. However, given

their inherent characteristics of low damping and great flexibility, the stay cables are prone to large vibrations caused by external excitations, such as wind, rain, vehicles, and anchorage motion. Very large amplitude vibration has been observed in stay cables of many cable-stayed bridges on condition of simultaneous occurrence of rain and wind, which is referred as rain−wind-induced vibration (RWIV) in this study. Such a large amplitude vibration may cause severe damage, such as the reduction of the cable's life, destruction of the connections, breakdown of the protection, and damage of the dampers (Pacheco and Fujino 1993; Poston 1998). RWIV has become a worldwide concern over decades to bridge engineering and wind engineering. Extensive researches through field measurement, wind tunnel test, and numerical analysis have been conducted to study the RWIV and to solve this problem. The response characteristics and on-set conditions of the RWIV have been investigated. The RWIV has been widely reported as an amplitude- and velocity-restricted and large amplitude vibration at low frequency. The wind speed and direction conditions have also been well investigated. However, the excitation mechanisms of the RWIV of cables are still not very clear.

Among these studies, the upper rivulet has been widely reported to be crucial to the RWIV. However, the precise characteristics of the upper rivulet oscillation and the geometric size remains unclear because the rivulet is considerably small, thin, and sensitive to wind flow and thus difficult to accurately measure.

1.2 Research Objectives

Being motivated by the shortage of referable rivulet information and the distinct divergence in the existing excitation mechanisms, this study aims at better

understanding the excitation mechanism of the RWIV, especially how the little rivulet exactly excite the large cable vibration.

The above goal will be achieved through the following approaches:

(1) Reproducing the RWIV with controllable rivulets in a wind tunnel to investigate the effects of different parameters on the RWIV;

(2) Developing a digital image processing technique to measure the rivulet when the RWIV occurs;

(3) Investigating the characteristics of the obtained rivulet and analyzing its relation to the cable vibration;

(4) Proposing an excitation mechanism based on the obtained rivulet information and the relationship between the rivulet and the cable vibrations.

(5) Establishing a numerical model to verify the proposed excitation mechanism.

1.3 Thesis Organization

This thesis is organized as Figure 1-2 shows. Chapter Two summaries the extensive literature related to the RWIV, including those on the dry cable galloping. The wind tunnel tests conducted in the present study are introduced in Chapter Three. A digital image processing technique is developed in Chapter Four to enable the measurement of the rivulet during the RWIV. The characteristics of the rivulet movement and thickness are investigated in this chapter. The relationship between the rivulet and cable vibrations is analyzed in detail in Chapter Five. A numerical model is derived based on the quasi-static assumptions using the measured rivulet information in Chapter Six. Numerical analyses are then conducted and compared with the wind tunnel tests. Based on the obtained rivulet information in Chapters Four and Five, a

new excitation mechanism of the RWIV is proposed in Chapter Seven. To verify the

proposed excitation mechanism of the RWIV, a single degree of freedom numerical

model is established and an energy-based criterion is developed to predict the steady

amplitude of the RWIV in Chapter Eight. Finally, Chapter Nine concludes the thesis

and discusses the possible future research.
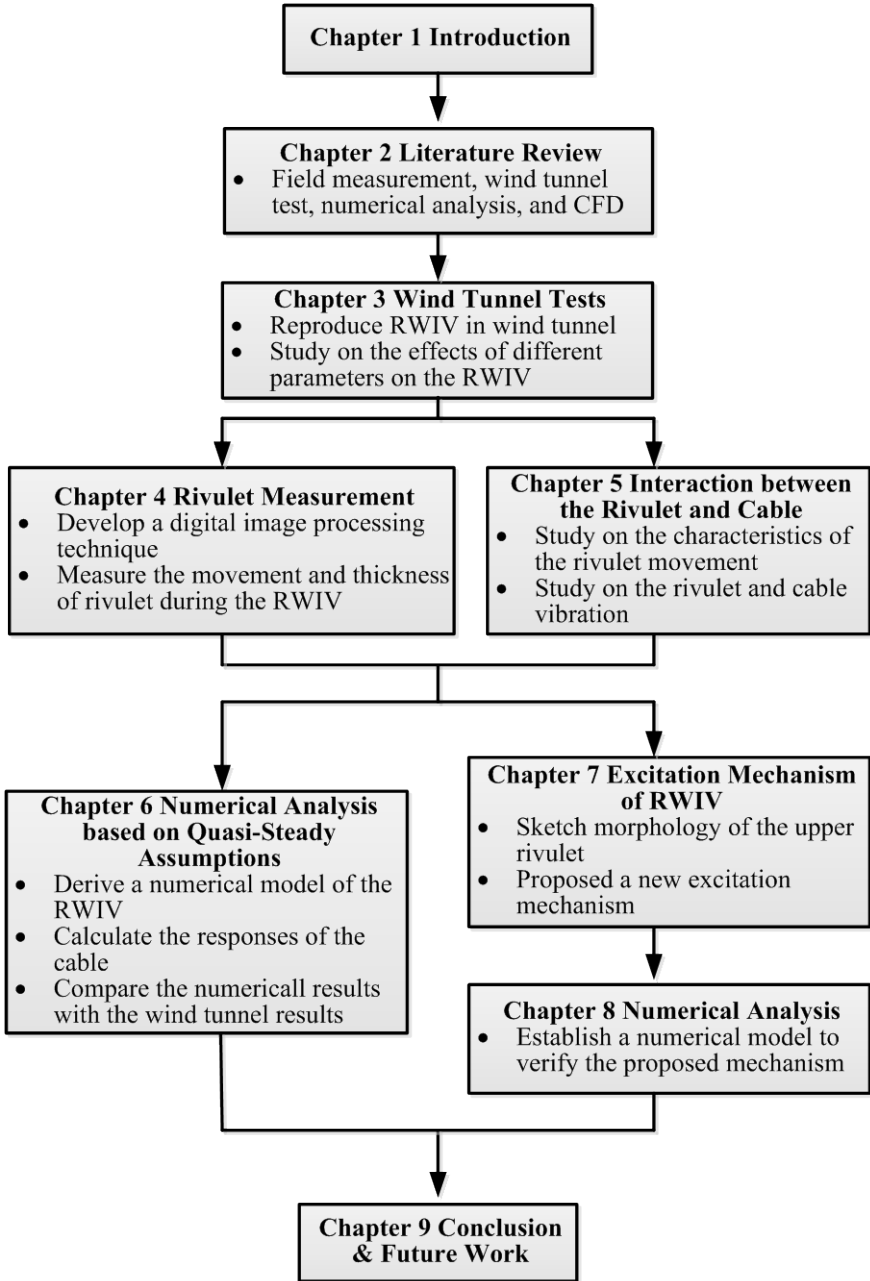
Figure 1-2. Organization of thesis

LITERATURE REVIEW

2.1 Cable Vibration

The stay cables are prone to large vibrations due to their low damping, light mass and great flexibility (FHWA 2007; Xu 2013). The main cable vibrations that require careful consideration by bridge engineers include the parametric vibration (Fujino et al. 1993; Xia and Fujino 2006), vortex−induced vibration (Zdravkovich 1997; Williamson and Govardhan 2008), wake galloping of group cables (Tokoro et al. 2000; Li et al. 2013), galloping of cables with ice accumulations (McComber and Paradis 1998; Chabart and Lilien 1998; Hu et al. 2012), and the RWIV (Hikami and Shiraishi 1988, Xu and Wang 2001, 2003, Gu and Du 2005).

2.1.1 Parametric Vibration

Parametric vibration of the cable is caused by the movement of the anchorages on either the girder or the tower which may be induced by the wind loading, traffic loading. It differs from the regular forced cable vibration. The disturbance of the anchorage movement periodically changes the parameters of the cable. When the external excitation frequency equals twice of the natural frequency of the cable, parametric resonance takes place and a large cable vibration occurs. The parametric vibration of the cable is an instable phenomenon (Fujino et al. 1993; Xia and Fujino 2006).

2.1.2 Vortex-Induced Cable Vibration

Vortex−induced cable vibration is excited by the periodic vortex shedding from the cable's both sides (Zdravkovich 1997; Williamson and Govardhan 2008). It has the characteristics of amplitude- and velocity-restriction at relatively low wind speeds. Vortex−induced cable vibration usually occurs when the wind is approximately perpendicular to the cable axis.

The vortex shedding frequency (f_s) is proportional to the wind speed (U) and inversely proportional to the cable diameter (D). That is

$$f_s = S_t \frac{U}{D} \qquad (2\text{-}1)$$

where S_t is the Strouhal number, which is close to 0.2 in the pre-critical range.

Vortex−induced cable vibration occurs when the vortex shedding frequency matches the natural frequency of the cable. Therefore, the wind speed at which vortex−induced vibration occurs is calculated as:

$$U = \frac{fD}{S_t} \qquad (2\text{-}2)$$

where f is the natural frequency of the cable.

2.1.3 Wake Galloping for Groups of Cables

The wake galloping of the cable is excited by the wake flow of other elements, such

as the tower or other cables (Tokoro et al. 2000; Li et al. 2013). It usually exhibits an elliptical trajectory and takes place at relatively high wind speeds with large amplitude. The Scruton number ($S_c = \dfrac{4\pi m \xi_s}{\rho D^2}$, where, m is the mass of the cable per unit length; ξ_s is the damping ratio of the cable; $\rho = 1.29$ kg/m^3 is the air density) has significant effect on the wind speed of the wake galloping. The critical wind speed U_{crit}, above which the wake galloping of the cable might occur, is estimated as (Irwin 1997; Cooper 1985):

$$U_{crit} = c_1 f D \sqrt{S_c / 4\pi} \qquad (2\text{-}3)$$

where c_1 is constant parameter. For the stay cables, the value of the constant c_1 is recommended as: 25 for $2D \leq l_c < 6D$; 40 for $6D \leq l_c < 10D$; and 80 for $10D \leq l_c$, where l_c is the clear spacing between the cables.

2.1.4 Galloping of Cables with Ice Accumulations

The accumulation of ice changes the symmetrical aerodynamic configuration of the cable, which makes the cable aerodynamically unstable (McComber and Paradis 1998; Chabart and Lilien 1998; Hu et al. 2012). This kind of vibration usually occurs in the long power conductor cables and does not always occur in the stay cables of the bridges. It has the characteristics of large amplitude, low frequency and high wind speeds. The stability of the cable with ice accumulation can be estimated by the well-known Den Hartog galloping criterion :

$$\delta_D = C_d + \frac{\partial C_l}{\partial \varphi} \qquad (2\text{-}4)$$

where δ_D is the coefficient of Den Hartog; C_d and C_l are the drag and lift force coefficients, respectively, and φ is the attacking angle. The cable is table when $\delta_D \geq 0$ but has the potential of galloping when $\delta_D < 0$.

2.1.5 Rain－Wind-Induced Vibration

Large cable vibrations have been observed under the simultaneous occurrence of rain and wind, which is referred as the RWIV. This phenomenon was first identified by Hikami and Shiraishi (1988) and has been observed on many cable-stayed bridges. The RWIV has characteristics of amplitude- and velocity-restriction, large amplitude and low frequency. The water rivulets formed and running on the upper and lower sides of the cable surface are the essential component of this aero-elastic instability. However, the excitation mechanism of the RWIV is still unclear.

Over the past three decades, the RWIV has been investigated by numerous researchers and engineers around the world through field measurements, wind tunnel tests, numerical analysis, and computational fluid dynamics simulation. The four aspects will be reviewed in following sections.

The cable and wind geometry including the inclined angle α and yawed angle β is defined in Figure 2-1. $\beta > 0°$ denotes the wind is in declining direction of the cable, and $\beta = 0°$ denotes the wind normal to the cable plane. The effective yaw angle between the wind direction and the cable axis was $\beta^* = \sin^{-1}(\sin\beta\cos\alpha)$.
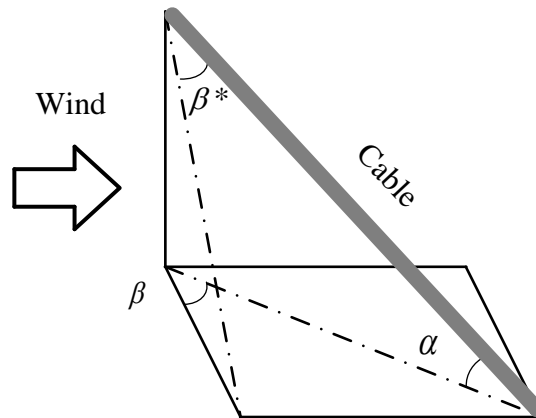
Figure 2-1. Definition of inclined and yawed angle

2.2 Field Measurement

Hikami and Shiraishi (1988) firstly reported the field measurements of the RWIV on Meikonishi Bridge during the construction period. In their study, 24 stay cables had been measured for five mouths. The investigated cable length varied from 65 m to 200 m. The external diameter (*D*) of the cables was 140 mm. The mass of the cable was 37 kg/m and 51 kg/m before and after grouting, respectively. The in-plane acceleration of the cable, wind speed and direction, and rainfall intensity were measured. The large cable vibration only occurred in rainy and wind weather. Therefore, the reason of the large vibration was the combined excitation of the rain and wind. The RWIV occurred when the cables with geometrically decline in the wind direction. Large cable vibration with maximal pick-to-pick (p-p) amplitude of 55 cm occurred under the wind speed of 14 m/s on rainy days. The frequency of the RWIV was observed much lower than that of the classical Karman vortex induced vibration, falling in the range of 1 Hz to 3 Hz. The running rivulets and their circumferential oscillations were also observed.

Yoshimura (1992) summarized the field observations of the RWIV during the construction of the Aratsu Bridge. They observed that most RWIV occurred on the cable declined to the wind direction under light rainfall. The maximal p-p amplitude was measured as 60 cm, approximately 3.5 times the cable diameter.

Geurts et al. (1998) observed the significant vibration of the cable and deck of the Erasmus Bridge under windy and rainy weather conditions. The maximal cable vibration amplitude could be 0.7 m, approximately three times the diameter of the cable. When the large vibration occurred, the yawed angle was about 25° and the wind speed was around 14 m/s. The dominant frequency of cable vibration was 0.8 Hz to 1.2 Hz corresponding to the 2nd and 3rd mode. The large vibrations disappeared as soon as the rain stopped.

Main and Jones (1999) and Main et al. (2001) carried out long-term measurements on the Fred Hartman Bridge in Houston, Texas and the Veteran's Memorial Bridge in Port Arthur, Texas. The root-mean-square (RMS) of the cable displacement in the RWIV could reach as large as 51 cm, corresponding to the p-p amplitude of 1.4 m. The large responses occurred almost purely in single mode and were in-plane cable vibrations. However, most cable vibrations exhibited two-dimensionality and multi-modes cable vibration. The dominant mode of cable vibration ranged from the 1st to 4th mode, with most in the 2nd and 3rd mode. All vibration frequencies were between 1 Hz to 3 Hz, with the largest density at around 2 Hz. For a given stay cable, the RWIV likely occurred in a certain mode over a fairly wide range of wind speeds. The observed cable vibrations on the Hartman Bridge were categorized into three

distinct regimes: non-rain vibrations, moderate-rain vibrations, and heavy-rain vibration, each exhibiting different characteristics. In the absence of rainfall, relatively small vibration was observed of higher modes, which coincided with the classical Karman vortex induced vibration. Most of the large cable vibrations were associated with the moderate rain, and had similar characteristics as those reported in previous studies. Under the heavy rain, large-amplitude cable vibration was observed at the relatively low wind speed with the participation of numerous modes. Main and Jones (2000) further analyzed the modal participation in the measured cable vibration events and investigated the influence of rainfall on the RWIV. It was found that large vibration occurred in the lower mode over a wide range of wind speeds with rainfall, while small response occurred in higher mode within a narrow wind speed range without rainfall.

Matsumoto et al. (2003a) built a full-scale test bed outdoor to measure the cable response under natural weather conditions. The system consisted of a steel tower with the height of 23.5 m and a cable model with the length of 30 m. The cable model was coved by polyethylene same material as the surface of real stay cables. The external diameter of the cable model was 0.11 m. The upper end of the model was fixed on the tower at the level of 21 m, and the lower end was tied on the ground. Accelerometers and displacement meters were installed at 2.8 and 2.0 meters apart from the lower end of the cable, respectively. They observed that cable vibration occurred both with and without rainfall, whereas exhibited quite different characteristics. Under the similar wind condition, the cable vibrated in the 7th and 8th modes without rainfall, whereas in the 3rd and 4th modes with rain. In addition, the vibration amplitude was larger when there was precipitation.

Scott Phelan et al. (2006) monitored the responses of the stay cables of Veterans' Memorial Bridge. They concluded that the RWIV occurred under the combined conditions of wind and rain, in which the wind speed ranged between 6 to 14 m/s and the relative yaw angle was between 10° to 50°. The largest cable vibration occurred when the relative yaw angle were between 30° to 35°. Velocity-restricted cable vibrations were also observed when the wind normal to the cable plane, without rain, and the wind speed ranged between 7 to 11 m/s. However, this type response appeared in higher modes at much smaller amplitude, corresponding to the Karman vortex induced vibration.

Ni et al. (2007) conducted continuous field measurement on the cable-stayed Dongting Lake Bridge. They observed that large amplitude RWIV occurred under the mean wind speed of 6-14 m/s (at deck level), mean wind direction (relative yaw angle) between 10° and 50°, and light to moderate rain (less than 8 mm/h). The largest acceleration amplitude reached 10g. The two-dimensionality and the participation of numerous modes of the cable vibration were also observed. The in-plane acceleration response amplitude was approximately two times of out-of-plane. The overall dominant mode was the 3rd mode in all the RWIV events. However the dominant mode could vary during the process of vibration evolution.

Zuo et al. (2008) and Zuo and Jones (2010) conducted two long-term field measurements on the Fred Hartman Bridge and Veteran's Memorial Bridge. They reported that the RWIV differed from the classical Karman vortex-induced vibration, although both were self-limited. In particular, the RWIV occurred in the lower

frequency at much higher wind speeds with larger amplitude than the vortex-induced vibration. They addressed the importance of the three-dimensional nature of the RWIV, and indicated that the RWIV might be caused by a new type of vortex-shedding, rather than the classical Karman vortex shedding. They also noted that the mode of the stay cable vibration was related to the wind speed and direction. The vibration in higher modes usually occurs under higher wind speed for the same attack angle. For the same mode of vibration, the required wind speed increases as the attack angle deviates from 90°. Besides, they also observed that large cable vibrations when there was no rainfall and these vibrations had similar characteristics as the RWIV. At last they pointed out that the rainfall might be not the on-set condition of the RWIV but promote or enhance this vibration.

Conditions and parameters of the above field measurements are summarized in Table 2-1.

Table 2-1. Summary of the RWIV observed on-site

Author	Bridge	Cable parameters	Weather	Maximal p-p amplitude	Mode / Frequency
Hikami and Shiraishi (1988)	Meikonishi Bridge	D = 140 mm L = 65 ~ 200 m	U = 5 ~ 17 m/s β >0° With rainfall	55 cm	Single mode: 1st to 4th mode / 1.0 ~3.0 Hz
Yoshimura (1992)	Aratsu Bridge	--	U = 10 ~ 18 m/s With rainfall	60 cm	Single mode: 1st or 2nd modes
Matsumoto et al. (1995)	--	D = 140 ~ 200 mm	U = 6 ~ 17 m/s With rainfall	240 cm	Single mode: 1st or 2nd mode / 0.56 ~1.12 Hz
Geurts et al. (1998)	Erasmus Bridge	D = 160 ~ 225 mm L = 85 ~ 300 m	U = 5 ~ 17 m/s β = 25° With rainfall	140 cm	Single mode: 2nd or higher modes / 0.8 ~1.2 Hz
Scott Phelan et al. (2006)	Veterans' Memorial Bridge	D = 114 mm L = 51, 57, 97 m	U = 6 ~ 14 m/s α = 21.6°, β^* = 10° ~ 52° With rainfall	--	Single mode: 2st Multi-modes: 2nd to higher modes
Ni et al. (2007)	Dongting Lake Bridge	D = 119 mm L = 122 m	U = 6 ~14 m/s α = 35.2°, β^* = 10° ~ 50° With rainfall	--	Dominating mode: 3rd mode / 3.2 Hz
Main and Jones (1999) Main et al. (2001) Zuo et al. (2008)	Veteran's Memorial Bridge Fred Hartman Bridge	D = 107 ~ 194 mm L = 87 ~ 198 m	U = 5 ~ 13 m/s α = 21° ~ 49° β >0 or β <0 With or without rainfall	140 cm	Multi-modes: 2nd to 6th mode

The field measurement data were directly obtained under the practical conditions without artificial interference and thus are convincing and valuable. From the field observed results, the on-set conditions and response characteristics of the RWIV

were summarized as follows.

2.2.1 Occurrence Conditions of the RWIV

(a) Wind speed and direction

As Table 2-1 shows, all RWIV observed through field measurement were velocity-restricted, similar to the conventional Karman vortex induced vibration. The wind speed of the RWIV were 5 to 18 m/s, corresponding to the reduced wind speed ($U_r = U / fD$) of 20 to 120, much higher than that required for the classical Karman vortex induced vibration ($U_r \approx 5$).

Comparing with the wind speed, the wind direction of the RWIV was more complicated. Most RWIVs occurred on the cable geometrically declining in the wind direction, such as the Meikonishi Bridge, Erasmus Bridge, and Dongting Lake Bridge. However, Main and Jones (1999), Zuo et al. (2008), and Zuo and Jones (2010) observed the large cable vibration when the cable was non-declined in the wind direction on the Fred Hartman Bridge and Veteran's Memorial Bridge. In Dongting Lake Bridge, the RWIV occurred at the relative yaw angle of 10° to 50°. Zuo et al. (2008) and Zuo and Jones (2010) reported that at the same wind direction, the cable vibrations in the higher modes usually occurred at the higher wind speed. For the same mode of vibration, the required wind speed for the large vibration increased as the attack angle deviated from 90°.

(b) Influence of rainfall

Most field observations showed that the RWIV occurred under the combination

effect of rain and wind. The majority of large amplitude RWIVs were observed during light to moderate rainfall. Hikami and Shiraishi (1988), Scott Phelan et al. (2006), and Ni et al. (2007) reported that when the rain stopped, the cable ceased to vibrate suddenly even the wind conditions remains unchanged. Main and Jones (1999) observed that only the Karman vortex induced vibrations occurred without rainfall.

However, large cable vibrations were also observed under no rainfall condition by some researchers. Matsumoto et al. (1990, 1998) reported that an inclined polyethylene cable of 187 m long experienced a violent vibration without rain. The maximal cable vibration amplitude was approximately 1.5 m. This vibration severely damaged the cable surface and the edge faring of the girder. Large cable vibrations had been also observed when there was no rain in Fred Hartman Bridge (Zuo and Jones 2010). The observed large vibrations occurred over the same ranges of wind speed and direction as the RWIV, and the amplitude was over the diameter of the stayed cable.

Scott Phelan et al. (2006) and Ni et al. (2007) reported that most large amplitude RWIVs occurred under the light to moderate rain (less than 8 mm/h). Under heavy rain condition, as observed by Main et al. (2001), RWIVs occurred at a smaller wind speed than that of moderate rain. In the case of drizzle (below 1 mm/h), the RWIV could be excited when the wind speed and direction in proper range.

2.2.2 Response Characteristics of the RWIV

(a) Large amplitude and low frequency

Field measured RWIVs exhibited the characteristics of large amplitude and low

frequency. As Table 2-1 shows, the smallest maximal p-p displacement amplitude of the RWIV was larger than 3.9 times the diameter of cable and most of the RWIVs occurred in the first three modes. Some are even 10 times the cable diameter (Matsumoto et al. 1995; Main and Jones 1999; Main et al. 2001).

(b) Amplitude-restricted

Although the amplitude of the RWIV was large, almost all of them showed the characteristic of amplitude-restricted. Although the largest p-p displacement amplitude of the full scale measurements reached 2.4 m, no divergent RWIV was reported in the field observation.

(c) Vibration modes

The RWIV occurred in a single mode as well as in multi-modes. The RWIV were first observed in a single mode such as Hikami and Shiraishi (1988) and Yoshimura (1992). The multi-mode RWIV were later observed by Matsumoto et al. (1998), Ni et al. (2007), Zuo et al. (2008), and Zuo and Jones (2010). The multi-mode RWIV was similar to the multi-mode vortex induced vibration. In Dongting Lake Bridge, most cables experienced multi-mode RWIV, and only a few cases of the response were similar to the single mode vibration (Ni et al. 2007).

Mode-transition, which means the RWIV mode gradually changes from the initial one to the other or to multi-modes, was also observed in the field testing. Ni et al. (2007) reported that the dominant mode of the RWIV changed from the 2nd mode at the beginning to the 3rd at last.

(d) In-plane and out-of-plane vibrations

At the early stage of the field measurement, only in-plane RWIV were reported such as by Hikami and Shiraishi (1988). Later on more and more two-dimensional RWIV were reported such as by Main and Jones (1999) and Ni et al. (2007). Ni et al. (2007) presented an example of the RWIV in both in-plane and out-of-plane. The in-plane acceleration response amplitude was approximately two times the out-of-plane amplitude.

Although valuable data have been obtained through field measurement, it also has limitations such as:

1) The field environment such as the weather condition is very complex and out of control.

2) The real structural systems are very complicated and would be influenced by many factors. The real factors affecting the RWIV may be masked by other factors and thus it is difficult to precisely investigate the RWIV.

3) Many parameters such as the cable diameter, fundamental frequency, damping ratio, and cable surface are unchangeable in real stay cable. The effects of such parameters on the RWIV are unpredictable through field measurement.

4) Installation of transducers on real bridges may not be allowed.

2.3 Wind Tunnel Test

Due to the constraints of field testing described above, plenty of wind tunnel tests have been conducted to better understand the RWIV, in which wind parameters (such as wind speed and direction and rainfall) could be controlled and their effects on the

RWIV can be thus separately investigated. During the studies, the cable model was tested both with and without the simulation of the rivulets. Two different methods were adopted to simulate the water rivulets: (1) spraying water appropriately on the cable surface; and (2) sticking artificial rivulets on the cable surface.

2.3.1 Spraying Water on the Cable Surface

Spraying water simulates actual water drops falling and flowing on the cable model surface under the action of wind, gravity, and cable vibration, rivulets are formed on the cable surface. The simulated rivulets have the natural profile as on-site and can freely oscillate on the cable surface.

Hikami and Shiraishi (1988) first reproduced the RWIV in an open-jet wind tunnel by spraying water on the cable surface. They examined the effects of different parameters on the RWIV, such as the wind speed and direction, water rivulets, vibration amplitude, and vibration frequency. It was found that the RWIV occurred only when the cable declined in the wind direction and this type of cable vibration was velocity-restricted and amplitude-restricted as observed on-site. Two water rivulets were observed on the upper and lower sides of the cable. They circumferentially oscillated on the cable surface during the RWIV. It was also pointed out that the fundamental frequency of the cable had almost no effects on the wind speed range but significantly affected the amplitude of the RWIV. They concluded that the essential reason of the RWIV was the upper water rivulet, which periodically changed the cross section of the cable and caused it aerodynamically unstable.

Matsumoto et al. (1995) also conducted a series wind tunnel tests on an inclined/ yawed cable model with the rivulets simulated by spraying water and measured the location of the rivulets when the cable model was static.

Saito et al. (1994) reproduced the RWIV in a large-scale wind tunnel using a full-scale cable model under the simulated wind and rain and tried to suppress this large vibration with the longitudinal projections. They found that the natural frequency of the cable model had no effects on the wind speed region of the RWIV and the turbulence would stabilize the cable vibration.

Flamand (1995) conducted wind tunnel tests in a climatic wind tunnel using a full-scale cable model. He reported that the RWIV occurred at the wind speed ranging from 7 to 13 m/s and at the yaw angle ranging from 25° to 50°. The importance of the upper water rivulet and its movement around the cable surface were confirmed. It was also found that the cable surface condition played an important role in the RWIV. In particular, the dirt coating of the cable would enhance the upper rivulet oscillation and consequently destabilized the cable. He suggested that disorganizing the movement of upper rivulet was able to suppress the RWIV of inclined cable.

Verwiebe and Ruscheweyh (1998) investigated the excitation mechanism of the RWIV through wind tunnel test. They observed that the RWIV occurred at the wind speed of 8 to 30 m/s. Besides, the RWIV could occur both in-plane (cross-wind direction) and out-of-plane (along-wind direction), depending on the cable geometry (α, β) and the wind speed. They proposed three kinds of excitation mechanisms

based on the interaction between the motion of rivulets in the circumferential direction and the oscillation of the cable model, including one type of in-plane vibration and two types of out-of-plane vibration. When the two rivulets symmetrically oscillated on the surface in the natural frequency of the cable, the RWIV took place in the along-wind direction. The other two types cross-wind RWIV were excited by anti-symmetric oscillation of the rivulets and the oscillation of the lower rivulet on the surface in the natural frequency of the cable, respectively.

Gu and Du (2005) reproduced the RWIV in wind tunnel by spraying water and investigated the effects of parameters such as the wind speed and direction and rainfall on the RWIV and its mitigation. It was observed that the largest RWIV occurred when the cable inclination angle was around 30° and wind yaw angle ranged from 30° to 35°. The amplitude of the RWIV obviously decreased with the increase of the damping ratio and fundamental frequency of the cable. They concluded that the upper rivulet and its motion should be the prerequisite of the appearance of the RWIV. Besides, the spiral wire with appropriate diameter and pitch and twine direction on the cable surface was effective in mitigating the RWIV.

Cosentino et al. (2003a) measured the unsteady wind pressure, rivulet thickness, and upper rivulet oscillation on a cable model under rain and wind in a wind tunnel. They observed that the upper rivulet circumferentially oscillated on the cable surface in the frequency of cable vibration. They pointed out that the RWIV was determined by a flow regime modification which occurred close to the critical range of Reynolds number ($R_e = UD/\upsilon$, υ denotes air kinematic viscosity). Such flow regime fluctuations were related to the air-rivulet interference.

Li et al. (2010a) also measured the thickness, width, and movement of the rivulets around a cable model using an ultrasonic technique in a wind tunnel. They observed that the mean thickness of the upper and lower rivulets was approximately 0.5 mm and 0.6 mm, respectively. The width of the upper and lower rivulet was approximately 8.0 and 3.9 mm, respectively. Besides, the lower rivulet was more or less fixed during the RWIV, whereas the upper rivulet circumferentially oscillated around the equilibrium position with the RMS of 7° at the same frequency as the natural frequency of the cable.

Wang et al. (2005) investigated the effect of two water rivulets on the fluid dynamics in the wake of an inclined cable with the inclination angle of 45° and wind yaw angles of 0° to 90° at the wind speed of 8-15 m/s in a wind tunnel. The intermittent quasi-periodic vortex street was observed with and without the water rivulets. They concluded that large circumferential oscillation of the upper rivulet perturbed the flow separation of the inclined cable and, when the perturbation frequency was close to the nature frequency of cable, a large cable vibration might be excited. Mahbub Alam and Zhou (2007) experimentally studied the fluid dynamics around an inclined circular cylinder with and without water running on its surface. They concluded that the main reason of the RWIV was the vortex shedding. The water rivulets running on the cable could enhance the two-dimensionality of the flow, which contributed to the large cable vibration.

Although spraying water has a lot of advantages, it also has some drawbacks. The simulated rivulets strongly and complexly depend on many uncontrollable

parameters. The researchers can neither easily modify the shape of the water rivulet nor change their position as well as the movement state. The simulated rivulets are not very stable and are sensitive to the parameters such as the wind speed and the state of cable vibration. For the scaled models, it is difficult to apply the similarity law to both the cable model and water rivulets, because the water droplet cannot be modified.

2.3.2 Sticking Artificial Rivulets on the Cable Surface

Sticking artificial rigid rivulets was also used to simulate the rivulets in wind tunnel tests.

Yamaguchi (1990) conducted wind tunnel tests using a two-dimensional rigid model attached with an artificial water rivulet to investigate the RWIV based on quasi-steady assumptions. In his test, a figure-8 shaped model was used to simulate the cable attached by the artificial upper water rivulet. The influence of the geometric size of the artificial rivulet on the steady wind force coefficients was studied, in which the ratio of the rivulet diameter to the cable diameter was 0.1, 0.2, and 0.4, respectively. They concluded that the scale of artificial water rivulet had small influence on the steady wind force.

Matsumoto et al. (1992, 1995, 1998) conducted a series of wind tunnel tests to study the excitation mechanism of the RWIV. The on-set conditions of the RWIV were summarized from the experiments on a prototype cable. They indicated that the artificial upper rivulet on the cable surface, the axial flow in the near wake of the cable, and the span-wise three-dimensional Karman vortex shedding could trigger a

large vibration simultaneously or separately. The responses of the inclined cable were classified into the velocity-restricted type and the divergent type. The former type of cable vibrations occurred at the low wind speed, which was induced by the span-wise three-dimensional Karman vortex shedding or the formation of the upper rivulet, while the later occurred at the high wind speed, which was attributed to the negative slope of the lift force coefficient because of the formation of the upper rivulet at the certain location or the generated axial flow. Besides, the cable response was very sensitive to the cable–wind geometry (α and β) and the location of the upper rivulet. The effects of the turbulence on the response of the cable were complicated. The turbulence could stabilize or destabilize the cable vibration. Later, Matsumoto et al. (2005) installed a perforated splitter plate in the wake of a non-yawed circular cylinder attached by an artificial upper rivulet to simulate the influence of the axial flow. The steady aerodynamic forces on the circular cylinder were measured. They concluded that both the upper rivulet and the axial flow simulated by the perforated splitter plate could induce the inclined cable to galloping vibration.

Bosdogianni and Olivari (1996) used two bars and oil to simulate the water rivulets and tested a small rigid cylinder in a wind tunnel to investigate the source of the instability of the inclined cable. They concluded that the presence of a rivulet at a certain position, rather than the motion of the rivulet, caused the cable instability.

Xu et al. (2006) measured the drag and lift coefficients of an inclined cable with an artificial upper rivulet against the rivulet position. They investigated the effects of the artificial rivulet's shape and size on the aerodynamic coefficients of the inclined cable. The aerodynamic coefficients of the inclined cable significantly varied with

the position of upper rivulet and the size and shape of the artificial rivulet had no significant effects on the variation pattern of the aerodynamic coefficients. They concluded that the observed negative slope in the lift coefficient curve was the reason of the RWIV.

Gu (2009) and Du et al. (2013) conducted wind tunnel tests to measure the aerodynamic forces and wind pressure acting on the cable and the rivulet. The cable was simulated by a static inclined cylinder attached with an artificial upper rivulet. They investigated the effect of the artificial rivulet on the aerodynamics of the inclined cable. They concluded that the key reason of the RWIV might be the significant variations of the aerodynamic force coefficients of the cable and upper rivulet when the upper rivulet was located at different positions. The upper rivulet can either enhance or suppress the classical vortex shedding.

The artificial rivulets attached on the model surface were made in plastic or wood. This kind of artificial rivulet has the advantage of easy control (in shape, position) and good stability. However, its drawbacks are very obvious. The profile of the artificial rivulet might be different with the real one. The rivulet position and shape could not freely change as the real one. These compromise the interaction between the rivulets, wind, and cable vibration.

2.3.3 No Simulation of Rivulets

Some researchers have tested dry inclined cable models in the wind tunnel. The dynamic responses of the inclined cable model are measured in dynamic tests, while the wind pressure distribution and the aerodynamic coefficients are measured on the

static rigid cable model.

Matsumoto et al. (1990) investigated the fundamental aerodynamic characteristics of an inclined/yawed cable. They observed that large vibration occurred when the cable model was declined and non-declined in the wind direction and concluded that the existence of the rivulet could change the characteristics of the cable responses, which could be divergent or velocity-restricted. The secondary axial flow formed in the near wake of the cable was the main reason of the aerodynamic instability of the yawed or inclined cable. The rainfall was just an amplifier of the instability of the yawed or inclined cable. At last, they proposed a few countermeasures to suppress the cable vibration.

Matsumoto et al. (1992, 1995, 1998) investigated the aerodynamic response and aerodynamic characteristics of the dry cable models. Large cable vibrations could occur even there was no rivulet. They pointed out that the three-dimensional Karman vortex shedding also played an important role. Again they addressed that the secondary axial flow in the near wake of the cable was the main reason of the instability of the yawed/inclined cable. The axial flow in the near wake of the cable could trigger a large vibration even without the upper rivulet. Matsumoto et al. (2001, 2003b) further investigated the responses and the aerodynamic characteristics of an inclined cable without the upper rivulet and observed significant cable vibration in the case. They indicated that the RWIV might be a type of vortex-induced vibration at high reduced wind velocities due to the fluid interaction between the classical Karman vortex and axial vortex.

26

Cheng et al. (2003, 2008a) conducted the wind tunnel tests to investigate the response of the inclined cable without the water rivulets. Both the divergent and velocity-restricted responses of the inclined dry cable were observed at the high reduced velocity. They found that the former was similar to the classical galloping whereas the latter occurred only in a narrow region of the high reduced wind velocity. They deducted that the latter might be induced by the vortex formed along the cable.

Boujard (2007) measured the wind pressure distribution and the aerodynamic force coefficients of an inclined and yawed circular cylinder. They found that the wind pressure distribution and aerodynamic force coefficients significantly varied with the flow state indicated by the Reynolds number (R_e). The lift force coefficient first decreased from around zero to negative values and then returned back to zero along with the decrease of the drag force coefficient when R_e varied from 2.1×10^5 to 3.5×10^5. They proposed that the decrease of the lift force coefficient was caused by the increase of the negative pressure on the lower side of the cylinder, which appeared when transition occurred in the separated shear layer and induced the boundary layer re-attachment on lower side of the cylinder.

Jakobsen et al. (2012) investigated the aerodynamic response and the surface pressure distribution of an inclined dry circular cylinder in the critical range of R_e. They observed that large vibrations occurred within two narrow ranges of R_e. Most cylinder responses could be larger than 10% of the cable diameter, and the largest response occurred around the end of the drag crisis range with the RMS of 42% of the cable diameter. Besides, it was found that in the critical range of R_e, a highly three dimensional flow was generated around the inclined cylinder. They concluded

that the basic reason of the large response of inclined cylinder was the low-frequency component in the wake flow during the formation of the one-bubble regime and disruption of the two-bubble regime.

Matteoni and Georgakis (2012) investigated the effects of the surface roughness and cross-sectional distortions on the aerodynamic force coefficients of the inclined/yawed dry cable models. They observed that even small geometrical defect of the cable model, such as distortion of the shape or alterations of surface could change the aerodynamic coefficients.

Nikitas et al. (2012) and Nikitas and Macdonald (2015) experimentally studied both static and dynamic dry inclined cable in a wind tunnel and found that the occurrence of large vibrations coincided with the critical regime of R_e. They also investigated the difference of the wind pressured distribution and aerodynamic response between the yawed and non-yawed cables. It was observed that the cable at certain angle could stately maintain different flow states along its length, whereas at other angle the flow intermittently jumped between different states, resulting in the alteration of the lift force coefficient in value or sign. They suggested that the sudden jump in the lift force and the vortex dislocation along the cable model in the longitudinal direction were related to the aerodynamic instability of the dry inclined cable. Besides, the galloping of the dry inclined cable was not only caused by the bursting of a laminar separation bubble but also related to the organization of the noise arising from the transition and the wind turbulence.

2.3.4 Response Characteristics and On-set Conditions

From the data obtained through wind tunnel tests, the characteristics of the RWIV are summarized in terms of the response characteristics and on-set conditions as follows.

(a) Influence of wind speed and wind direction

The RWIV was widely reported has the characteristics of amplitude-restricted and velocity-restricted as first observed by Hikami and Shiraishi (1988) in field testing. They tested an inclined cable model ($\alpha = 45°$ and $\beta = 45°$) with the diameter of 140 mm in wind tunnel and found that the wind speed of the occurrence of the RWIV ranged from 9 m/s to 13 m/s. Gu and Du (2005) observed that the RWIV of a cable with diameter of 120 mm only occurred in the wind speed range of 7 m/s to 10 m/s. Flamand (1995) also found that the RWIV of a cable model with the diameter of 160 mm took place when the wind speed ranged from 7 to 12 m/s. However, the galloping response was also observed by Matsumoto et al. (1992, 1995) and Cheng et al. (2003, 2008).

Some researchers, for example Hikami and Shiraishi (1988), concluded that the RWIV only occurred when the cable inclined in the wind direction. Similar conclusion was observed by Gu and Du (2005) and Flamand (1995). The former measured that the RWIV of a cable model occurred at an inclined angle of 30° and the yaw angle ranged from 30° to 40°, and the latter pointed out that the yaw angle of the occurrence of the RWIV was from 25° to 50° for a cable model with the inclined angle of 25°. However, some others, for example Matsumoto et al. (1990), also observed that large vibration occurred when the cable was non-declined in the wind direction.

(b) Influence of frequency

The effects of the natural frequency of the cable on the RWIV have been widely investigated such as by Hikami and Shiraishi (1988), Saito et al. (1994), and Gu and Du (2005). All the test results show that the amplitude of the RWIV became smaller when the model frequency became higher. However, the wind speed range of the RWIV was unchanged, which was independent of the model frequencies.

(c) Influence of water rivulets

As mentioned before, the importance of water rivulets to the occurrence of the RWIV was reported in many wind tunnel tests. Hikami and Shiraishi (1988) thought that the circumferential oscillation of the upper rivulet, causing a periodic change of the cable cross-section, was the key factor of the RWIV. Bosdogianni and Olivari (1996) hold the idea that not the movement but the position of the upper rivulet induced the vibration. However, Verwiebe and Ruscheweyh (1998) stated that not only the upper rivulet but also the lower rivulet were essential for the RWIV. Gu and Du (2005) later observed that the location and movement state of the upper rivulet played the most important role in the RWIV.

The rivulets were also believed to be associated with the characteristics of speed restriction and limited amplitude of the RWIV. The location and movement state of the water rivulets were determined by gravity force, inertia force, wind pressure and the water repellency. The inertia force depends on the movement of the cable and rivulets, and wind pressure force depends on the wind speed. Those relationship makes the rivulets can only be formed just in restricted wind speed and limited

vibration state of the cable, which coincides with the characteristics of amplitude- and velocity-restriction of the RWIV.

2.3.5 Aerodynamic Force and Wind Pressure Distribution

Yamaguchi (1990) firstly investigated the influence of the upper rivulet location (or attacking angle) on the aerodynamic forces of a two-dimensional cable model. He measured the aerodynamic coefficients curve versus the upper rivulet location.

Xu et al. (2006) measured the aerodynamic coefficients curve on both two-dimensional and three-dimensional cable model using a force balance. They found that the effect of water rivulets on aerodynamic forces was obvious. When the rivulet position ranged between 40° and 50°, the drag and lift coefficients suddenly increased and decreased, respectively.

Gu (2009) and Du et al. (2013) measured the wind pressure distribution of a cable model attached with an artificial rivulet using an electronic pressure scan valve system. The aerodynamic forces were obtained by integrating the wind pressures around the cable model. When the artificial rivulet was located 0° to 20° from the stagnation point, the wind pressure distribution of the two-dimensional cable model with rivulet was very similar as those of the two-dimensional smooth cable ($\alpha = 0°$ and $\beta = 0°$). When the upper rivulet was located 20° to 40° from the stagnation point, compared with the pressure distribution of cable without artificial rivulets, the absolute value of the mean wind pressure at the tap position just behind the upper rivulet suddenly became much larger than those in front of the upper rivulet; while the others almost remained unchanged. The three-dimensional ($\alpha > 0°$ and $\beta > 0°$)

model had similar results. They also tested the wind pressure and the aerodynamic forces on the artificial rivulet.

2.4 Numerical Analysis

Some researchers investigated the RWIV through numerical analysis on the basic of the quasi-steady assumptions. The aerodynamic forces measured from the wind tunnel tests were applied to the numerical model of the cable and the cable responses were then calculated.

Yamaguchi (1990) established two mathematical models: the single degree of freedom (SODF) model (Den Hartog mechanism) and the two degree of freedom (TDOF) model, by means of quasi-steady galloping analysis. They concluded that the latter could explain large RWIV and the circumferential oscillation of upper rivulets was critical to the increase of the cable vibration.

Geurts et al. (1998) modified the SODF galloping model by including the movement of water rivulets and calculated the cable responses. They concluded that the movement of the rivulets was merely the "trigger" of the RWIV in cables, and was of minor importance to their instability.

Xu and Wang (2001, 2003) proposed an SDOF model and a two degrees of freedom (TDOF) model to numerically analyze the response of an inclined and yawed cable with consideration of the effect of the upper rivulet. They considered the effect of the mean wind velocity on the initial position of the upper rivulet and the effect of the oscillating rivulet on the cable. For the SDOF, the upper rivulet oscillation was

assumed to be proportional to the cable vibration. The analytical models were verified by comparing the numerical results with the wind tunnel testing results. They concluded that the velocity- and amplitude-restricted RWIV was mainly induced by the negative aerodynamic damping or the excitation force arising from the interaction between the wind, water rivulets, and cable vibration.

Wilde and Witkowski (2003) derived a similar SODF model with the assumption that the upper rivulet circumferentially oscillated with the same frequency as the cable and the amplitude ratio between the upper rivulet and the cable vibrations was constant for a given wind speed. They estimated the maximum amplitude of the RWIV with their proposed mathematic model.

Cosentino et al. (2003b) proposed a three degrees of freedom model consisting of a two dimensional motion of the cable and an oscillating upper rivulet. The upper rivulet was subjected to external pressure gradients, air−water friction, cable−water friction, gravity effects, and an inertia effect. The numerical results agreed with those obtained in a wind tunnel test. However, although they considered the aero elastic force of the cable due to the presence of water rivulets, they did not include the longitudinal correlation.

Cao et al. (2003) constructed a stochastic model for the RWIV. The aerodynamic forces on the cable were assumed to be modified by the position of the upper rivulet. The movement of the upper rivulet was described using a simple stochastic process. The response of single cable was explored using the drag and lift force coefficients obtained through wind tunnel test. They suggested that the large vibration of cable

was due to the stochastic excitations by the moving rivulets.

Peil and Dreyer (2007) used a mathematical approach to simulate the RWIV and the rivulet. In their method, the cable response was calculated in displacement, velocity, and acceleration. The inertia force caused by the cable vibration was applied on the water rivulet. The rivulet's shape, position, and velocity were then calculated. In turn, the aerodynamic forces on the cable could be obtained according to the position of the water rivulet. They investigated the interaction between the wind flow, the movements of the cable and the rivulets, leading to self-induced vibration.

Seidel and Dinkler (2006) considered the rivulet as a movable disturbance that oscillated around the transition point of the flow at the same frequency as that of the cable vibration. The periodic disturbance induced the periodic transition of the flow from pre-critical to critical flows, resulting in the transfer of energy from the flow to the elastic structure.

Gu (2009) established a TDOF model and calculated the inclined and yawed cable response. In the model, the exciting forces on the cable consisted of the elastic force, structural damping force, inertial force, aerodynamic forces, gravity force, and the friction force between the cable surface and rivulet. The forces acting on the rivulet included the inertial forces caused by the cable's motion and the rivulet motion itself, rivulet's gravity, aerodynamic forces, and the friction force between the water rivulet and the cable surface. Both the aerodynamic forces of cable and rivulet were obtained through wind tunnel test. The model was able to estimate the responses and the onset wind speed of the cable. The numerical analysis results reflected the

response characteristics of amplitude- and velocity-restriction to some extent. However, the vibration amplitude calculated from the numerical analysis differed from that of the wind tunnel test. He also expanded the TDOF model to a continuous cable considering the influence of the wind profile.

2.5 Computational Fluid Dynamics

CFD is an efficient method to investigate the RWIV because it can provide lots of detailed information which could not be obtained by other methods. The RWIV is a complex interaction process of rain, wind and cable. Up to now, there has not software which could simulate this kind of phenomenon perfectly. CFD was used to investigate the RWIV in three aspects: (1) simulate the formation and growth of water rivulets; (2) evaluate the aerodynamic forces acting on the cable with given rigid rivulet, similar to the wind tunnel test using artificial rivulets to measure the aerodynamic forces, which has been developed just for a few years; and (3) simulate the wind flow passing the dry yawed cable.

2.5.1 Formation and Growth of Rivulets

The investigation of the formation of the rivulets with numerical approach just started a few years ago. Lemaitre et al. (2007, 2010) firstly derived a model to simulate the evolution of a water film on a cylinder blown by the wind. The model was successfully used to predict the formation and position of the rivulets when the wind was normal to the cable axis ($\beta = 90^{o}$). They expanded the model to all possible three-dimensional configurations and investigated the minimum wind speed for the appearance of the two wind-induced rivulets as well as the maximum wind

speed for the existence of the rivulets. However, their simulation was based on the fixed aerodynamic loading measured on a smooth and dry cylinder through wind tunnel tests. This indicates that the aerodynamic forces were constant when the rivulets developed from the liquid film, during which the configuration of the cable model changed according to the shape of the rivulets and the aerodynamic forces should be consequently influenced. The effect of the cable configuration variation on the aerodynamic force distribution was ignored.

Robertson et al. (2010) and Taylor and Robertson (2011, 2015) firstly used a coupled model to simulate the formation process of the rivulets. The model coupled the discrete vortex method solver and a pseudo-spectral solver. The former was used to determine the external flow field and unsteady aerodynamic loading acting on the water film and the latter was used to calculate the evolution and growth of the water rivulets under the external loading. With the new coupled model, the effects of different loading combinations (shear, pressure, surface tension and gravity) were investigated. They observed that the upper rivulet periodically formed on the cable surface and it frequency was related to the initial thickness of the water film. They concluded that the rivulet formation and oscillation played an important role in the RWIV.

For the first time, Bi et al. (2013, 2014) derived a two dimensional coupled equation of water film evolution by combining the lubrication theory and single-mode system vibration theory. The evolution of the water rivulets, aerodynamic forces of the cable, and cable vibration were calculated by solving the coupled equation. Their numerical results showed that the RWIV occurred within a special wind speed range and the

water film periodically varied close to the cable frequency. They concluded that the resonance between the cable and rivulets was the main reason of the RWIV.

Cheng et al. (2015) combined direct numerical simulations and large eddy simulations to simulate the evolution of the rain drops on a cable subjected to the wind. They categorized the morphology of rain drops evolution into four patterns: collision–splashing; accumulation–slipping; formation–breaking; and dynamic equilibrium. Besides, the upper rivulet was observed circumferentially vibrating on the cable surface with the dominant frequency of 0.98 Hz.

2.5.2 Aerodynamic Forces Simulated by CFD

Li et al. (2010b) firstly used CFD to evaluate the aerodynamic forces of a cable model with given rivulet. It was a hybrid approach and proved to be effective. Both the position of rivulets and the movement of cable and rivulets were based on the wind tunnel test. Given the boundary conditions of the cable and rivulets, the aerodynamic forces of the cable were calculated. The aerodynamic forces were then applied to an SDOF model to calculate the cable responses, which coincided with the wind tunnel test results very well. They concluded that the upper rivulet's oscillation within a certain region excited the RWIV.

2.5.3 Wind Flow Passing Yawed Dry Cable

Yeo and Jones (2008, 2012) investigated the three-dimensional characteristics of the flow around a yawed and inclined cylinder at the high Reynolds number using CFD. They observed that the shear layer beyond the separation line rolled up with a large span-wise velocity, forming a swirling flow structure behind the inclined cylinder.

The swirling flow structure alternatively developed on both sides of the cylinder, moved obliquely to the centreline, and shed, generating multiple moving forces on the yawed and inclined cylinder. This loading was the source of the aerodynamic instability of an inclined cable oblique to the wind.

2.6 Summary

From the data obtained through field measurement, wind tunnel test, numerical analysis, and CFD, the possible excitation mechanisms of the RWIV were summarized as: (1) new type of galloping caused by water rivulets position and movement; (2) vortex induced vibration at high reduced wind speed; (3) modification on the flow state caused by the rivulets; and (4) swirling flow traveling along the inclined circular cylinder.

(1) Hikami and Shiraishi (1988) first proposed the idea that the circumferential oscillation of upper rivulet, resulting in a periodic change in the cable cross-section, might be the reason of the RWIV. This idea was confirmed by Xu and Wang (2003), Gu and Du (2005), Gu (2009), Li et al. (2010), Du et al. (2013), and Chen et al. (2013). They concluded that the upper rivulet movement changed the aerodynamic forces coefficients, resulting in the cable instability. Yamacuchi (1990), Xu et al. (2006), Gu (2009), and Du et al. (2013) measured the negative slope in the lift force coefficient curve when the artificial upper rivulet was stuck at different positions of the cable model. Xu and Wang (2003), Wilde and Witkowski (2003), Cao et al. (2003), and Peil and Dreyer (2007) numerically analyzed the cable response using the measured lift force coefficients curve and concluded that the negative slope in the lift coefficient curve was the main reason

of the RWIV. However, Bosdogianni and Olivari (1996) hold the different opinion that it was not the movement but the position of upper rivulet that induced the new type of galloping. Verwiebe and Ruscheweyh (1998) pointed out that the lower rivulet were also essential for the RWIV.

(2) Except for the upper rivulet, the axial flow/vortex generated in the wake of inclined cable was also reported playing an important role in the RWIV. Matsumoto et al. (1990, 1992) first reported the existence of axial flow in the wake of inclined cable and concluded that the negative slope in the lift coefficient curve could be caused by the axial flow or the upper rivulet. Besides, Matsumoto et al. (1995, 1998) observed that the existence of the axial vortex would enhance the Karman vortex once in very several times and then generated the lower frequency vortex shedding. Finally, they suggested that the RWIV might be a new type of vortex induced vibration at high reduced wind speeds.

(3) Cosentino et al. (2003a) thought that when the cable moved downward (normal to the cable axis) the upper rivulet changed the flow state into one-bubble regime, and when the cable ascended the flow state returned to the sub-critical regime. This periodical variation in the flow state caused the cable unstable. Seidel and Dinkler (2006) considered the rivulet as a movable disturbance. The periodical disturbance generated a periodic lift force based on the "Prandtl tripwire", exciting the cable vibration. Besides, Cheng, et al. (2003, 2008), Boujard (2007), Jakobsen et al. (2012) and Nikitas et al. (2012) observed the dry galloping of an inclined cable, which exhibited similar characteristics as the RWIV. They indicated that the RWIV was related to the modification of the flow state.

(4) Yeo and Jones (2008, 2012) assumed that the swirling flow structure alternatively developed on both sides behind the inclined cylinder made the cable unstable. The swirling flow moving obliquely to the centreline and shedding alternately generated the lower frequency aerodynamic loading to excite the cable vibration.

Although extensive studies have been conducted, the exact excitation mechanism of the RWIV remains unclear. Many researchers reported that the rivulet plays an important role in the RWIV. However, there are different viewpoints about how this little rivulet affects the wind flow and consequently the aerodynamic forces of the cable.

CHAPTER THREE

REPRODUCTION OF RWIV IN A WIND TUNNEL

3.1 Introduction

Extensive wind tunnel tests have been conducted to investigate the RWIV. It is in general agreed that the circumferentially oscillating upper rivulet on the cable surface plays a crucial role in inducing this type of cable vibration. The wind tunnel tests can be categorized into two types by the different simulations of the water rivulet. One is to stick a solid artificial rivulet on the cable surface; the other is to spray real water forming the water rivulets on the cable surface. Sticking an artificial rivulet has been used to measure the aerodynamic force coefficients and then reveal the excitation mechanism, while spraying real water is mainly used to investigate the on-set conditions and the response characteristics of this type of cable vibration.

The artificial rivulet is usually made of aluminum, wood, or plastics. Its shape can be circle, semi-circle, ellipse, semi-ellipse, arc, or rectangle. The artificial rivulet has the advantage of easy control (in shape and position) and little effect on the experimental instruments. However, it also has some defects. The solid artificial rivulet may not reflect the actual water rivulet and the RWIV because the artificial rivulet could not oscillate on the cable surface and its shape remains unchanged during the RWIV, which are different with the real rivulet. Besides, the size of the artificial rivulets was much larger than the real water rivulet.

Spraying real water simulates the rainfall. Under the actions of the wind, gravity, and cable vibration the rain drops accumulate on the cable surface forming the rivulets. The simulated rivulets can freely oscillate and deform on the cable surface, which are almost the same as the real water rivulets on the stay cable.

To better understand how the upper rivulet excites this new type of cable vibration, detailed wind tunnel tests using the real water to simulate the rivulets are needed. In this thesis, three types of rivulet simulation methods using the real water were used to reproduce the RWIV in a wind tunnel. The effects of the flow rate of the rivulet, damping ratio, and initial condition of the cable on the RWIV were investigated. The effects of the upper rivulet on the aerodynamic damping ratio and on the wake flow of the inclined cable were also studied.

3.2 Experimental Set-up

3.2.1 Wind Tunnel

The wind tunnel tests were conducted in D-2 wind tunnel (see Figure 3-1) at Southwest Jiaotong University, located in Sichuan, China. It is an open-jet wind tunnel with a rectangular outlet section of 1.34 m wide and 1.54 m high, which can simultaneously simulate wind and rainfall. The maximal available wind speed is approximately 20 m/s. The distribution of the mean wind speed and the turbulence intensity in the outlet section were first measured point by point by the experimenters with a Cobra probe anemometer (made by Turbulent Flow Instrumentation) at the wind speeds (U) of 9.2 and 12.1 m/s. The results are shown in Figure 3-2. The

variations in the mean wind speed and the turbulence intensity in the outlet section were approximately 3% and 2%, respectively.

(a)
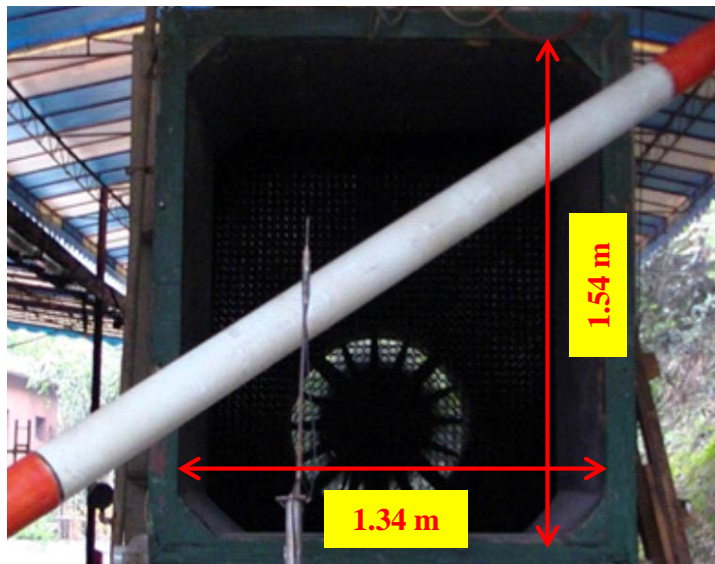
(b)

Figure 3-1. D-2 wind tunnel at Southwest Jiaotong University
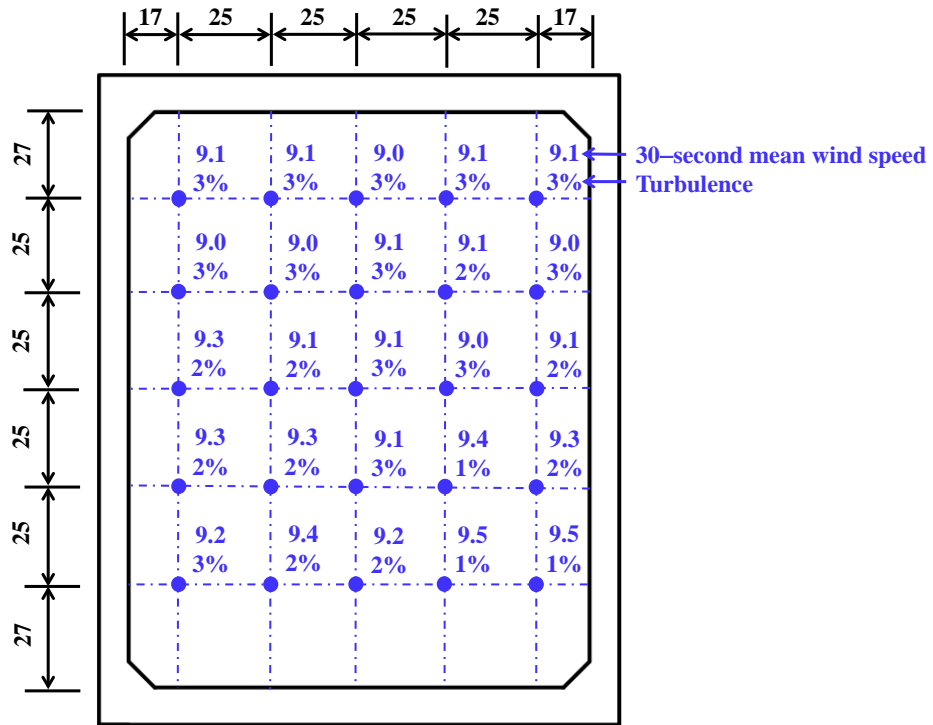
(a) $U = 9.2$ m/s
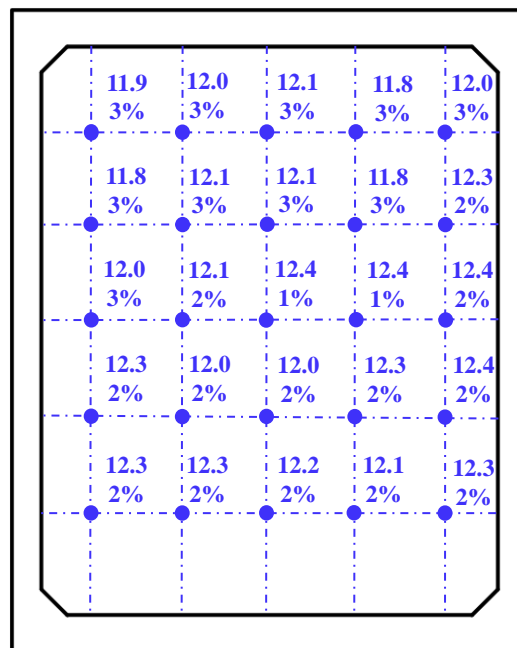
(b) $U = 12.1$ m/s

Figure 3-2. Wind speed and turbulence distribution in the outlet section of the wind

tunnel (length unit: cm; wind speed unit: m/s)

3.2.2 Cable Model

The cable model was made of a steel tube coated by high density polyethylene (HDPE), same as the stay cables used in real bridges. Figure 3-3 shows the section and cutaway view of the cable model. The cable model is 160 mm in diameter and 2.7 m in length, with a 2 m-long test segment in the middle and transition segments at both ends. The mass of the entire cable model was measured as 66.0 kg.

68 mm   80 mm

PE coat   Steel tube

(a) Cross-section view

350 mm   2000 mm   350 mm

Transition segment   Test segment   Transition segment
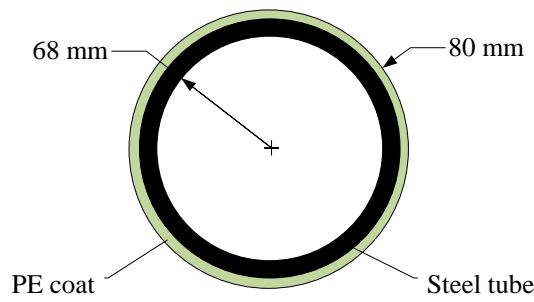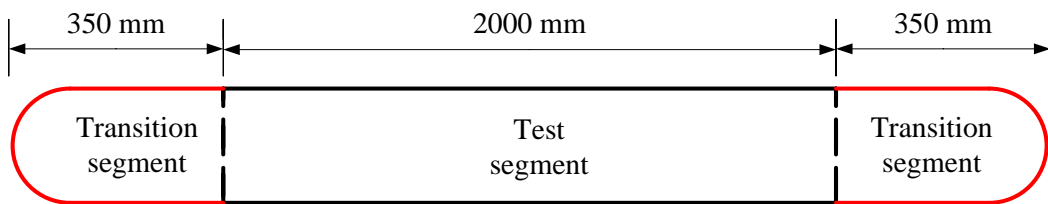
(b) Cutaway view

Figure 3-3. Cable model

The cable model was suspended about 1 m behind the outlet section at an inclined angle (α) of 32° and a yaw angle (β) of 35°, as shown in Figure 3-4, resulting in a relative yaw angle of 29.1° [$\beta^* = \sin^{-1}(\sin\beta\cos\alpha) = 29.1°$]. Figure 3-5 shows the cable supporting system. Four springs or two springs (without horizontal springs)

suspended the cable at both ends in the transverse direction, and a steel wire supported the cable in the longitudinal direction. The springs were mounted on a firm steel frame, which was fixed on the ground (not shown in the figure).
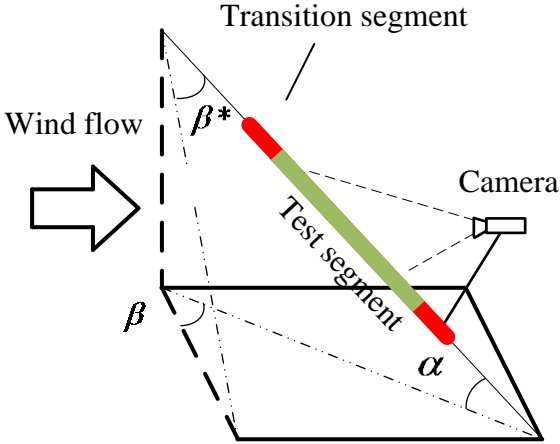
Figure 3-4. Cable geometry in wind tunnel
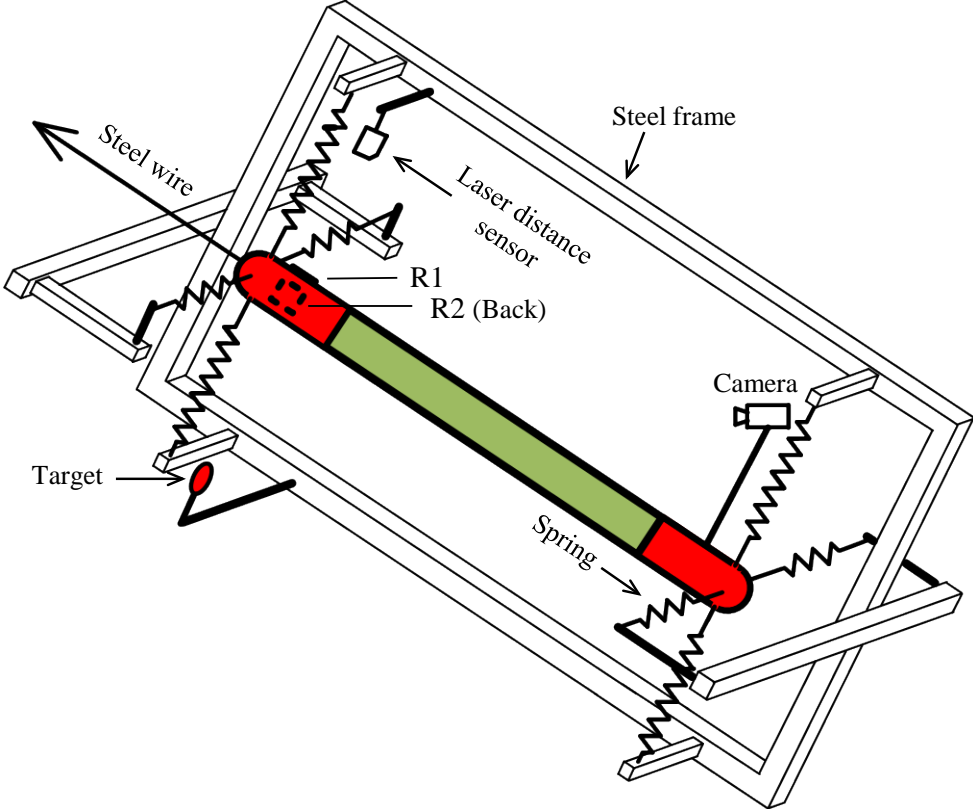
Figure 3-5. Cable supporting system

Two laser distance sensors with a 100 μm resolution were fixed on the frame with two reflectors at the top end of the cable (see Figure 3-5). One laser sensor and reflector 1 (R1) were employed to measure the cross-wind displacement of the cable (in the cable plane and perpendicular to the cable axis). The other laser sensor (not shown in the figure) and reflector 2 (R2) measured the horizontal displacement of the cable (perpendicular to the cable plane). The cable horizontal vibration was found to be very small. Therefore, only the cross-wind vibration was presented in this thesis and downward movement was set as positive.

A digital video camera (JVC-HD30AC) was mounted on the cable and located 1.2 m above the bottom end of the cable (Figure 3-5) such that it had no disturbance on the rivulet and the wake flow. A target with a ruler was fixed on the frame. The camera captured the rivulet, cable, and the target at the same time because the camera moved with the cable while the target remained steady during the experiment and the movement of the target captured by the camera actually represented the movement of the camera and the cable relative to the ground. In this manner, the camera could synchronously record the upper rivulet movement and the cable vibration. The identification of the rivulet movement and the cable vibration will be presented in Chapter Four.

3.3 Wind Tunnel Test

3.3.1 Different Types of Simulation of Water Rivulet

The water rivulets can be simulated by spraying water (Hikami and Shiraishi 1988; Matsumoto et al. 1992; Flamand 1995; Cosentino et al. 2003a; Gu and Du 2005; Li

et al. 2010a), guiding water lines on the cable surface (Wang et al. 2005; Alam and Zhou 2007), or their combination (Zhan et al. 2008).

Spraying water simulates the on-site rainfall. The flying raindrops blown by wind accumulate on the cable surface to form the upper and lower rivulets. Spraying water was widely used in previous wind tunnel studies to reproduce the RWIV (Hikami and Shiraishi 1988; Flamand 1995; Cosentino et al. 2003a; Gu and Du, 2005; Li et al. 2010a), and its effectiveness has been sufficiently verified.

In the guiding water lines technique, small pipes are placed at the upper end of the cable. The water flows downward along the cable because of gravity and wind pressure, thereby forming the upper and lower rivulets as Figure 3-6 shows. This simulation approach is also effective and has a significant advantage in wind tunnel tests because the raindrops are avoided during the test. Besides, the size of the rivulets can be controlled by changing the cross-section of the plastic pipes.

(a)   (b)
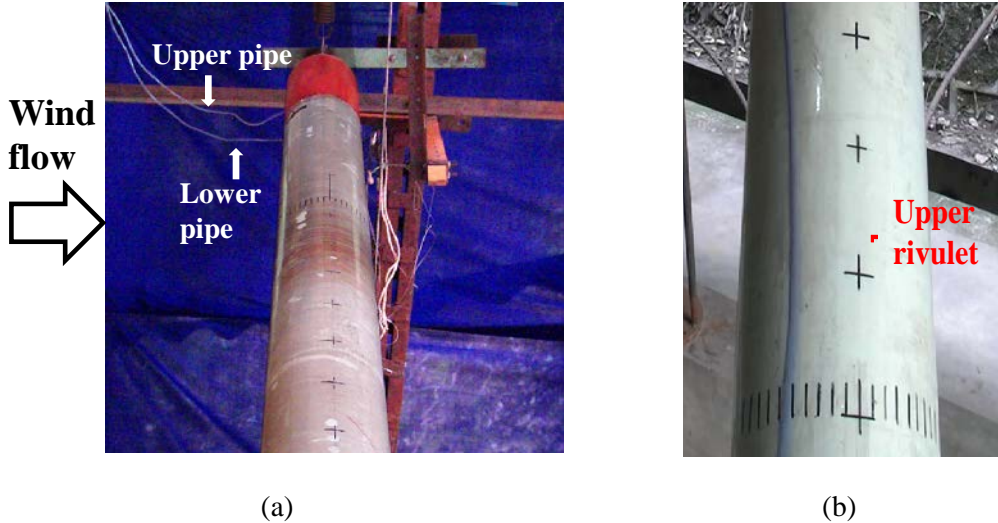
Figure 3-6. Simulation of upper and lower rivulets

On-site rivulets typically contain two parts: the newly gathered rivulets from the raindrops and the formed rivulets flowing down from a higher cross-section. Therefore, simultaneously spraying water and guiding water lines might be close to the real rivulet situation, as adopted by Zhan et al. (2008).

In the present study, the aforementioned three methods were first adopted under the wind speed of 12.1 m/s and the rivulets flow rate (Q) of 7.46×10^{-7} m^3/s. The measurement of Q will be introduced in Section 3.3.3. The Reynolds number was derived as $R_e = UD/v = 1.3 \times 10^5$, where v denotes the kinematic viscosity.

The experimental results show that the wettability of the cable surface, which enables the oscillation of the rivulet, was crucial for the RWIV as reported by Flamand (1995). All three types of rivulet simulations can effectively reproduce the RWIV when the rivulet could freely vibrate on the cable surface. The time history of the cable displacement is shown in Figure 3-7. The amplitudes of the simulated cable vibrations obtained using the three methods were 63.6, 76.2, and 73.1 mm, respectively, which are very close to each other. The dominant frequencies of the cable vibrations were the same as the fundamental frequency of the cable.

Guiding water lines is adopted hereinafter because the flying raindrops may damage the experimental facilities.
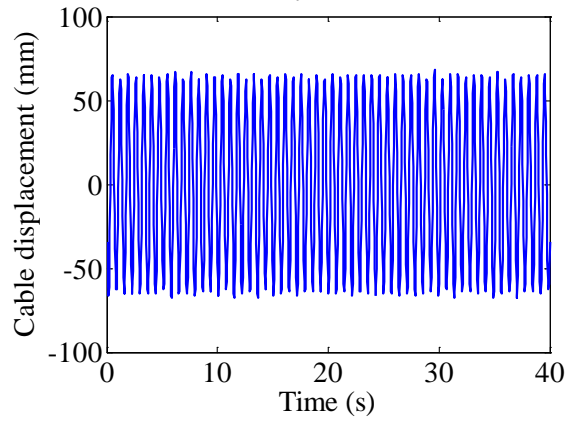
(a) Spraying water only
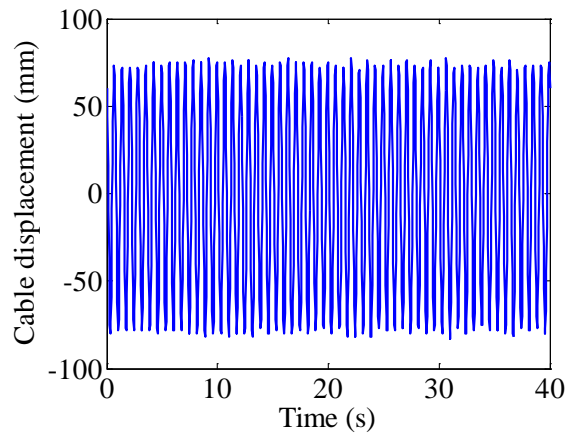
(b) Guiding water lines only
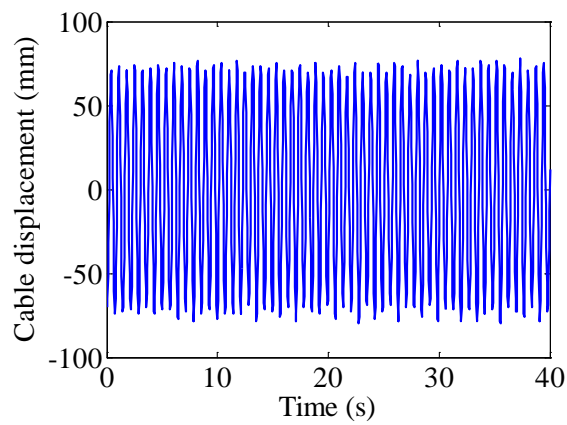
(c) Spraying water and guiding water lines

Figure 3-7. RWIV of the cable reproduced by different rivulet simulations

3.3.2 Effects of the Upper and Lower Rivulets on the RWIV

The effects of the upper and lower rivulets on cable vibration were investigated. The upper and lower rivulets were alternatively switched on/off and the cable responses were measured under the wind speed of 11.4 m/s. The cable vibration time history is shown in Figure 3-8(a), where "On-1" and "Off-1" denote that the upper rivulet is turned on and off, respectively, and "Off-2" means the lower rivulet is switched off. Before the test, no large vibration was observed for a long time when the lower and upper rivulets were off. At the beginning of the test, both the lower and upper rivulets were turned on. RWIV then developed and the vibration amplitude steadily increased. When the upper rivulet was turned off at 110 s, the cable vibration began to decrease rapidly. At 180 s, the upper rivulet was turned on again and the cable vibration also increased. After a relatively large amplitude vibration was reached, the lower rivulet was turned off at 230 s. However, the vibration was unaffected by this action. Lastly, the upper rivulet was turned off at 255 s, and the cable vibration began to decrease dramatically to a small amplitude. Similar results were observed under the wind speed of 13.0 m/s as Figure 3-8(b) shows. In this case, the lower rivulet had been turned on for a long time before the beginning. In the two wind speed cases, the reduced velocity ($V_r = U / fD$) is calculated as 56 and 64, respectively. The flow rates of the upper and lower rivulets were the same as 7.46×10^{-7} m^3/s.
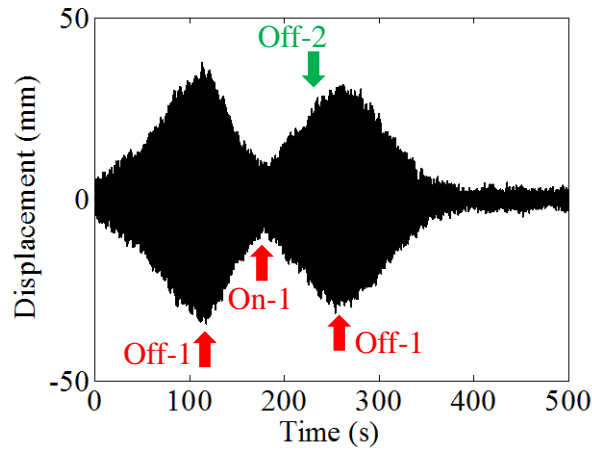
(a) Wind speed is 11.4 m/s
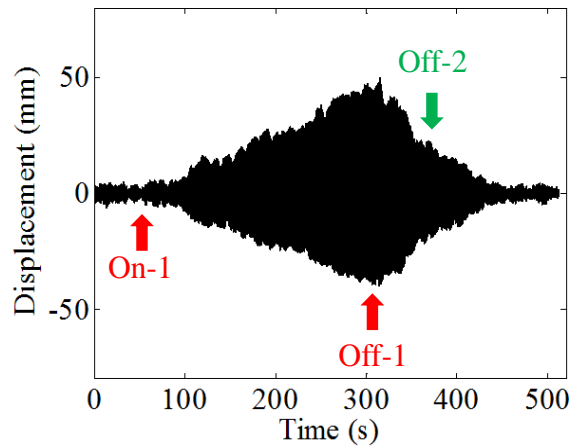
(b) Wind speed is 13.0 m/s

Figure 3-8. Effects of upper and lower rivulets on the RWIV

The above observation clearly demonstrates the importance of the upper rivulet in large cable vibration. Only when the upper rivulet circumferentially oscillated on the cable surface did large cable vibrations occur. The lower rivulet minimally affected the cable vibration and was observed to be static, which was consistent with previous studies (Ni et al. 2007; Hikami and Shiraishi 1988; Cosentino et al. 2003a; Li et al. 2010a). Therefore, the existence of the upper rivulet was an on-set condition of the RWIV.

3.3.3 Effect of Rivulet Flow Rate on the RWIV

The flow rate of the water rivulet is the water volume passing the outlet of guiding pipe per unit time. It is determined by the hydraulic head pressure difference and the inner diameter of the guiding pipe. In this study, the effects of the rivulet flow rate on the RWIV were investigated by changing the inner diameter of the guiding plastic pipes and the hydraulic head pressure difference remained unchanged. Four plastic pipes with different inner diameter were used to guide water lines to reproduce the RWIV in the wind tunnel. The flow rate of the four plastic pipes were measured as 0.0925 mL/s, 0.2774 mL/s, 0.7463 mL/s, and 1.6313 mL/s, corresponding to cases Q_1 to Q_4. Cases Q_1 and Q_2 represented the light rainfall. In particular, for case Q_1 there was only approximate three water drops flowing out of the guiding pipes per second, which indicates the drizzle on-site. Case Q_3 and Q_4 simulated the moderate rainfall. Figure 3-9 shows the simulated upper rivulet on the cable surface with different flow rates. For the small water rivulet, such as case Q_1, the upper rivulet formed at the lower wind speed (approximate 8.0 m/s), and the formed upper rivulet was more stable and static on the stationary cable model. For the bigger rivulet, such as case Q_4, the upper rivulet formed only when the wind speed was higher than 9.5 m/s. It arbitrarily spread and gathered and randomly oscillated on the cable surface even when the cable model was stationary.

Figure 3-10 shows the vibration amplitude of the cable with the four flow rates under different wind speeds. It can be seen that the RWIV occurred when the wind speed was higher than 10 m/s. In particular, the RWIV of case Q_3 started when the wind speed was 9 m/s, lower than the other cases. For case Q_1 the large RWIV disappeared

at the wind speed of 16 m/s. The upper critical wind speed of cases Q_2 to Q_4 was not observed because of the limitation of the maximum wind speed of the wind tunnel.

(a) Q_1

(b) Q_2

(c) Q_3

(d) Q_4
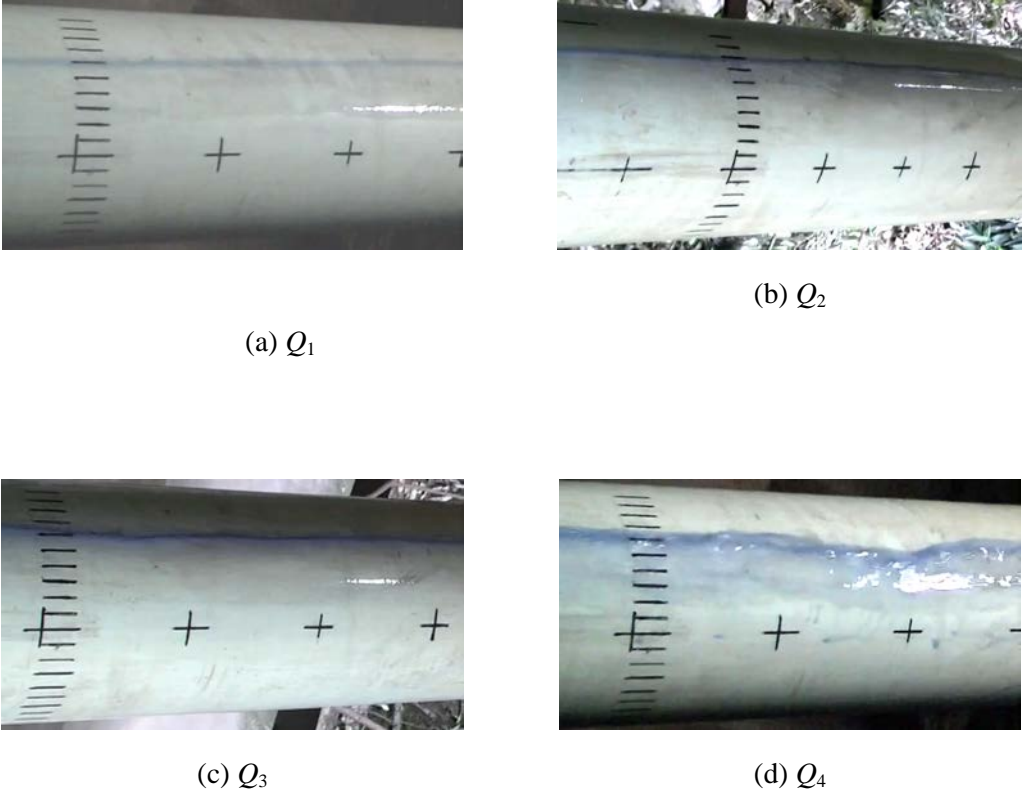
Figure 3-9. Rivulet on cable surface for different flow rates
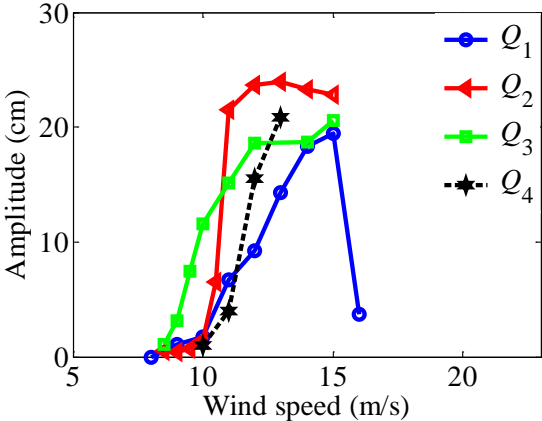
Figure 3-10. Amplitude of cable vibration versus wind speed for different flow rates

It is worth to note that the amplitude shown in Figure 3-10 does not represents the maximal amplitude of the RWIV under each wind speed. When the cable vibration was close to the 25 cm, it had to be stopped even through some of them did not reach the maximal amplitude because the maximal available cable displacement of the experimental facility was approximate 26 cm. Besides, the amplitude of the RWIV was complicated and sensitive. It was significantly affected by the movement state of the upper rivulet and the initial condition of the cable. Under the same wind and rain conditions, the amplitude of the RWIV would be different, which will be investigated in detail in Chapter Five. In this study, case Q_3 was prone to large amplitude RWIV than other cases. It was thus chosen as the basic case to reveal the excitation mechanism of the RWIV. For cases Q_1 and Q_4, the occurrence of large RWIV was relatively difficult and need a larger initial excitation. The effects of the initial condition of the cable on the RWIV will be discussed in Section 3.3.4.

3.3.3 Effect of Damping Ratio on the RWIV

Many factors such as the damping ratio, cable fundamental frequency, initial conditions of the cable and the rivulet, surface condition of the cable, intensity of rainfall, and wind conditions (wind speed, direction, and turbulence), would influence the amplitude of the RWIV. Among them, damping ratio is one of the most significant factors. In this section, the effect of the damping ratio on the cable amplitude is experimentally examined.

The damping ratio of the cable system was adjusted by adding rubber bands on the springs, as shown in Figure 3-11. A total of 18 cases (D1 to D18) were considered. In each case, three more pairs of rubber bands were added to the springs. The free

vibration test was first conducted. The cable model was given an initial displacement and then released suddenly. It then vibrated freely. The displacement was measured during the decay of cable vibration. Then the RWIV was reproduced under the same rain−wind conditions ($U = 12.1$ m/s and 14.1 m/s, $Q = 7.46 \times 10^{-7}$ m^3/s) in the wind tunnel. The fundamental frequency and the damping ratio of each case were obtained using the free vibration test, and the results are listed in Table 3-1. The fundamental frequency increased by approximately 5%, and the damping ratio increased from 0.11% to 0.49%. This increase corresponds to an increase of Scruton number (S_c) increase from 13.6 in D1 to 61.3 in D18. Figure 3-12 shows the amplitude of the RWIV versus the damping ratio. The amplitude of the RWIV decreased with an increase in S_c, which agrees well with the previous studies such as Gu and Du (2005) and Zhan et al. (2008).

Figure 3-11. Rubber band on spring
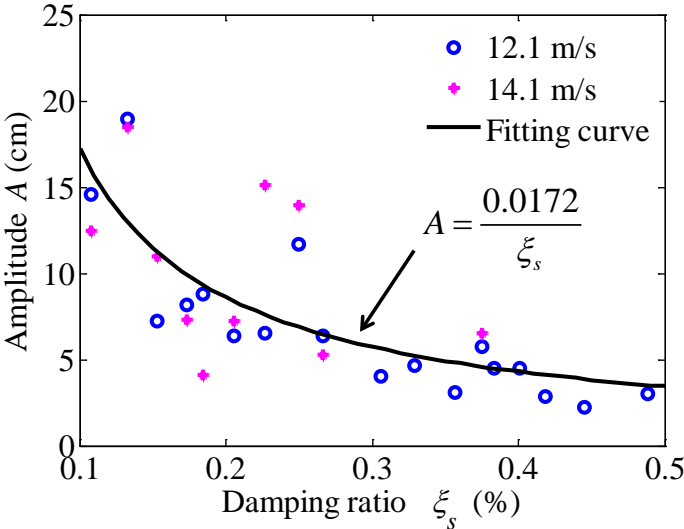
Figure 3-12. RWIV amplitude versus damping ratio

56

Table 3-1. Frequency and damping ratios for various rubber band cases

Case	f (Hz)	ξ (%)	S_c	Case	f (Hz)	ξ (%)	S_c
D1	1.3672	0.11	13.6	D10	1.4140	0.28	34.6
D2	1.3750	0.13	16.7	D11	1.4140	0.31	38.5
D3	1.3750	0.15	19.2	D12	1.4219	0.33	41.3
D4	1.3828	0.17	21.7	D13	1.4297	0.36	44.7
D5	1.3828	0.18	23.1	D14	1.4297	0.38	48.1
D6	1.3828	0.21	25.8	D15	1.4297	0.40	50.4
D7	1.3906	0.23	28.5	D16	1.4375	0.42	52.5
D8	1.4062	0.25	31.4	D17	1.4375	0.45	55.9
D9	1.4062	0.27	33.7	D18	1.4453	0.49	61.3

3.3.4 Effect of Initial Vibration on the RWIV

Given that the initial condition of the cable vibration significantly affected the amplitude of the RWIV, in this section, this effect is investigated by applying different initial displacement manually. The tests were classified into three groups: (1) relatively large damping ratio ($\xi_s = 0.38\%$, $S_c = 48.1$); (2) moderate damping ratio ($\xi_s = 0.28\%$, $S_c = 34.6$); and (3) small damping ratio ($\xi_s = 0.13\%$, $S_c = 16.7$).

Figure 3-13 shows the response of the cable model with a relatively large damping ratio. In Figure 3-13(a), the cable was excited to vibrate with the amplitude of approximate 18 mm and 28 mm. After the disturbance removed, the cable vibration decayed slowly, similar to the damped free vibration and the RWIV of the cable

could not be successfully excited. However, when the cable was excited to vibrate at a larger amplitude vibration, approximately 33 mm, as shown in Figure 3-13(b), the RWIV of the cable was successfully excited even through the inherent damping ratio was the same.
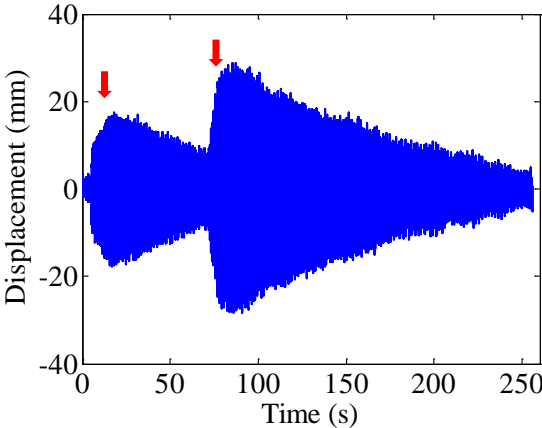
(a)
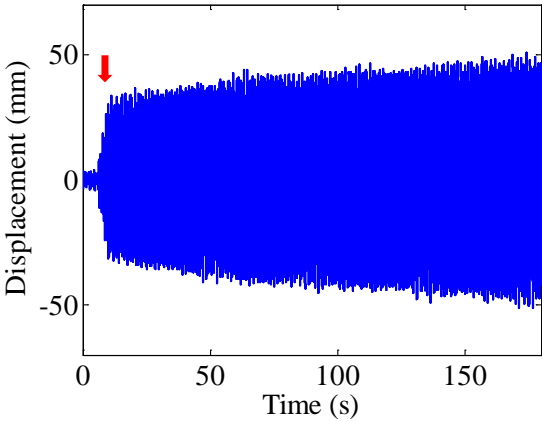
(b)

Figure 3-13. Time history of the cable displacement under different initial excitation

(ξ_s = 0.38% and S_c = 48.1; ↓ : Artificial excitation)

Figure 3-14 shows the response of the cable model with the moderate damping ratio. The RWIV of cable was successfully excited when the cable had a disturbance of 18

mm.
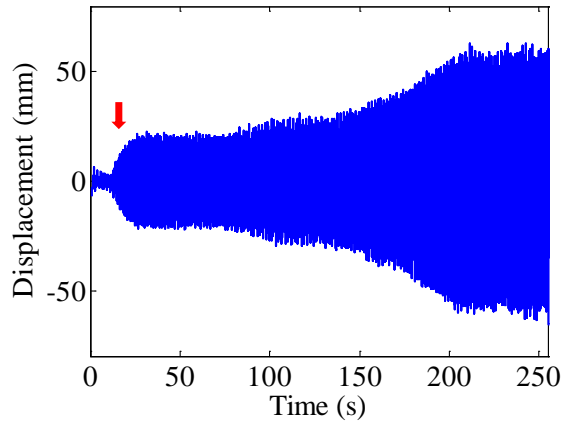
Figure 3-14. Time history of the cable displacement under initial motivation

($\xi_s = 0.28\%$ and $S_c = 34.6$; ⬇: Artificial excitation)

When the cable had a small damping, the RWIV of the cable could grow from stationary, even without any initial disturbance, as Figure 3-15(a) shows. However, if the cable was excited at a large amplitude at the beginning as shown in Figure 3-15(b), the RWIV amplitude of the cable could be much larger.

The above results show that the initial condition of the cable has a significant effect the on the RWIV. For a large damping ratio, the initial condition of the cable even determines whether the RWIV could occur or not. Larger damping ratio, larger initial disturbance is required to excite the RWIV. If the damping ratio of the cable is very small, the RWIV could be excited even without any initial disturbance.
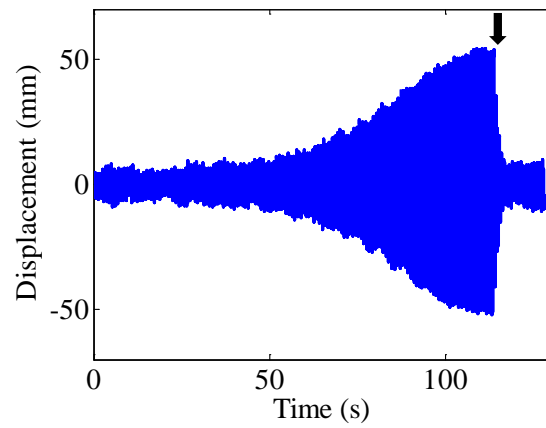
(a)
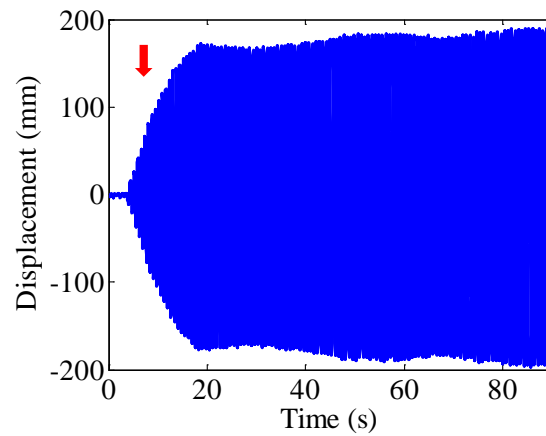
(b)

Figure 3-15. The time history of cable under different initial motivation

($\xi_s = 0.13\%$ and $S_c = 16.7$; ↓: Artificial excitation; ↓: Stop)

3.3.5 Effect of the Rivulets on the Aerodynamic Damping

The aerodynamic damping is an important parameter to evaluate the stability of the cable; it can be approximately estimated from the following equation:

$$\xi_{ae} = \xi_t - \xi_s \qquad \text{(3-1)}$$

where ξ_{ae}, ξ_t, and ξ_s denote the aerodynamic damping ratio, total damping ratio, and inherent structural damping ratio, respectively. The total damping ratio is calculated as:

$$\xi_t = \frac{1}{2\pi(m-n)} \ln(\frac{A_n}{A_m}) \qquad \text{(3-2)}$$

where m and n are the cycle number, A is the cable displacement amplitude.

The effect of the rivulet on the aerodynamic damping of the cable model is investigated by free vibration testing. The time history of the dry cable without any incoming wind flow or rivulet is shown in Figure 3-16(a). The structural damping ratio (ξ_s) of this cable model was identified as 0.42%, a relatively large damping ratio for stay cables. A similar free vibration test was then conducted in the wind flow (U = 12.1 m/s) without any rivulet. The time history of the cable displacement is shown in Figure 3-16 (b) and it seems that the cable vibration decays more quickly in the case. The total damping ratio (ξ_t) in the wind flow was identified as 0.49%. This indicates that the wind flow generated a positive damping and the aerodynamic damping ratio (ξ_{ae}) was calculated as $\xi_t - \xi_s$ = 0.07%. At last, the cable with the rivulets was tested in the same wind flow (U = 12.1 m/s). The time history is shown in Figure 3-16(c). It is obvious that the cable vibration decayed much slower than the previous two cases. The new total damping ratio (ξ_t) was identified as 0.09%. The new aerodynamic damping ratio is calculated as 0.09% − 0.42% = −0.33%,

indicating that the existence of the upper rivulet would significantly reduce the aerodynamic damping of the wind flow. The reduced aerodynamic damping ratio is calculated as $0.07\% - (-0.33\%) = 0.40\%$, which agrees well with the previous study such as Zhan et al. (2008).
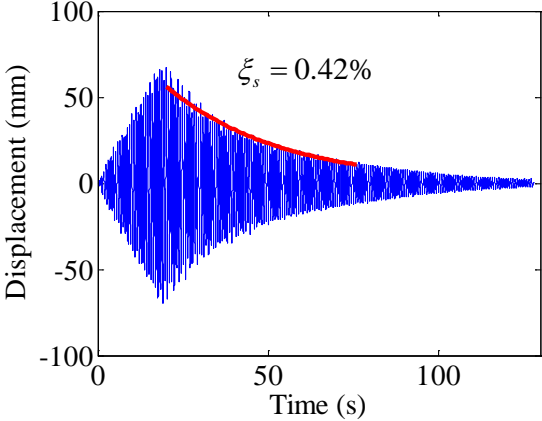
(a) Free vibration of dry cable
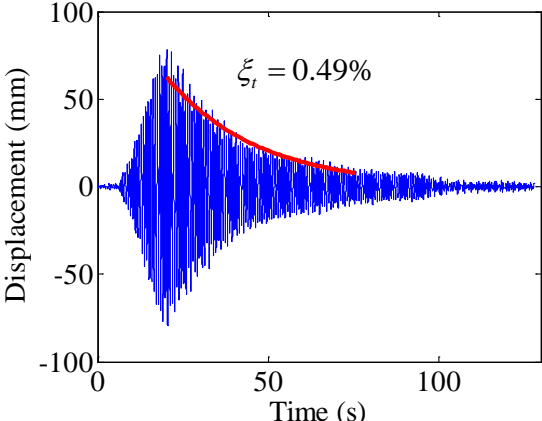
(b) Free vibration of dry cable in wind flow
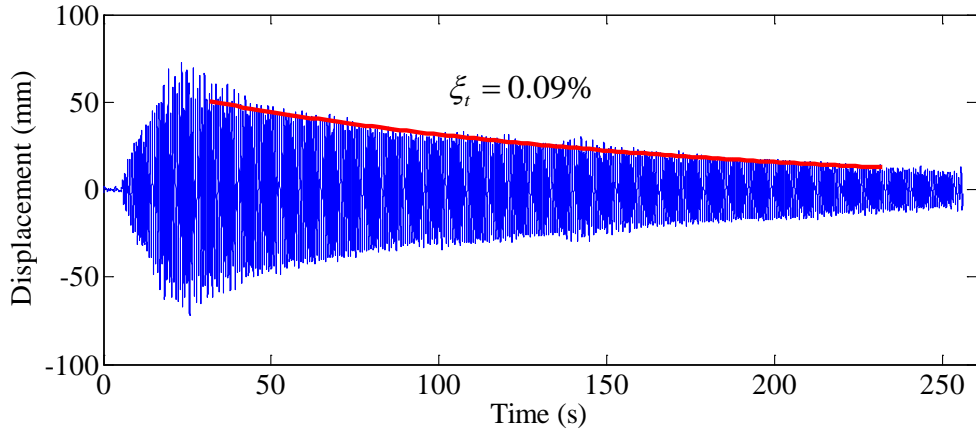
(c) Free vibration of cable with rivulet in wind flow

Figure 3-16. Effects of the rivulets on the damping ratio

The reduced aerodynamic damping, the negative aerodynamic damping caused by the upper rivulet, might be a potential factor in the suppression of the RWIV.

3.3.6 Wind Speed in the Wake of Inclined Cable

To investigate the effects of the rivulet on the vortex shedding and on the wake flow, the wind speed in the wake of the stationary cable model was measured by two Copra anemometers when the cable was dry and there was an upper rivulet on its surface.

Figure 3-17 shows the position of the two measurement points in the vertical plane along the wind direction. Since the cable was inclined and blown by the yaw wind, the test section of the cable model was oval in this plane. Point 1 was located at 49.8 cm behind and 14.1 cm higher than the cable, and Point 2 was located at 88.0 cm behind Point 1.
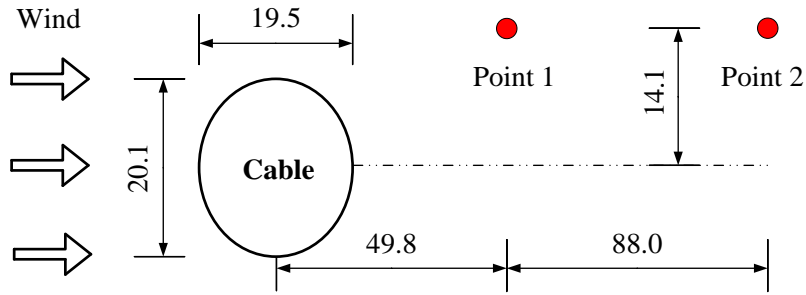
Figure 3-17. Wind speed measurement (unit: cm)

The auto-power spectral density (PSD) of the measured wind speed was calculated and shown in Figure 3-18. In this figure, the horizontal axis is the reduced frequency, which is defined as $f_r = f D_e / U$, where $D_e = 0.201$ m is the effective height of the cable cross-section. The wind speed at the two measurement points exhibits similar characteristics. When the cable was dry, the dominant reduced frequency was 0.20, corresponding to the classical Karman vortex shedding frequency in the sub-critical regime (Zdravkovich 1997). However, when there was an upper rivulet on the cable surface, the dominant frequency almost disappeared, which indicates that the existence of the upper rivulet suppressed the classical Karman vortex shedding. The disappearance of the vortex shedding implies that the existence of the upper rivulet might modify the air boundary layer state because the vortex shedding is directly related to the boundary layer state.
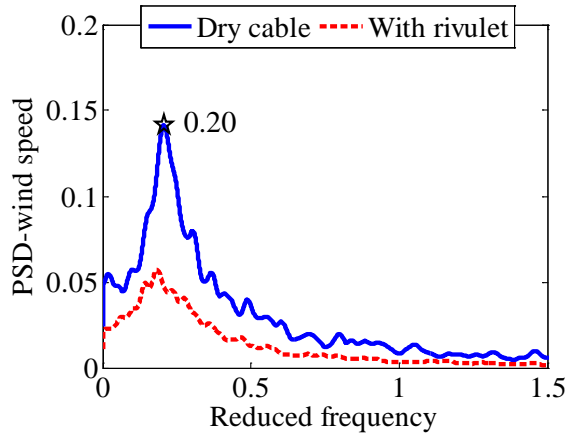
(a) Point 1
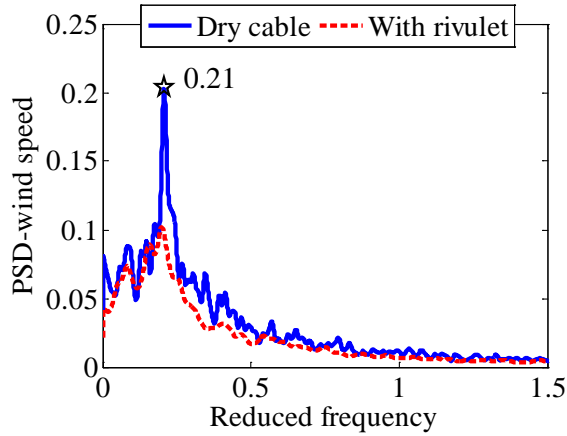
(b) Point 2

Figure 3-18. PSD of wind speed in the wake

3.4 Summary

In this Chapter, the RWIV of the inclined cable were successfully reproduced in the wind tunnel. The effects of different factors, such as the flow rate of the rivulet, damping ratio, and initial condition of the cable on the RWIV were investigated. The aerodynamic damping ratio was estimated and the wake flow of the inclined cable was measured when there were rivulets on the cable surface. The main conclusions

can be drawn as follows:

(1) Guiding water lines is effective to reproduce the RWIV in wind tunnel tests and the results are similar to that by spraying real water.

(2) The upper rivulet is directly associated with the RWIV, while the lower rivulet has no effect on the RWIV.

(3) The RWIV could occur within a wide range of flow rate. Large RWIV was observed even when the flow rate of the water rivulet was extremely small. However, when the water rivulet has moderate flow rate, corresponding to the moderate rainfall, the stay cable is more prone to large RWIV.

(4) The amplitude of the RWIV decreases with the increase of cable's damping. The initial condition of the cable affects the amplitude of the RWIV, especially when the damping ratio of the cable is relatively large.

(5) The circumferentially oscillating upper rivulet significantly reduces the aerodynamic damping of the inclined cable system.

(6) The existence of the upper rivulet on the cable surface suppresses the classical Karman vortex shedding.

CHAPTER FOUR

IDENTIFICATION OF RIVULET MOVEMENT AND THICKNESS USING DIGITAL IMAGE PROCESSING METHOD

4.1 Introduction

Many researchers believe that the upper rivulet plays the most important role in the RWIV. However, the excitation mechanisms of the RWIV are still not fully understood because there is limited information of the rivulet. The rivulet has become a crucial factor in understanding the RWIV of cables.

Up to now, most of the studies on the rivulet have been done using the computational fluid dynamics method. Lemaitre et al. (2007, 2010) proposed a lubrication theory-based numerical model to simulate the evolution of a water film around a cylinder and predicted the rivulets' location and wind speed range for the rivulets' existence. Robertson et al. (2010) and Taylor and Robertson (2011, 2015) combined the discrete vortex method and lubrication theory to calculate the growth of the rivulets on a cable surface under combined effects of pressure, shear, surface tension and gravity and investigated the effects of the initial water film thickness and the attacking angle on the development of rivulets. Bi et al. (2013) combined the lubrication and single-mode system vibration theories and derived the

two-dimensional coupled equations to calculate the evolution of the water film. Cheng et al. (2015) simulated the whole formation process of the water rivulets and categorized the rainwater morphology into four patterns over the analysis of the entire evolution process.

Nevertheless, experimental studies on the rivulet are very limited because the rivulet is considerably small, thin, and sensitive to the wind flow. To the best knowledge of the author, only few experiments have been carried out to measure the upper rivulet in literature. Cosentino et al. (2003a) measured the thickness and movement of the upper rivulet using eight pairs of wires. Li et al. (2010a) and Chen et al. (2013) employed an ultrasonic technique to measure the shape, thickness, position, and movement of the rivulets on an inclined stay cable model in a wind tunnel. However, the wires used by Cosentino et al. (2003a) had disturbance on the formation of rivulet and the wind flow. Li et al. (2010a) measured the rivulet at specific sections of the cable, and the rivulet distribution on the cable was not available.

Under the circumstance, the non-contact digital image processing technique has potential to avoid the aforementioned disadvantages. The technique has advantages of the non-intrusion, non-destruction, multi-point measurement, high resolution, and cost-effectiveness. For these reasons, it has been applied to the displacement or distance measurement. For example, Lee and Shinozuka (2006) developed the method to measure the dynamic displacement of a flexible bridge. Pankanin et al. (2007) applied it to quantitatively determine the geometric parameters of the Karman vortex street. Zhou et al. (2012) used it to measure the cable vibration of a real cable-stayed bridge. Choi et al. (2011) demonstrated the precision and

cost-effectiveness of the digital image processing method in measuring structural dynamic displacement.

In this chapter, the digital image processing method is developed and adopted to measure the cable displacement and the position and thickness of the rivulet on the cable model during the RWIV. The large RWIV of the model was reproduced by colored water rivulet in Chapter Three. The variation of the upper rivulet on the cable model was recorded using a digital video camera. Through the digital image processing, the time history of the cable displacement and the upper rivulet' vibration and thickness along the entire cable was obtained. During this test, the movement of the rivulet was not disturbed. Finally, the characteristics of the rivulet movement and thickness during the RWIV were investigated. The results will help elucidate the excitation mechanism of the RWIV of cables, which will be detailed in Chapter Seven.

4.2 Wind Tunnel Test

The wind tunnel tests were described in Chapter Three. Two flexible plastic pipes guided two water lines at the top end of the test segment (Figure 3-6) to simulate the upper and lower water rivulets, respectively. The water rivulets were colored in blue thus more distinguishable from the cable. Black marks were drawn on the cable surface of the test segment as reference to indicate the location of the rivulet during the RWIV. The fundamental frequency of the cable was identified as 1.37 Hz in free vibration tests and the damping ratio was 0.05%. The corresponding Scruton number

was calculated as $S_c = \dfrac{4\pi m\xi}{\rho D^2} = 6.28$.

A digital video camera was mounted 1.2 m above the bottom end of the cable (see Figure 3-5) such that it had no disturbance on the rivulet and wake flow. It moved with the cable and recorded the rivulet during the RWIV. The video camera captured 25 frames per second. Each frame had the resolution of 720 (height) × 1280 (width) pixels. The identification of the upper rivulet's movement and thickness will be introduced in detail in next section. Besides, a target with a ruler was fixed at the suspending frame so that the camera was able to simultaneously measure the relative movement between the target and the camera.

Images in the video clip are very sensitive to lighting. The same color under different lighting displays differently in digital images. Therefore, the lighting system was carefully adjusted to make the tests under uniform lighting condition during this testing.

4.3 Digital Image Processing Method

When the RWIV of the cable occurred, the upper rivulet moving in the circumferential direction on the cable and the stationary target were recorded by the digital camera. The video clips were processed to identify the rivulet position and thickness and the cable displacement, respectively.

4.3.1 Identification of Rivulet Position

The rivulet position is identified via three steps, namely, image pre-processing, rivulet identification, and rivulet locating.

Step 1: Image pre-processing

The recorded video clip is first converted into a series of images. The video camera used in this test captures 25 frames per second and each frame has 720 (height) $\times$ 1280 (width) pixels. The frames of the video clip are converted into a series of RGB images. RGB refers to the three hues of light (red, green, and blue) of each pixel, which range from 0 to 255 and can form any color by mixing together. For example, three intensities of 255 create the white color and three zeroes present the black. The k-th image can be represented as a three-dimensional matrix I^k with the size of 720 $\times$1280$\times$3, which corresponds to the three RGB intensities of each pixel. These images are named as raw images.

The raw images contain a big region irrelevant to the cable (see Figure 4-1). They are then cropped such that only the key area including the cable with rivulet remains. Consequently, the computational region in each image is reduced. To make sure the cable model located at the same position in all cropped images, one particular crossing point on the cable surface is chosen as the reference point in all images (see Figure 4-1). Its position in image k (or I^k) is (r_k, c_k), where r_k and c_k denote row and column numbers of the reference point, respectively. The reference point is identified by examining the neighborhood of the point, which is a 51×51 pixel

square in this thesis (see Figure 4-1). In the first raw image, the position of the reference point (r_1, c_1) is defined by the user. The neighborhood is determined such that its center is located at (r_1, c_1). The RGB of the neighborhood, denoted as I_R^1, is a three-dimensional matrix of 51×51×3. In the subsequent image, for example I^k, a 51×51 pixels square matching I_R^1 best is found and its center (r_k, c_k) is the reference point of I^k. That is,

$$(r_k, c_k) = \left\{ (r,c) \middle| \min \left(\left| I_R^k - I_R^1 \right| \right) \right\}$$ (4-1)

where

$$I_R^1 = I^1(r_1, c_1)_{51\times51\times3}$$ (4-2)

$$I_R^k = I^k(r,c)_{51\times51\times3}$$ (4-3)

I_R^1 is the RGB matrix of the neighborhood of the reference point in I^1 with the central point at (r_1, c_1), and I_R^k is the RGB matrix of a 51×51 pixels square in I^k with the central point at (r,c). When $\left| I_R^k - I_R^1 \right|$ reaches the minimum, the central point of I_R^k (r_k, c_k) will be identified as the reference point of I^k.
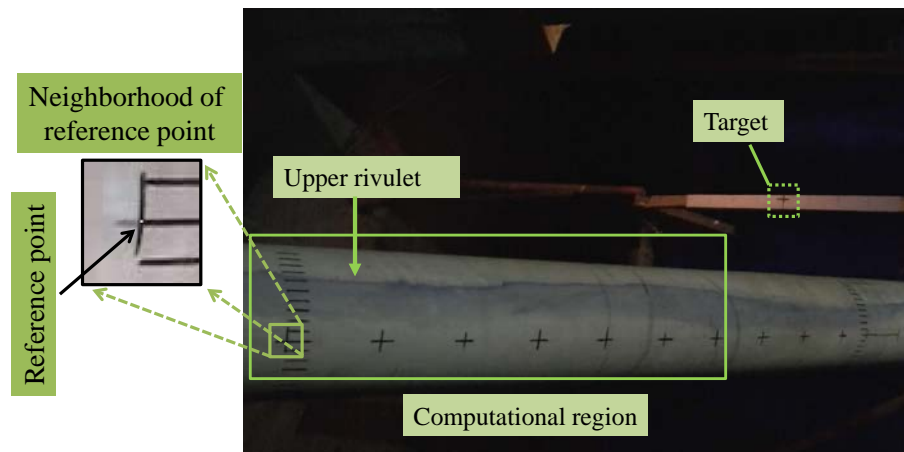
Figure 4-1. A raw image from the video clip

After the reference point is identified, the identical computational region is determined in all images. In this thesis, the computational region is a 200 (height) × 750 (width) pixels rectangle. The reference points in all cropped images are located at (150, 50). The origin (1, 1) is located at the upper-left corner of the image.

Subsequently, the contrast of the cropped images is enhanced with the histogram equalization method (Wang et al. 1999) to make the rivulet more distinguishable. Finally, the cropped and enhanced RGB images are converted into a grayscale image, as shown in Figure 4-2. The three intensities (R, G and B) of each pixel in the RGB image are translated to one gray intensity in the grayscale image (gray intensity = $0.2989 \times R + 0.5870 \times G + 0.1140 \times B$). The grayscale image, hereinafter, is referred to as the objective image. The objective image, a collection of 200×750 discrete pixels, is smoothed by the two-dimensional (2D) Gaussian filter, whose impulse response is a Gaussian function and efficient to filter out the noise with Gaussian distribution. Figure 4-3 shows a 2-D 5×5 discrete Gaussian kernel used in this study. The

200×750 matrix is convolved with the 5×5 Gaussian kernel. The filtered objective image is denoted by a two-dimensional matrix (A_0^k) with the size of 200 (row) $\times$ 750 (column), where k denotes the k-th image. Each item in the matrix represents the grayscale intensity of the pixel (black has the weakest intensity 0 and white at the strongest 255). As the water rivulet was colored in blue, the rivulet appeared darker than the surrounding white cable surface in the grayscale images. Consequently, the intensity of the rivulet is weaker and the corresponding items in matrixes A_0^k are smaller than others.
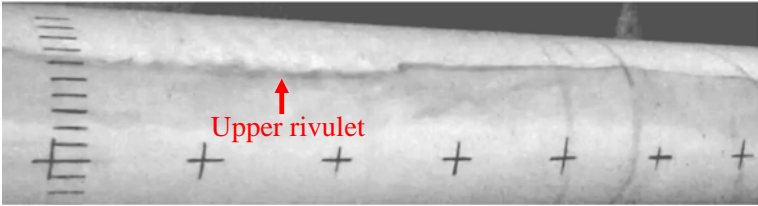
Figure 4-2. Cropped and enhanced grayscale image

$$\frac{1}{331} \begin{array}{|c|c|c|c|c|} \hline 1 & 4 & 7 & 4 & 1 \\ \hline 4 & 20 & 33 & 20 & 4 \\ \hline 7 & 33 & 55 & 33 & 7 \\ \hline 4 & 20 & 33 & 20 & 4 \\ \hline 1 & 4 & 7 & 4 & 1 \\ \hline \end{array}$$

Figure 4-3. Discrete two-dimensional Gaussian function

Step 2: Identifying rivulet in the image

The background of upper rivulet is slightly different in different objective images. To eliminate this effect, the background is removed by deducting the averaged values of the adjacent images as

$$A^k = A_0^k - avg(A_0^{k-10}, \cdots, A_0^{k+10}) \qquad (4\text{-}4)$$

where A^k and A_0^k denote the intensity matrixes after and before removing the background of the k-th image, respectively. The background of 21 adjacent images (approximately one period of the rivulet vibration) is averaged and deducted. As explained before, the intensity values in A^k where the rivulet is located are smaller than other items. In addition, they are also smaller than those in the previous (A^{k-1}) and succeeding images (A^{k+1}) at the same location because of the movement of the rivulet. Consequently, the rivulet location can be identified by the following two means under the ideal conditions: 1) to determine the minimal intensity in matrix A^k and 2) to find the maximal reduction of A^k from A^{k-1}. However, we have observed that both are significantly affected by noise in practice.

Here, the two approaches are integrated as follows:

(1) Calculate the intensity change as $\Delta A^k = A^k - A^{k-1}$.

(2) For each column j, the intensity is A_j^k and intensity change is ΔA_j^k.

(3) Obtain the local minimums of A_j^k.

(4) If the local minimum has a large reduction from the previous image, then the point is determined as the rivulet and the row number is the position of the

rivulet.

(5) Otherwise, the global minimum of A_j^k is determined as the rivulet.

(6) Let $j=j+1$ until all columns are identified. The rivulet location at j-column of the k-th image is denoted as $RL(k, j)$.

Figure 4-4 shows an example of an identified rivulet location in one column. The global minimum of A_j^k is determined as the rivulet location, which shows the largest reduction from the previous image (global minimum of ΔA^k) and coincides with one of the local minimums of A_j^k.
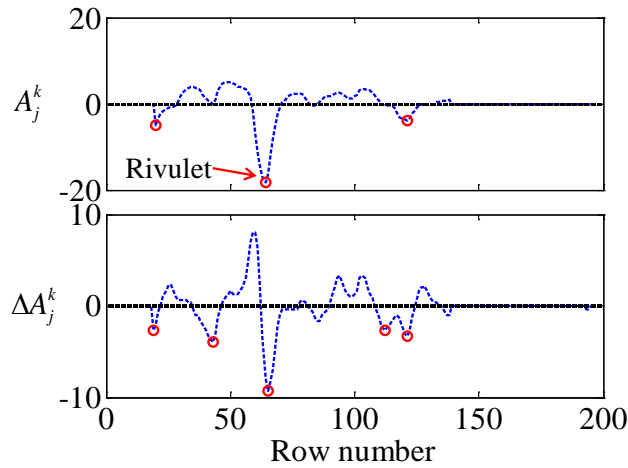
Figure 4-4. An example of rivulet identification

Step 3: Locating rivulets on the cable surface

The rivulet position $RL(k, j)$ obtained in Step 2 is the rivulet position in the image, which is then converted to the physical position on the cable surface. A virtual grid is established in the grayscale image based on the marks on the cable surface as shown in Figure 4-5(a). The distance of the grids on cable surface is 1 cm in the

circumferential direction and 10 cm in longitudinal direction. As the virtual grid is

equivalent to the cable surface in the image, the rivulet position on cable surface is

calculated through linear interpolation of the grids. Consequently, the location of the

rivulet on the cable surface is obtained in terms of the longitudinal distance to the

origin and the circumferential angle θ. As shown in Figure 4-5(b), θ measures

from the top of the cable, and anti-clockwise is positive. In the figure, only the wind

normal to cable axis is illustrated. The angle between the horizontal and wind

direction, φ, is expressed as Equation 4-5 (Wilde and Witkowski 2003) and

calculated as 20.4º.

$$\varphi = \arcsin\left(\frac{\sin\alpha \sin\beta}{\sqrt{\cos^2\beta + \sin^2\alpha \sin^2\beta}}\right) \tag{4-5}$$
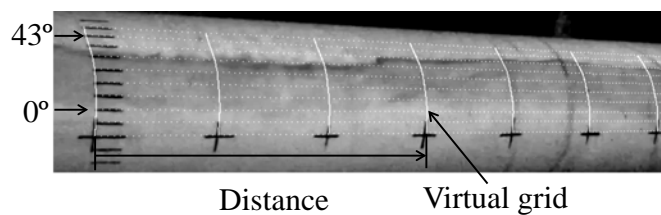
(a) Virtual grid
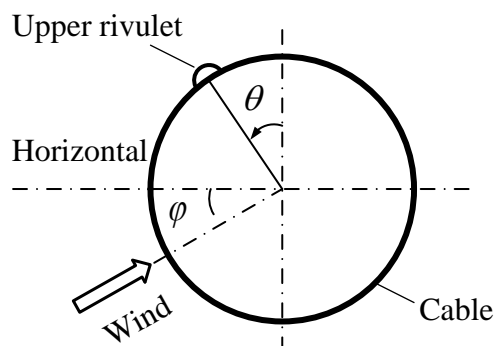
(b) Circumferential position of the upper rivulet

Figure 4-5. Rivulet position on the cable surface

The space resolution of the camera on the cable surface was 1.2 mm/pixel, resulting in an angle resolution in the circumferential direction of 0.8°/pixel.

4.3.2 Rivulet Thickness

The water used to simulate the rivulet was colored by the ink. Since the water is clear and colorless, the color of the rivulet comes from the color particle of the ink, which randomly distributes within the water. Figure 4-6 sketches the cross-section of the colored water and Figure 4-7 shows the ichnography of the colored water at different level of thickness. The color intensity of the colored water in pictures is in direct proportion to the number of the visible color particle within a unit area of ichnography. The relationship between the color intensity and the thickness of the colored water is sketched by the solid line in Figure 4-8. When the colored water is thin, the number of the visible color elements in the ichnography increases with the growth of the water thickness. Therefore, the color intensity increases with the growth of water thickness. When the water thickness keeps growing, the increase of the colour intensity regularly slows down because of the overlap of the color particle in the ichnography. At last, after the ichnography is full with visible color elements, the color intensity becomes constant with the growth of the water thickness.
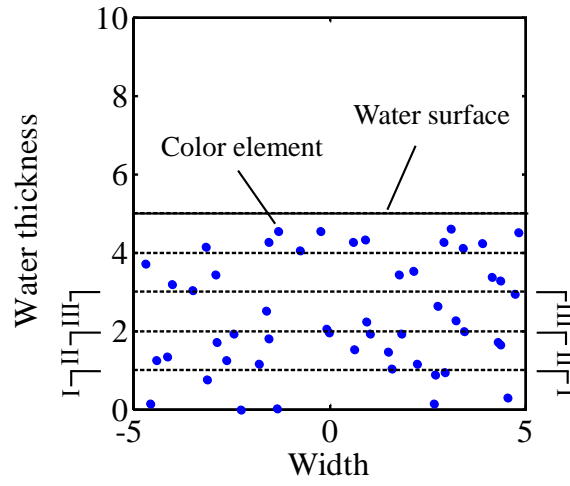
Figure 4-6. Sketch of the cross-section of the coloured water

(a) I－I

(b) II－II

(c) III－III
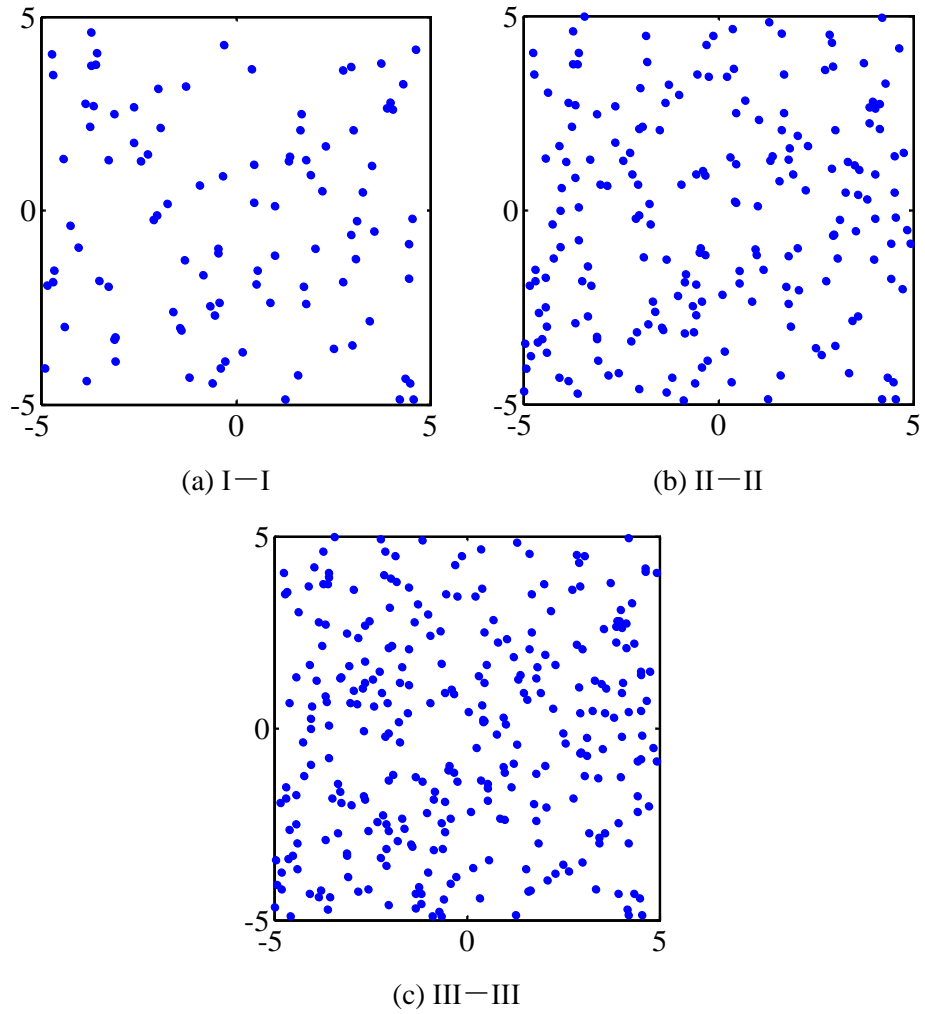
Figure 4-7. Ichnography of Figure 4-6

In this thesis, the ink was diluted five hundred times and the rivulet thickness is very thin. Therefore, it is reasonable to assume that the color intensity of the water rivulet is proportional to its thickness.

Consequently, the water thickness is measured by its relationship with the relative intensity of the pixel, which indicates the colour intensity, as the following equation

$$T_r = C_T \times H \tag{4-6}$$

where T_r denotes the water thickness; C_T is the scale factor; and H is the absolute value of the relative intensity of the pixel, which can be obtained from Section 4.3.1. When $H = 0$, the pixel has the same intensity as the background, indicating no rivulet. C_T is obtained by scaling the intensity such that the cross-sectional area of the measured rivulet (S_m) equals to that of the real rivulet section (S), which is obtained from the water flow of the plastic pipe. That is

$$S = C_T \times S_m \tag{4-7}$$

Figure 4-8 shows the example of the calculation of C_T. The rivulet has been identified at point M with the absolute value of relative intensity $H = 15$. S_m is the area surrounded by curve EMF, which is calculated as 80.72 mm. $S = Q/V$, where

Q is the quantity of the rivulet flow in the plastic pipe which has been measured as 7.46×10^{-7} m^3/s, and V is the flow speed of the rivulet on the inclined cable which is measured as 0.128 m/s. Therefore, S is calculated as 5.84 mm^2, C_T = 5.84/80.72 = 7.23×10^{-2} mm.
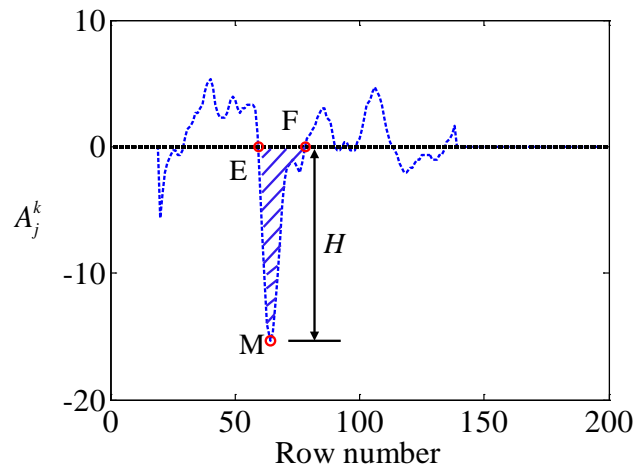
Figure 4-8. Rivulet thickness measurement

4.3.3 Identification of Cable Displacement in Video

Figure 4-9 shows the measurement of the cable displacement using a digital camera. As described in Chapter Three, the target and the ruler were fixed on the steel frame parallel to the cable vibration direction and remained stationary during the RWIV. The digital camera was fixed on the cable model and moved with the cable vibration. The camera displacement was actually the cable displacement. Since the direction of the cable vibration was parallel to the ruler, the movement of the camera was also parallel to the ruler. When the cable and the camera vibrate at a displacement of Δy, the target moves Δp in the image. The resolution of this method is calculated by $\Delta y / \Delta p$.
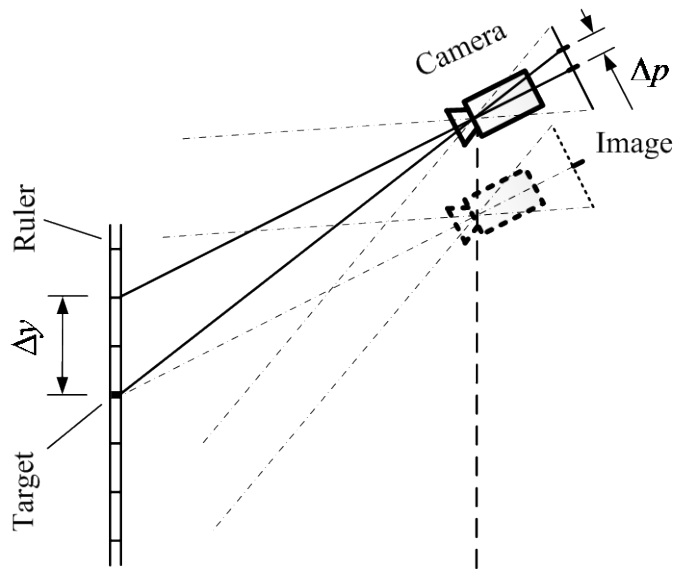
Figure 4-9. Identification of the cable displacement

The cable displacement is identified using the following steps:

(1) Transfer the video clip into a series of still images.

(2) Identify the location of the target and the ruler in the image when the cable is static. This image is referred to as the 'reference image' [see Figure 4-10(a)].

(3) Identify the location of the cross-shaped target in the image when the cable vibrates (Zhou et al. 2012).

(4) Transfer the location of the target in each image into in the physical location. The target's position in k-th image is compared with the reference image and their difference denotes the cable displacement. As shown in Figures 4-10(b) and (c), $\mathbf{y}_k$ and $\mathbf{y}_{k+1}$ represent displacement of the cable at k-th and $(k+1)$-th instant, respectively.

The scale of the reference rule has been calibrated before the tests. The resolution of this method was calculated as 2.5 mm/pixel. The downward movement was set as positive for the cable displacement.

(a) Reference image   (b) Image k   (c) Image k+1
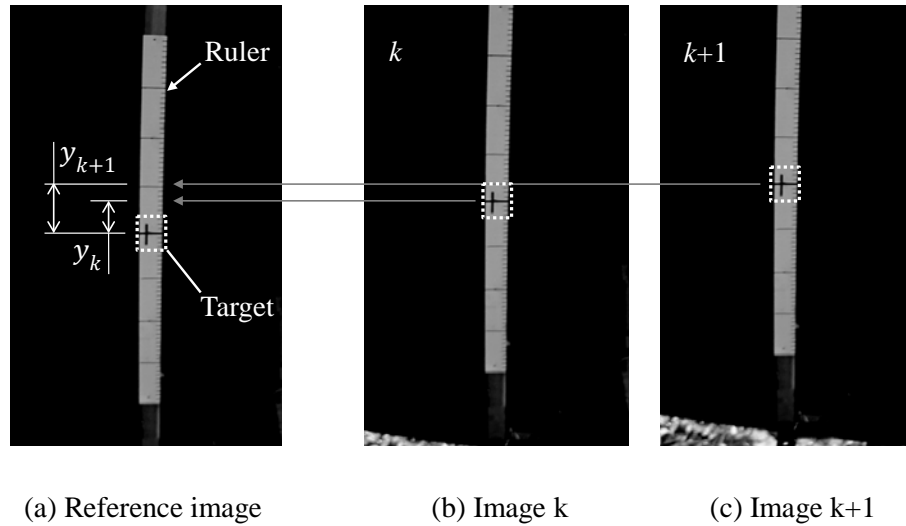
Figure 4-10. Identification of the cable displacement

4.4 Characteristics of the Rivulets Oscillation

Large RWIV of the cable was reproduced in this open-jet wind tunnel under the wind speed U = 12.1 m/s. The cable displacement and upper rivulet movement are identified from the same video clip using the image processing methods described in Sections 4.3.1 and 4.3.3. Figure 4-11 shows the time history and power spectral density (PSD) of the cable displacement. The cable steadily vibrates at the fundamental frequency of 1.37 Hz with the amplitude of 66.3 mm.

(a) Time history

1.37 Hz
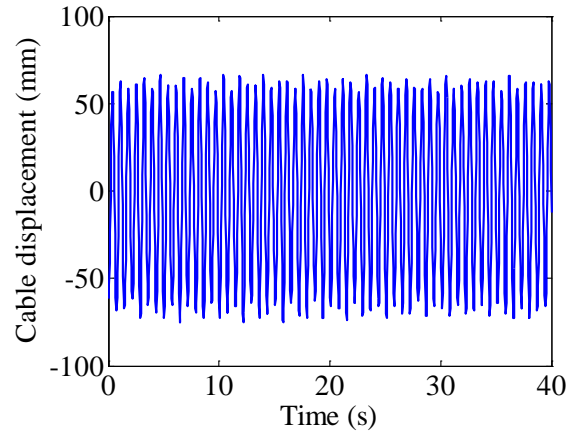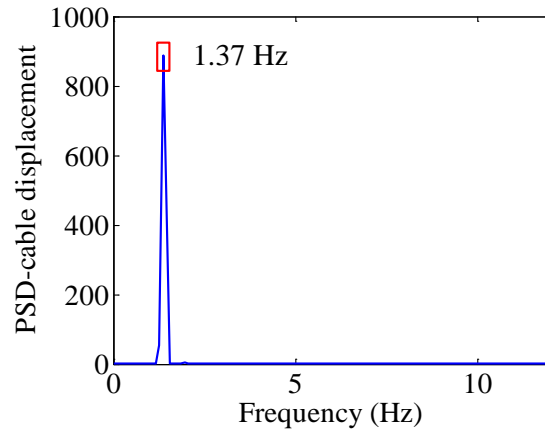
(b) PSD

Figure 4-11. Time history and PSD of the cable displacement

In the case, the time-dependent spatial distribution of the upper rivulet position (θ) along the cable is shown in Figure 4-12. The upper rivulet at individual section of the cable periodically oscillated in the circumferential direction. The oscillation feature at different sections along the cable axis was similar but not exactly the same. Particularly, the oscillation amplitudes are different along the cable axis. Figure 4-13 shows an example of the upper rivulet distribution at 15.44 s. The maximum

difference between different sections at this instant could be as large as 12°. In this regard, the upper rivulet's circumferential position at different cable sections is averaged at each time instant.
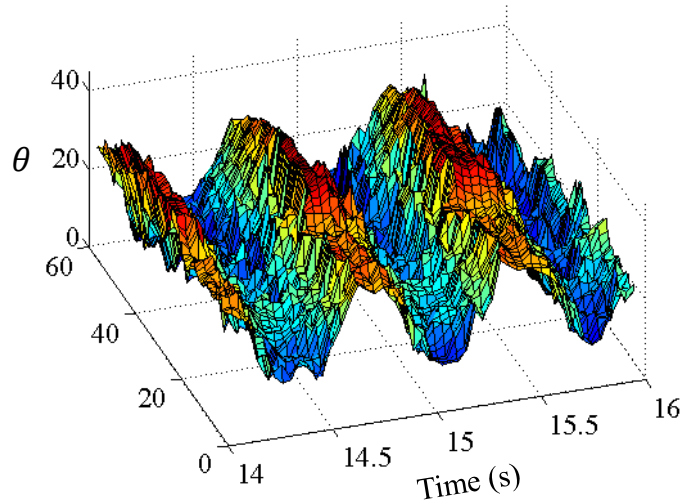
Figure 4-12. Upper rivulet vibration on the cable surface
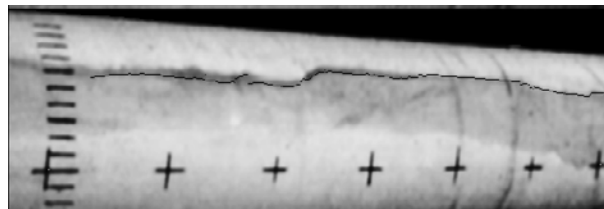
(a)
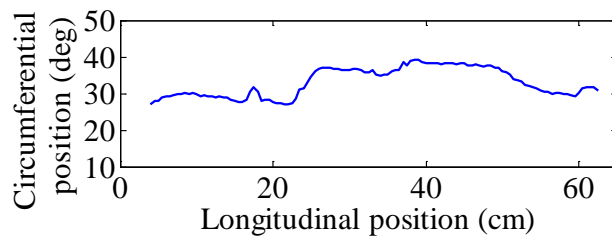
(b)

Figure 4-13. Identified upper rivulet position along the cable at 15.44 s

Figures 4-14(a) and (b) show the time history and the corresponding PSD of the averaged upper rivulet movement. The averaged upper rivulet regularly oscillated between 8º and 34º with the neutral position at 21º. The dominant frequency is 1.37 Hz, same as the cable's vibration frequency. These results coincide with previous studies by Li et al. (2010a) and Cosentino et al. (2003a). Figure 4-14(c) compares the averaged upper rivulet movement and the cable vibration. Both oscillations are steady, regular and almost in-phase, similar to those obtained by Cosentino et al. (2003a). Besides, the averaged upper rivulet oscillated away from the cable top (from 8º to 34º) when the cable moved downward (from –64 to 68 mm). On the contrary, it oscillated towards the cable top (from 34º to 8º) when the cable moved upward (from 68 to –64 mm).
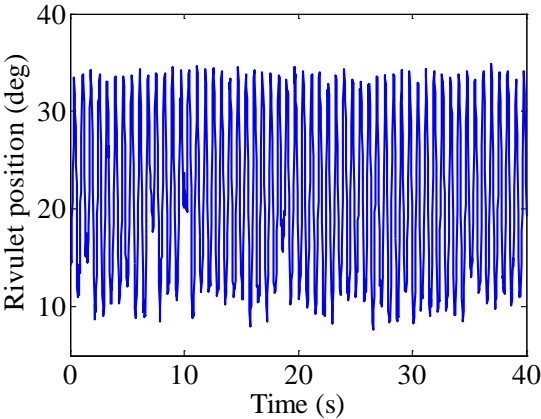
(a) Time history of the upper rivulet position
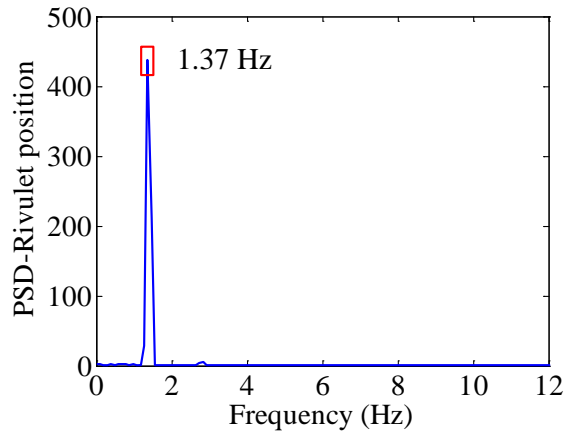
(b) PSD of the upper rivulet position
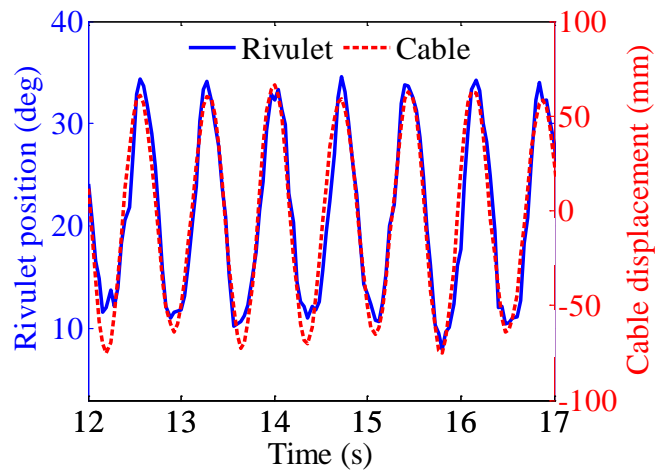
(c) Comparision of the upper rivulet and the cable oscillation

Figure 4-14. Upper rivulet position and the cable displacement when $U = 12.1$ m/s

Similar results have been observed under the wind speed of $U = 14.1$ m/s. The cable vibrated at the fundamental frequency with the amplitude of 40.2 mm. The upper rivulet steadily, regularly and circumferentially oscillated on the cable surface. The oscillation feature is similar but not perfectly uniform along the cable axis. The averaged upper rivulet oscillated between 7° and 35° with the neutral position of 21° at the cable's fundamental frequency. The averaged upper rivulet movement and the cable oscillation were almost in-phase as well.

4.5 Thickness of the Upper Rivulet during Oscillating

The rivulet thickness along the entire cable is also identified from the video clip, as described in Section 4.3.2. Figure 4-15 shows the identified upper rivulet thickness distribution at 15.44 s and 15.84 s, when the cable was at the lowest and highest position, respectively. The thickness varies along the cable. And it was thicker at 15.44 s than at 15.84 s. The thickness is then averaged along the cable axis. Figure 4-16 shows the time history and PSD of the averaged upper rivulet thickness. The upper rivulet thickness varied between 0.17 mm and 1.15 mm when the upper rivulet moved on the cable surface. The mean upper rivulet thickness is calculated as 0.45 mm. Similar results were also observed in previous wind tunnel tests. For example, Cosentino et al. (2003a) observed the upper rivulet thickness varied between 0.15 mm and 0.6 mm in wind tunnel tests. Taylor and Robertson (2015) simulated that the upper rivulet varied between 0.25 mm to 0.35 mm through the computational fluid dynamics when the cable was static. Li et al. (2010a) measured the rivulet thickness at certain section as 0.51 mm, very close to the present mean rivulet thickness. Two dominant frequencies are observed as 1.37 Hz and 2.83 Hz in the PSD. The first dominant frequency coincides with the cable fundamental frequency and the second is roughly double the first with smaller PSD amplitude.
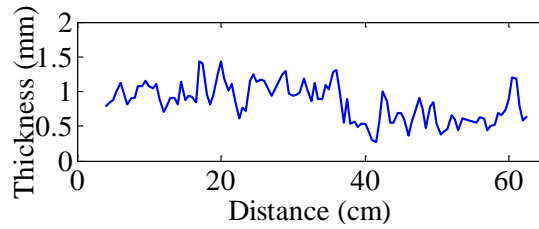
(a) 15.44s
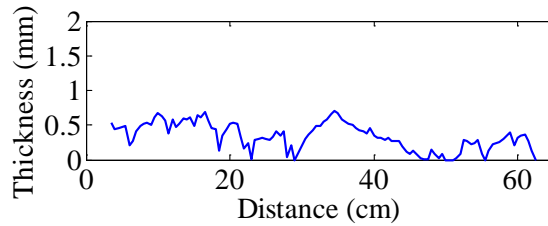
(b) 15.84s

Figure 4-15. Rivulet thickness along the cable

The detailed time history of the averaged upper rivulet thickness is shown in Figure 4-17. The upper rivulet thickness periodically and alternately changes. Within one period, the duration of the thick upper rivulet is about half of those of thin rivulet. The rivulet became thick when it moved away from the cable top (10° to 34°), and reached the thickest at the farthest position away from the top (around 34°). On the contrary, it became thin when it moved back close to the cable top. The thin upper rivulet lasted longer duration. This character is confirmed by the locus in Figure 4-17(b). Combining the obtained relationship between the upper rivulet oscillation and the cable vibration, it reveals that the upper rivulet became thick when the cable reached the lowest position, while became thin when the cable moved back to the highest position.
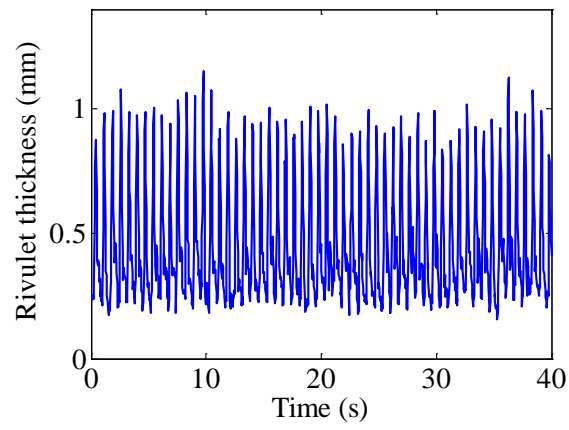
(a) Time history
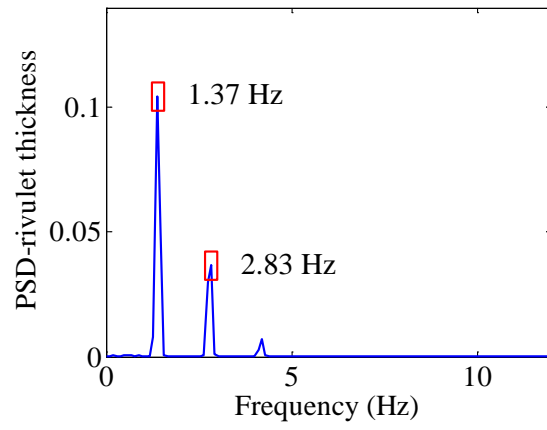
(b) PSD

Figure 4-16. Time history and PSD of the upper rivulet thickness when $U = 12.1$ m/s
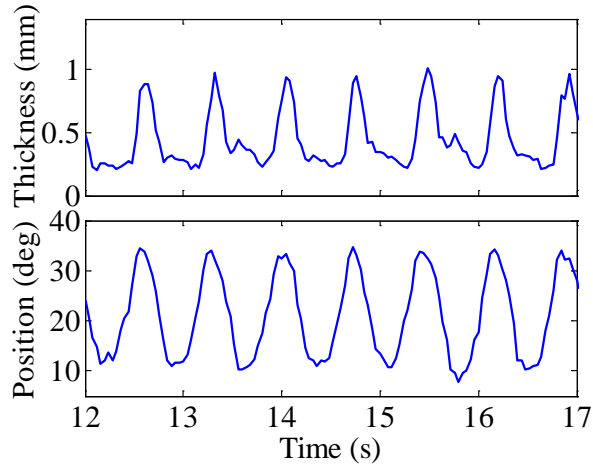
(a) Time histoy
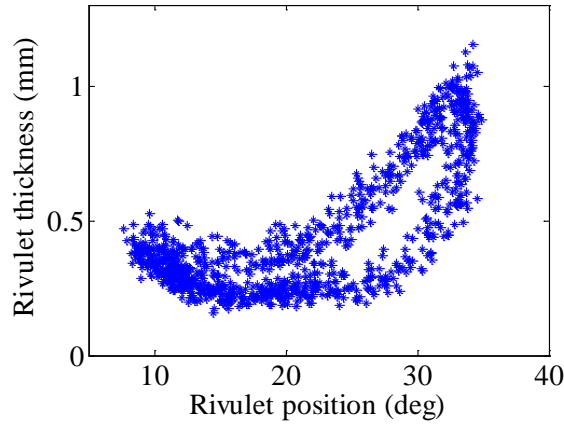
(b) Locus

Figure 4-17. Comparision of thickness and position of upper rivulet ($U = 12.1$ m/s)

Similar results were observed at the wind speed of $U = 14.1$ m/s. The time history
and PSD of the averaged upper rivulet thickness of the case are shown in Figure 4-18.
The upper rivulet thickness varied between 0.05 mm and 1.08 mm with the average
of 0.38 mm. Similar to the case of $U = 12.1$ m/s, the rivulet thickness periodically
varied at the dominate frequencies of 1.37 Hz and 2.83 Hz. Besides, within a single
period, the duration of the thick rivulet was shorter than that of the thin rivulet too.

The upper rivulet became thicker when it moved away from the cable top and the cable vibrated to the lowest position, while became thinner when the upper rivulet and the cable oscillated in the opposite direction.

The difference of the two cases is that the upper rivulet under $U = 14.1$ m/s was slightly thinner than that under $U = 12.1$ m/s and the former varied less regularly and steadily than the latter. The difference might be caused by the different cable vibration amplitude and wind speed. As reported in previous studies (Cosentino et al. 2003a), the variation of the upper rivulet position and thickness are related to the wind speed and the cable vibration. The upper rivulet has been reported being located close to the separation point of the inclined cable. The flow separation point and state of the inclined cylinder change with Reynolds number. Therefore, R_e and the corresponding wind speed should significantly affect the thickness and movement of the upper rivulet. Besides, the initial force from the cable vibration is one of main excitations of the upper rivulet. The cable vibration should also affect the upper rivulet's movement and thickness.
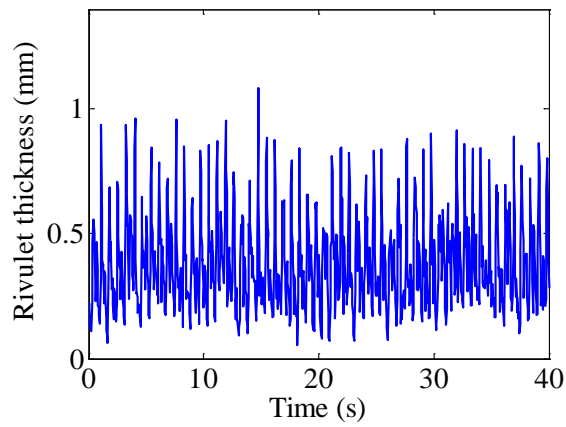
(a) Time history
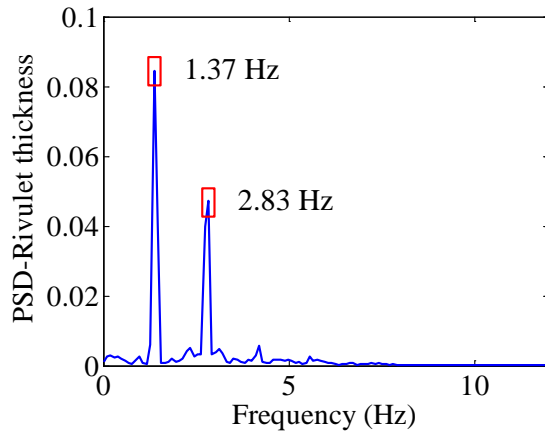
(b) PSD

Figure 4-18. Time history and PSD of the upper rivulet thickness when $U = 14.1$ m/s

4.6 Summary

In this study, large amplitude RWIV of a cable model was reproduced in an open-jet wind tunnel. The cable displacement, the upper rivulet position and thickness were simultaneously measured using the image processing method. The characteristics of the upper rivulet movement and thickness were obtained along the entire cable. Both the position and thickness of the upper rivulet varied with the cable vibration. The

relationships between the upper rivulet oscillation and thickness and the cable vibration have been obtained. Following conclusions can be drawn from the experiment:

(1) The proposed non-contact image processing method is efficient and cost-effective to measure the rivulet position and thickness along the whole cable.

(2) The upper rivulet oscillated circumferentially on the cable surface at the same frequency of the cable's when large RWIV of the cable occurred. The oscillation features of different sections along the cable axis were similar.

(3) The averaged upper rivulet position oscillated almost in-phase with the cable vibration when large RWIV occurred.

(4) The thickness of the upper rivulet periodically varied when the rivulet oscillated on the cable surface. The upper rivulet became thickest when it reached the farthest position away from the cable top and the cable simultaneously arrived at the lowest position.

CHAPTER FIVE

INTERACTION BETWEEN THE UPPER RIVULET AND

CABLE VIBRATION IN WIND TUNNEL TESTS

5.1 Introduction

Extensive research has been conducted to investigate the RWIV through wind tunnel testing (Hikami and Shiraishi 1988; Matsumoto et al. 1992, 1995, 2003b, 2005; Gu and Du 2005; Xu et al. 2006; Du et al. 2013). The on-set conditions of the RWIV, such as the wind speed and direction and rainfall intensity, have been well investigated. The characteristics of the RWIV, including large and restricted amplitude and low dominant frequency, have been reported. Numerous researchers believe that the upper rivulet is the most important factor in the RWIV, and various studies have been conducted try to reveal the relationship between the rivulets and RWIV.

However, up to now, the quantitative and scientific measurement of the rivulet in the RWIV is limited because the rivulet is extremely small, thin, sensitive to wind flow, and uncontrollable (Cosentino et al. 2003a; Li et al. 2010a), therefore directly measuring the rivulets simulated by the real water is very difficult on site or in wind tunnels. In particular, few wind tunnel tests have been carried out to the relationship between the upper rivulet and cable vibration using the real water rivulets.

In Chapter Four, a digital image processing method has been proposed to measure the rivulets' movement and thickness, which makes it possible to quantitatively and scientifically investigate the relationship between the upper rivulet and cable vibration. In this chapter, a stay cable with the rivulets simulated by the real water is tested in a wind tunnel. A digital video camera was installed to record the rivulet movement during the test. The digital image processing method proposed in Chapter Four was adopted to extract the time history of the rivulet movement and the cable displacement. The characteristics of the rivulet oscillation and the relationship between the cable and rivulet vibration are extensively analyzed to assist in understanding the mechanism of the RWIV. The results show that the rivulet–cable system is coupled, which makes the cable steady vibrate with different amplitudes under the same wind speed.

5.2 Wind Tunnel Test

Wind tunnel tests were conducted using the same cable model in the same wind tunnel as described in the previous chapters. However, the fundamental frequency and the structural damping ratio were slightly different. In the present tests, the natural frequency and damping ratio were measured as 1.27 Hz and 0.24% in the vertical direction, respectively, resulting in the Scruton number $S_c = 30.1$. In the horizontal direction, the natural frequency and damping ratio were measured as 1.18 Hz and 0.13% respectively, resulting in the Scruton number of 16.33.

The cable displacement was measured by the digital video camera and two laser distance sensors. They were synchronized by comparing the measured cross-wind displacement of the cable using the two facilities. The cable horizontal vibration was

very small, therefore, only the cross-wind vibration is presented in this chapter and downward movement is set as positive.

The RWIV of the cable model was repeatedly reproduced under the same 'rain' and wind conditions and the results show that the cable could vibrate steadily with different amplitudes. The movement of the upper rivulet was recorded when the cable was static and vibrated with different amplitudes. Then it was identified through the proposed digital image processing method. The details of this method please refer to the Chapter Four.

5.3 RWIVs of Cable Model and the Upper Rivulet Movement

In this Chapter, the cable was observed to vibrate steadily with different amplitudes, such as 50.0 mm, 43.3 mm, 33.3 mm, 29.8 mm, 25.0 mm, 19.6 mm, and relative small vibration with a standard deviation of 4.2 mm, under the same rivulet water flow and wind speed ($Q = 0.7463$ mL/s; $U = 11.4$ m/s). The time history of the cable displacement and the upper rivulet's motion of several typical cases are presented as follows and others exhibit similar characteristics. The lower rivulet is not present in this chapter because it was always static and had no effect on the RWIV.

5.3.1 Upper Rivulet Movement of Vibrating Cable

Figure 5-1 shows the time history and power spectral density (PSD) of the cable vibration when the amplitude Y was 50.0 mm ($Y = 50.0$ mm). The figure shows that cable vibrated steadily at the frequency of 1.27 Hz, same as its natural frequency. Figure 5-2 shows the spatial distribution of the upper rivulet position (θ) along the longitudinal direction, where "Distance" denotes the longitudinal distance of the

rivulet from the reference section [Figure 4-5(a)], and θ is the circumferential position on the cable surface [Figure 4-5(b)]. The upper rivulet periodically oscillated on the cable surface, and the vibrations at different distances were almost in-phase with similar amplitude. The upper rivulet position along the cable axis was then averaged. The time history and PSD of the averaged position are shown in Figure 5-3. The averaged value oscillated between 18° and 36° at the fundamental frequency of 1.27 Hz. Figure 5-4(a) shows a comparison of the upper rivulet movement and the cable vibration. In the figure, both the cable and the upper rivulet oscillated steadily and regularly and were very close to each other, as reported in Cosentino et al. (2003a). The rivulet oscillated away from the cable top to 36° when the cable moved downward (from −50 mm to 50 mm). By contrast, the rivulet oscillated to the cable top (18°) when the cable moved upward (from 50 mm to −50 mm). The cable vibration had a phase delay of about 0.07 π (12.2°) relative to the rivulet oscillation. This phase difference was demonstrated by the elliptical locus in Figure 5-4(b), which moved clockwise. The loci of the different oscillation cycles were very close to one another, which demonstrated the stability and regularity of the rivulet oscillation.
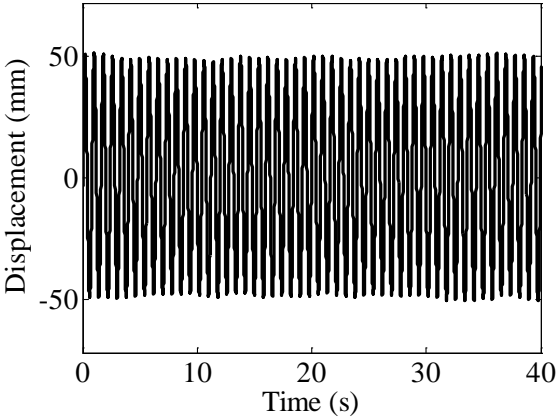
(a) Time history
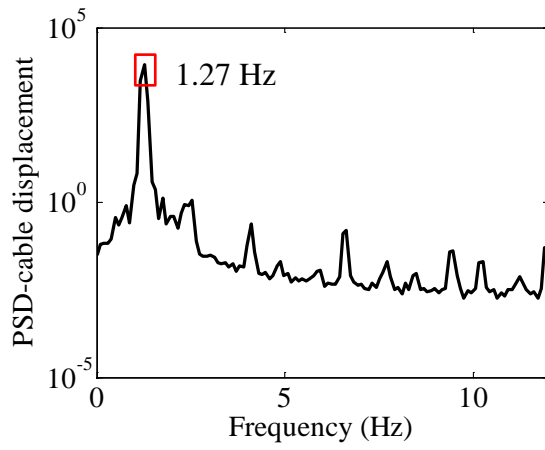
(b) PSD

Figure 5-1. Cable displacement of the RWIV (Y = 50.0 mm)
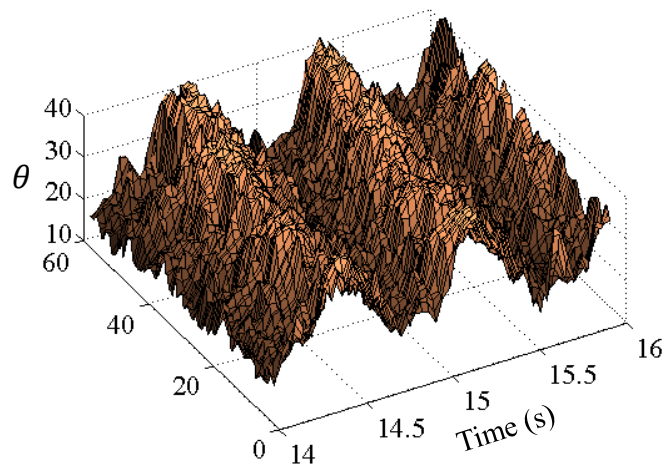
Figure 5-2. Time-dependent spatial distribution of the upper rivulet (Y = 50.0 mm)
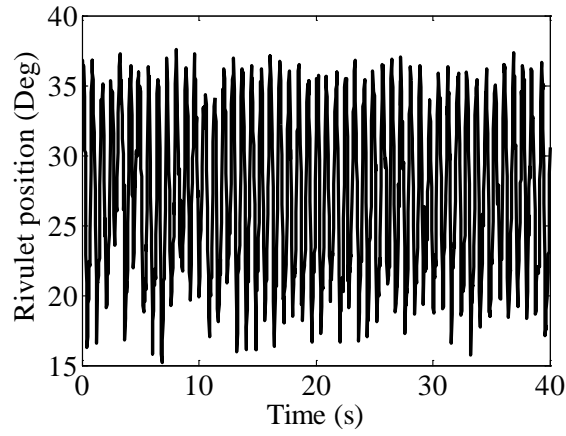
(a) Time history
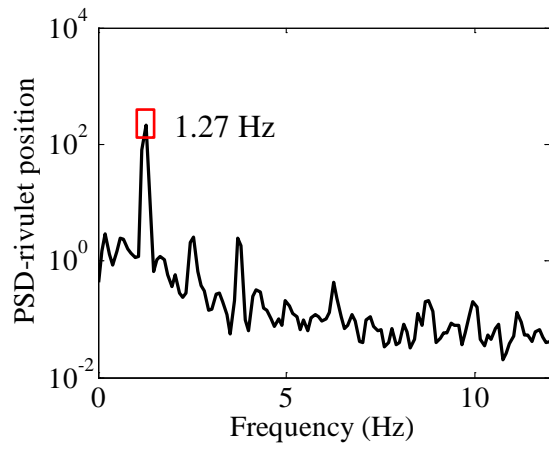
(b) PSD

Figure 5-3. Averaged upper rivulet movement (Y = 50.0 mm)
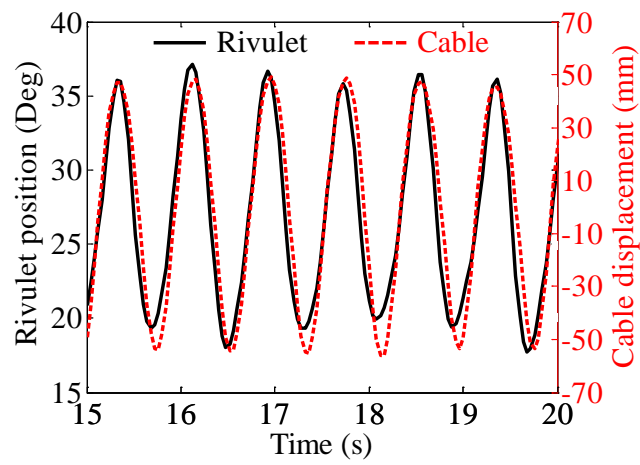
(a) Time history
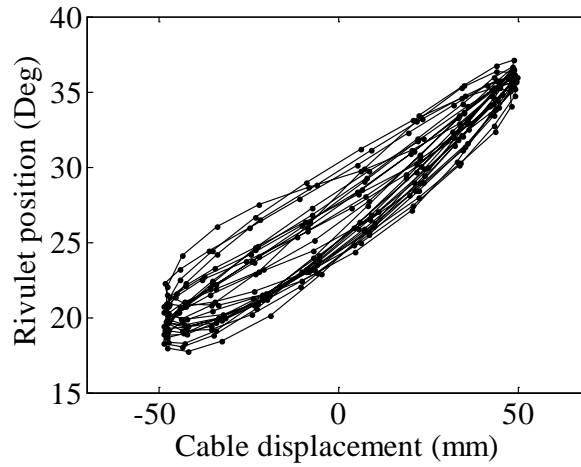
(b) Vibration locus

Figure 5-4. Comparison of the upper rivulet oscillation and cable vibration

($Y = 50.0$ mm)

Figure 5-5 illustrates the spatial distribution of the upper rivulet when the cable vibration reduced to $Y = 33.3$ mm. Similar to the case of $Y = 50.0$ mm, the upper rivulet periodically oscillated on the cable surface. Figures 5-6(a) and (b) show the time history of the cable displacement and the averaged upper rivulet position, respectively. The cable steadily vibrated with 33.3 mm amplitude, and the averaged upper rivulet oscillated between 19° and 38°. The crest of the upper rivulet position was almost stable (around 37°), but the trough varied between 19° and 28°. This observation indicated that the upper rivulet oscillated more steadily at the position away from the cable top than as it moved close to the cable top. Figure 5-6(c) shows the PSD of the averaged upper rivulet position and again the dominant frequency is 1.27 Hz. The upper rivulet oscillation and the cable vibration are compared in Figure 5-6(d). The phase difference of the upper rivulet oscillation and the cable vibration was calculated as 0.24π (42.3°).
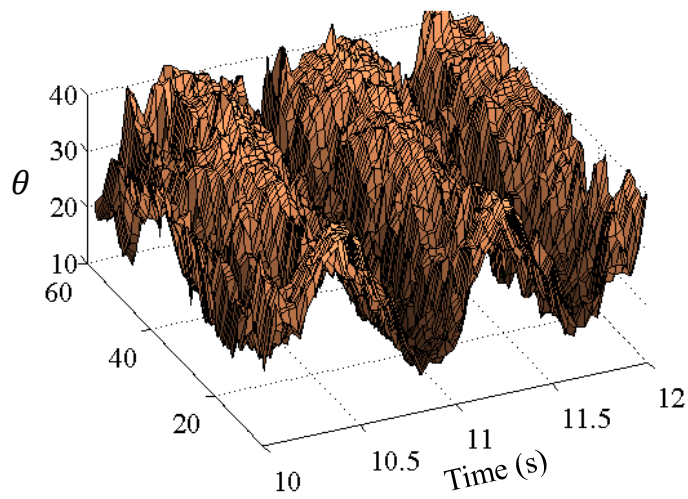
Figure 5-5. Time-dependent spatial distribution of the upper rivulet ($Y = 33.3$ mm)
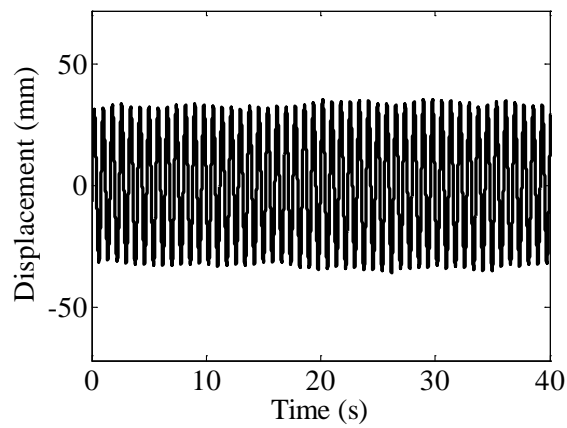
(a) Time history of cable displacement
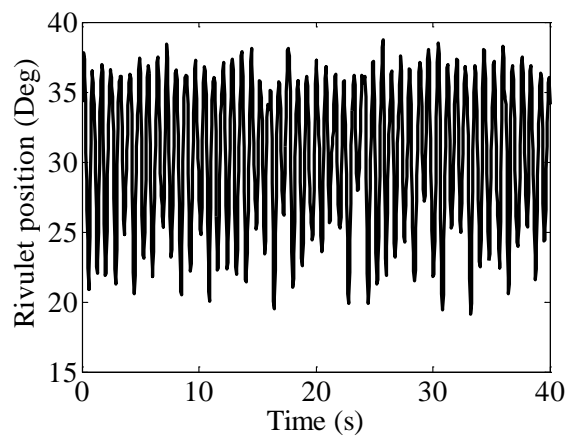
(b) Time history of upper rivulet position
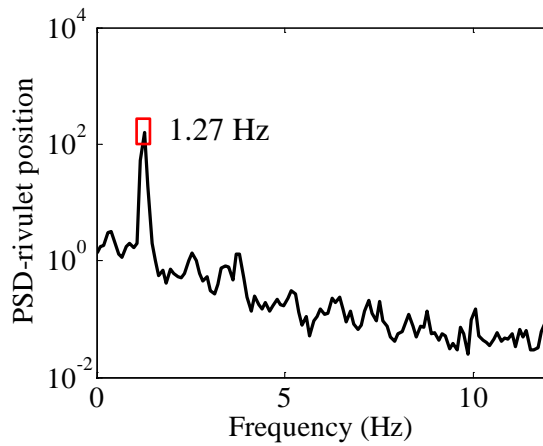
(c) PSD of upper rivulet position
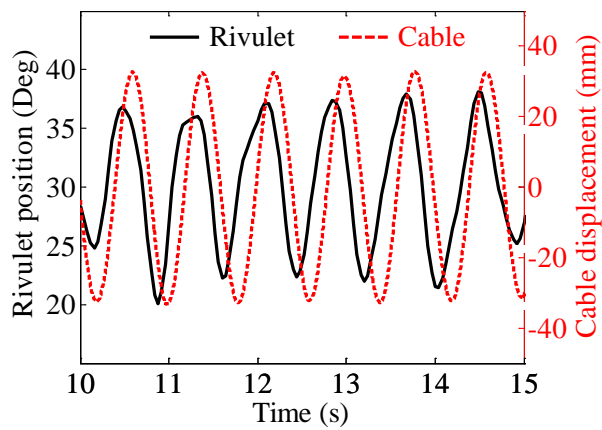
(d) Comparison of time history

Figure 5-6. Cable vibration and upper rivulet oscillation ($Y = 33.3$ mm)

Figure 5-7 shows the time-dependent spatial distribution of the upper rivulet when the cable vibration weakened further to $Y = 19.6$ mm. The periodicity of the upper rivulet oscillation was not as stable as the cases when large RWIV occurred. The spatial distribution of the rivulet position along the cable was not uniform either. Figures 5-8(a) and (b) show the time history of the cable and the averaged upper rivulet vibrations respectively. The cable steadily vibrated with 19.6 mm amplitude,

and the averaged upper rivulet oscillated between 15° and 37°. The crest of the averaged upper rivulet position was always stable (around 36°), but the trough varied between 15° and 29°. The dominant frequency of the averaged upper rivulet oscillation was 1.27 Hz. The upper rivulet oscillation was obviously less sinusoidal and less steady compared with the cable. The averaged phase difference of the upper rivulet oscillation was calculated as 0.33π (59.8°) compared to the cable vibration.
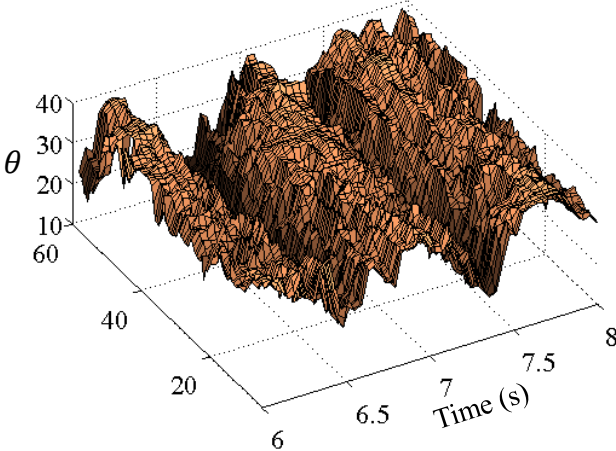
Figure 5-7. Time-dependent spatial distribution of the upper rivulet ($Y = 19.6$ mm)
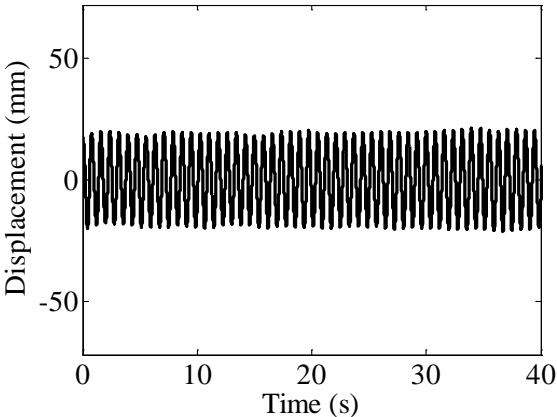
(a) Cable displacement
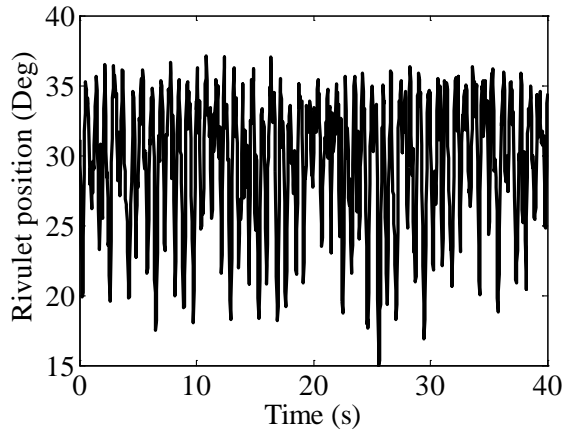
(b) Upper rivulet position
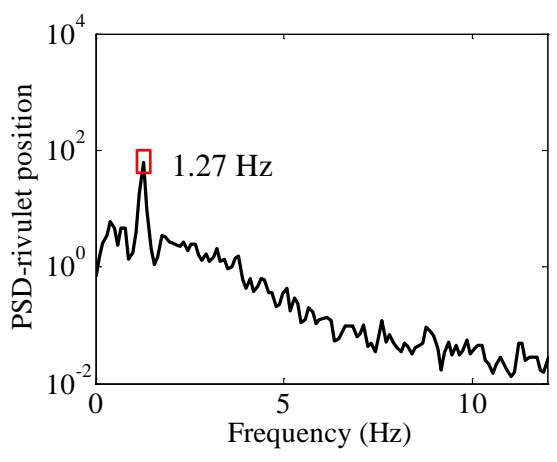
(c) PSD of the averaged upper rivulet
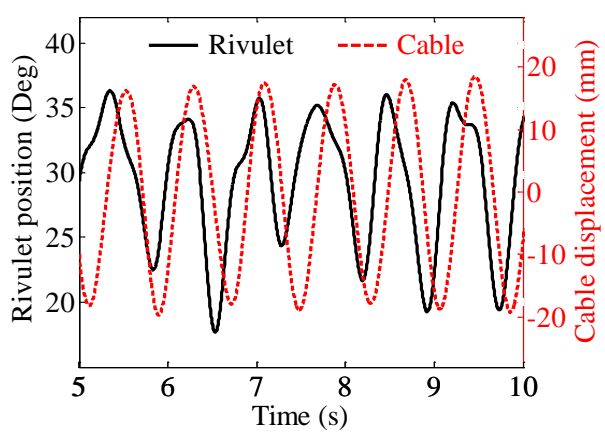
(d) Comparison of time history

Figure 5-8. Cable vibration and upper rivulet oscillation ($Y = 19.6$ mm)

The upper rivulet movement was also measured when the cable vibration was very small. Figure 5-9 shows the spatial distribution of the upper rivulet when the standard deviation of the cable vibration amplitude was 4.2 mm. The distribution along the cable was non-uniform, and the rivulet oscillation was non-harmonic. Figures 5-10(a) and (b) show the time history and PSD of the cable vibration, respectively. The dominant frequency of the cable vibration was 1.27 Hz, while a higher frequency occurred as well. Figures 5-10(c) and (d) show the time history and PSD of the averaged upper rivulet oscillation, respectively. The averaged upper rivulet oscillated unsteadily between 20° and 37°. Although a peak at 1.27 Hz was observed, the upper rivulet exhibited a uniform frequency band between 0 and 5 Hz.
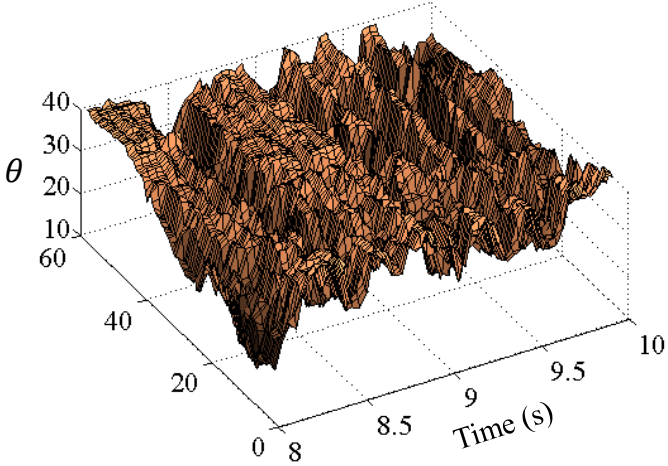
Figure 5-9. Time-dependent spatial distribution of the upper rivulet (Std = 4.2 mm)
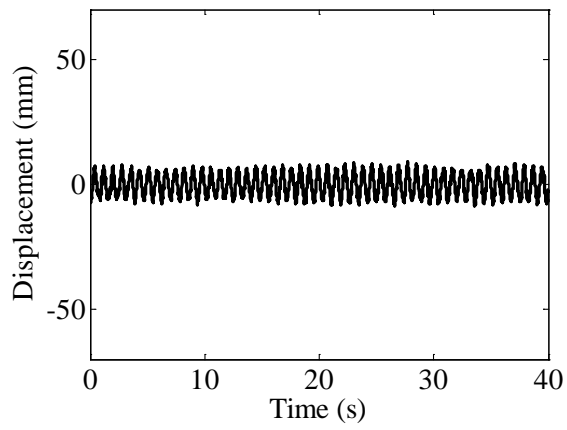
(a) Time history of cable displacement
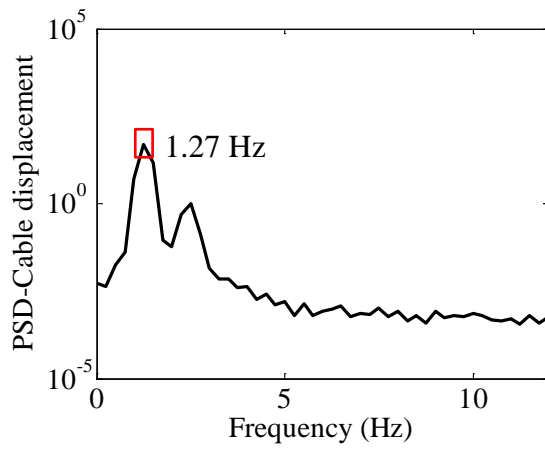
(b) PSD of cable displacement
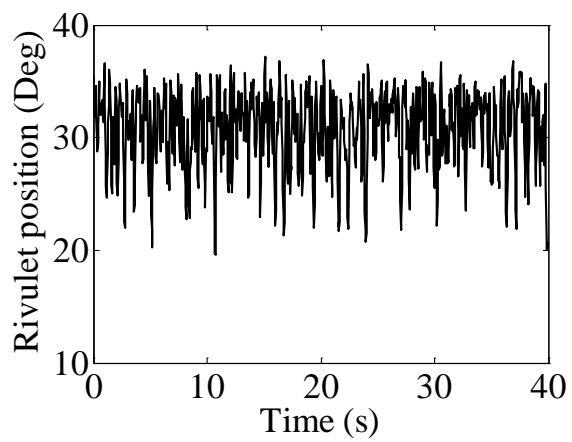
(c) Time history of averaged upper rivulet

107
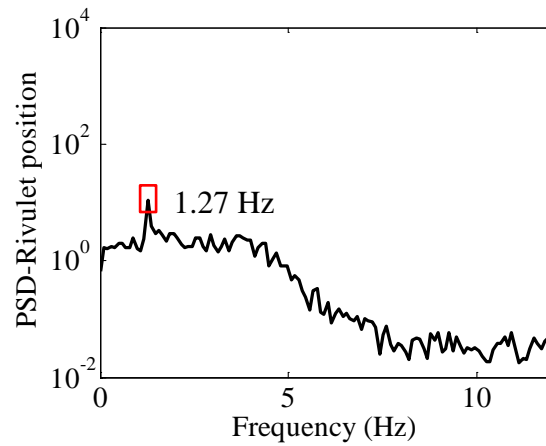
(d) PSD of averaged upper rivulet

Figure 5-10. Cable vibration and upper rivulet oscillation (Std = 4.2 mm)

5.3.2 Rivulet Motion on Stationary Cable

For comparison, the system was also tested by fixing the cable model at both ends under 11.4 m/s wind speed. The time-dependent spatial position of the upper rivulet along the stay cable is shown in Figure 5-11. The upper rivulet could vibrate on the cable surface, but the vibration was not harmonic and the motion along the longitudinal direction was non-uniform. As shown in Figure 5-12, the averaged upper rivulet vibrated between 20° and 33° with the neutral position of 27°, and exhibited a uniform frequency band between 0 and 5 Hz.
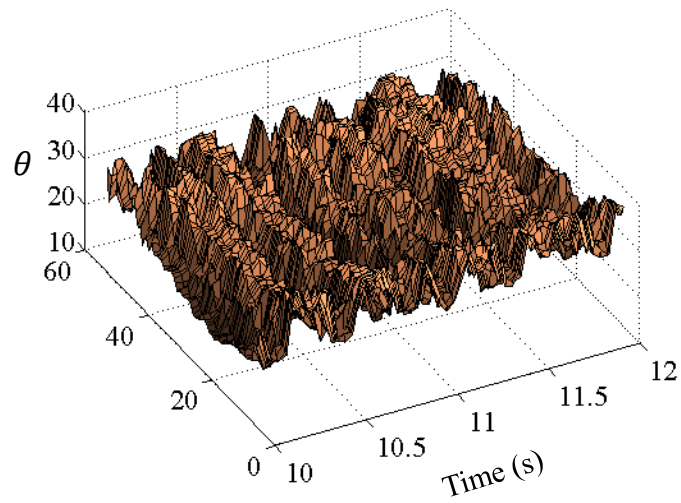
Figure 5-11. Upper rivulet movement when the cable was fixed and the wind speed

was 11.4 m/s
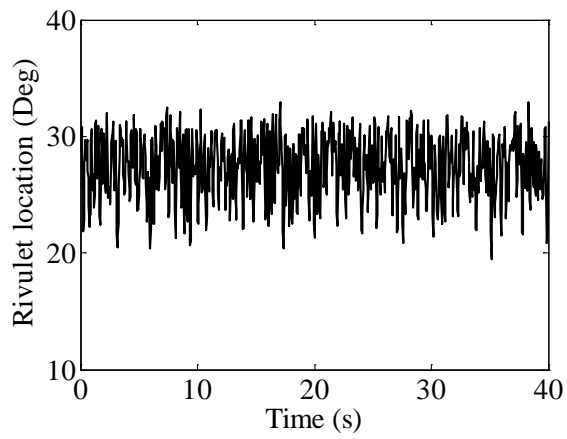
(a) Time history
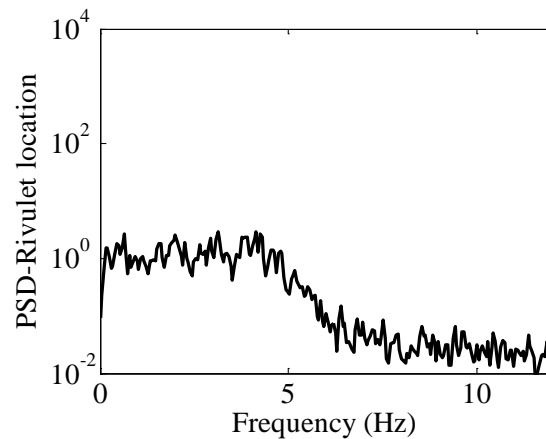
(b) PSD

Figure 5-12. Upper rivulet movement when the cable was fixed

5.4 Discussions

The upper rivulet movement under different cable vibrations was obtained. When the cable was experiencing a large amplitude vibration, the upper rivulet oscillated almost in-phase and uniformly along the cable axis. The averaged upper rivulet harmonically and regularly oscillated on the cable surface with steady amplitude at the cable's fundamental frequency. The phase difference between cable vibration and averaged upper rivulet oscillation was very small. When the amplitude of the cable vibration was smaller, the upper rivulet oscillation became less harmonic and less uniform along the cable axis, particularly at the position close to the cable top. In addition, the phase difference between the cable vibration and the upper rivulet oscillation increased. When the cable was vibrating with very small amplitude, the upper rivulet along the cable axis was non-uniform and the averaged upper rivulet exhibited a small harmonic plus a wideband process. When the cable was fixed without any vibration, the averaged upper rivulet was a pure wideband random process.

The upper rivulet is subjected to gravity, wind pressure, surface tension, friction force, and inertia force caused by cable vibration. Lemaitre et al. (2007, 2010) and Taylor et al. (2011) have pointed out the importance of the wind pressure and shear force in the formation of the rivulets when the cable was static. The above experimental observations show that the cable vibration plays a significant role in harmonizing the upper rivulet movement. The cable vibration generates the harmonic inertia force on the upper rivulet and periodically changes the attacking angle of the wind which also generates periodic aerodynamic forces including the wind pressure and shear force on the upper rivulet. Consequently, when the cable is static, the upper rivulet moves forth and back without a dominant frequency. As the cable starts oscillating, even at small amplitude, the cable vibration is able to drive the upper rivulet oscillating at the cable vibration frequency. When the cable vibration becomes large, the upper rivulet steadily and uniformly oscillates along the cable axis.

On the other hand, the cable is subjected to gravity and wind pressure. The existence of the upper rivulet changes the aerodynamic forces. The time-varying position of the upper rivulet continuously changes the wind force on the cable. When the upper rivulet movement is non-uniform along the cable axis, the generated wind forces along the cable axis are different in phase, and the resultant force on the cable is small. Consequently, the cable presents a small vibration only. When the upper rivulet uniformly and steadily oscillates along the cable axis, the wind forces along the cable axis are uniform and the resultant force increases, exciting the cable vibration with large amplitude.

Therefore, the cable vibration and upper rivulet oscillation interact and excite with

each other. When they reach an equilibrium state, steady RWIV of cable occurs. The multi-amplitude RWIV under the same wind speed observed in this chapter indicates that the equilibrium state might be non-unique. Different amplitude RWIV could be caused by the small difference in initial conditions. The initial conditions of the upper rivulet and the cable vibration significantly affect the amplitude of the RWIV. If the upper rivulet oscillation is uniform along the cable axis at the beginning even with small amplitude, the cable could grow into large amplitude RWIV, and vice versa.

5.5 Summary

In this chapter, the RWIV of the cable model were repeatedly reproduced in the wind tunnel. The cable was observed to vibrate steadily with different amplitudes under the same rivulet flow rate and wind speed. The characteristics of the rivulet movement were investigated under different cable vibrations. The relationship between the upper rivulet and cable vibrations was obtained. The main conclusions can be drawn as follows:

(1) The upper rivulet and the cable vibrations were coupled.

(2) The cable may vibrate with different amplitudes under the same wind speed. When large cable vibration occurs, the upper rivulet periodically oscillates on the cable surface in the circumferential direction and the oscillations are almost in-phase with the same amplitude along the cable axis. The upper rivulet oscillates less harmonically and less uniformly along the cable axis when the cable vibration amplitude is small.

(3) The inertia force and the periodic variation of the attacking angle provided by the vertical cable vibration excite the upper rivulet oscillation. Uniform oscillation of

the upper rivulet generates a significant resultant lift force on the cable and causes it to vibrate at large amplitude. This interaction might be the main mechanism of the RWIV of the cable, which will be studied in Chapter Seven in details.

NUMERICAL ANALYSIS OF RWIV BASED ON QUASI-STEADY ASSUMPTION

6.1 Introduction

The RWIV has been widely reported as a complicated fluid-solid coupled process with nonlinearity and the excitation mechanism of the RWIV has not been fully understood (Robertson et al. 2010, Taylor et al. 2010). Extensive research has been conducted to understand the excitation mechanism of the RWIV through numerical analysis based on the quasi-steady assumptions. Two numerical approaches have been developed to simulate the movement of the upper rivulet on the cable section model: one is to assume that the upper rivulet movement directly depends on the cable vibration (Geurts et al. 1998; Xu and Wang 2003; Wilde and Witkowski 2003; Cao et al. 2003; Li et al. 2015) and the other is to calculate the upper rivulet's response by solving the coupled kinematic equation (Wang and Xu 2003; Cosentino et al. 2003a; Gu 2009). The former is concise and effective. The assumption of the relationship between the upper rivulet and the cable vibration has been experimentally verified in Chapter Four. The latter can explain the detail of the interaction between the upper rivulet and the cable. However, the calibration of the parameters used in the coupled kinematic equation is difficult.

All analytical models consider the upper rivulet as one important factor in the RWIV, but valuable information on the upper rivulet measured in wind tunnel tests is limited and comparisons between the numerical and the experimental results are very few. Most of the numerical models were based on the aerodynamic force coefficient curves measured by Yamaguchi (1990) and Gu et al. (2002). These aerodynamic force coefficients were measured on a two dimensional cable model without considering the effects of yaw angles. However, the RWIV were only observed on the inclined stay cables under the three dimensional ambient wind.

In this chapter, a numerical model based on the first approach is established and the aerodynamic force coefficients measured by Xu et al. (2006) on an inclined yawed cable model are used to calculate the responses of the cable model. By this means, the effect of the three dimensionality of the wind on the aerodynamic force coefficients is considered.

The numerical model is then applied to two cable models. One was tested by Hikami and Shiraishi (1988), which provided the upper rivulet information including the initial position and the vibration amplitude. The second is the cable tested in previous chapters. The responses of the former are calculated using the established numerical model. The effects of different parameters such as the rivulet movement, structural damping ratio, and cable fundamental frequency, are investigated. For the second cable model, the identified parameters of the upper rivulet movement during the wind tunnel test are used in the numerical model. The calculated cable responses are compared with the wind tunnel results.

6.2.1 Wind Speed and Forces on the Two Dimensional Cable Model

An inclined cable subjected to yaw wind flow, as shown in Figure 6-1(a), is considered. The cable model has the inclination angle α and the yaw angle β. Since the sag of real stay-cables is relatively small, the inclined cable is modeled by a rigid and uniform circular cylinder. The upper rivulet is assumed to be rigid in shape and circumferentially vibrate on the cable surface during the RWIV, while the lower rivulet is ignored since it has no effect on the RWIV. The distribution of the upper rivulet is assumed to be uniform along the longitudinal axis of the cable model.

The incoming wind speed is decomposed into two components as Figure 6-1(a) shows: (1) wind speed in the cable plane ($U \sin \beta$); and (2) that normal to the cable plane ($U \cos \beta$). The former one can be future decomposed into the wind speed parallel to the cable axis ($U \sin \beta \cos \alpha$) and that normal to the cable axis ($U \sin \beta \sin \alpha$) as shown in Figure 6-1(b). Consequently, in the cross-section of the cable model, the resultant wind speed normal to the cable axis (U_{N0}) and the attacking angle (φ_0) can be calculated as:

$$U_{N0} = U \sqrt{\cos^2 \beta + \sin^2 \beta \sin^2 \alpha} \qquad (6\text{-}1)$$

$$\varphi_0 = \arcsin(\frac{\sin \alpha \sin \beta}{\sqrt{\cos^2 \beta + \sin^2 \alpha \sin^2 \beta}}) \qquad (6\text{-}2)$$

(a)   (b)   (c)
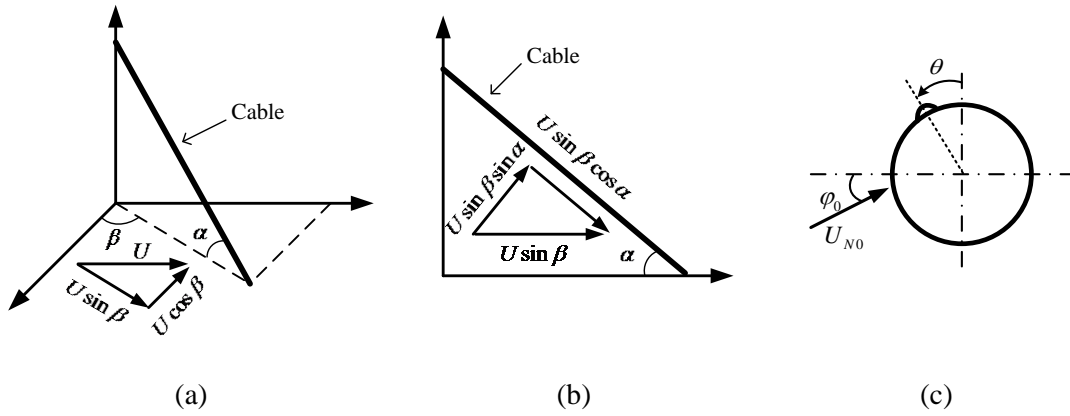
Figure 6-1. Wind speed respect to the cable

When the cable is vibrating in the vertical direction with the velocity of $\dot{y}$ (a downward y is positive) and the upper rivulet is vibrating in anti-clockwise with the angular velocity of $\dot{\theta}$ as shown in Figure 6-2, the relative wind speed and the corresponding attacking angle are modified as:

$$U_N = \sqrt{(U\cos\beta + R\dot{\theta}\cos\theta)^2 + (U\sin\beta\cos\alpha + \dot{y} + R\dot{\theta}\sin\theta)^2} \qquad (6\text{-}3)$$

$$\varphi = \arcsin(\frac{U\sin\beta\cos\alpha + \dot{y} + R\dot{\theta}\sin\theta}{U_N}) \qquad (6\text{-}4)$$

where R denotes the external radius of the cable model.
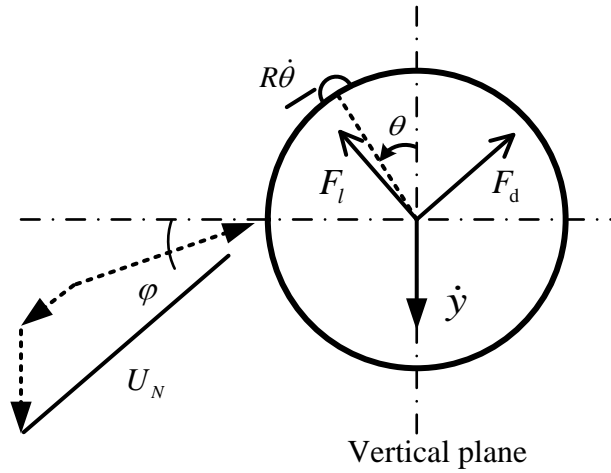
Figure 6-2. Wind speed and forces in the cross-section of the cable

In the two-dimensional cable model, the effect of the longitudinal wind on the wind forces acting on the cable model is ignored based on the quasi-steady assumptions. The aerodynamic forces are only related to the wind speed normal to the cable axis. Therefore, the aerodynamic lift and drag force coefficients (C_l and C_d) of the cable are defined as:

$$C_l = \frac{2F_l}{\rho U_N^2 D} \tag{6-5a}$$

$$C_d = \frac{2F_d}{\rho U_N^2 D} \tag{6-5b}$$

where ρ denotes the air density; D external diameter of the cable model; F_l and F_d are the lift and dry forces of the cable model, respectively, which are measured when the incoming wind was normal to the cable model in a wind tunnel.

The resultant forces in the vertical and horizontal directions are expressed as:

$$F_v = \frac{1}{2}\rho U_N^2 D(C_l \cos\varphi + C_d \sin\varphi) \qquad\qquad (6\text{-}6a)$$

$$F_h = \frac{1}{2}\rho U_N^2 D(C_d \cos\varphi - C_l \sin\varphi) \qquad\qquad (6\text{-}6b)$$

6.2.2 Analysis Model of Three Dimensional Cable Based on Quasi-Steady Assumptions

The aerodynamic force coefficients of the two-dimensional cable model have been widely used in previous numerical analysis (Xu and Wang 2003; Wilde and Witkowshi 2003). However, Xu et al. (2006) and Du et al. (2013) pointed out that the three dimensionality of the wind has significantly effects on the aerodynamic forces of the inclined cable. They both measured the aerodynamic force coefficients on the inclined cable suffering yaw wind.

In this chapter, the force coefficients measured by Xu et al. (2006) are adopted to calculate the responses of the cable. The numerical model of an inclined and yawed cable is established based on the following assumptions (Wilde and Witkowshi 2003; Taylor et al. 2010):

(1) The upper rivulet excites the RWIV, while the lower one has no effect on the RWIV.

(2) The upper rivulet circumferentially vibrates on the cable surface at the cable fundamental frequency during the RWIV.

(3) The amplitude of the upper rivulet vibration is proportional to the cable amplitude for a given wind speed, and the amplitude ratio is constant.

(4) The initial position of the upper rivulet depends on the wind speed. Their relationship is obtained through wind tunnel testing.

(5) The mass of the rivulet is negligible compared with that of the cable.

(6) The upper rivulet changes the loading of the cable by modifying the aerodynamic force coefficients when it moves on the cable surface.

(7) Only the in-plane cable vibration occurs with a relatively small amplitude and the out-of-plane vibration is ignored.

(8) Only the single mode vibration is considered and the interaction between multiple modes is ignored.

Figure 6-3 shows the sketch of the analytical model. The equation of motion of the cable is expressed as:

$$\ddot{y} + 2\xi_s \omega \dot{y} + \omega^2 y = -F_v / m \qquad (6\text{-}7)$$

where m is the mass of the cable model per unit length, $\omega = \sqrt{K/m}$ the circular frequency of the cable model, and $\xi_s = C/2m\omega$ the structural damping ratio. The negative sign in the vertical force of Equation (6-7) is attributed to the fact that the force is opposite to the positive direction.
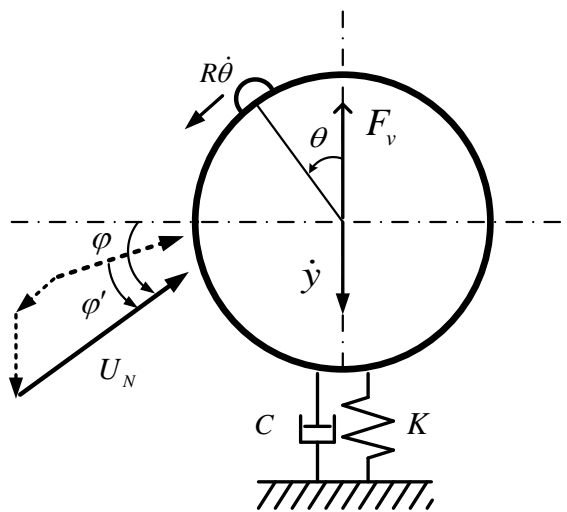
Figure 6-3. The cable model and the upper rivulet

The aerodynamic force coefficients measured by Xu et al. (2006) were based on the body coordinate system of the cable model, as Figure 6-4 shows. The lift force was in the cross-section and in the vertical direction; and the drag force was in the cross-section and in the horizontal direction.
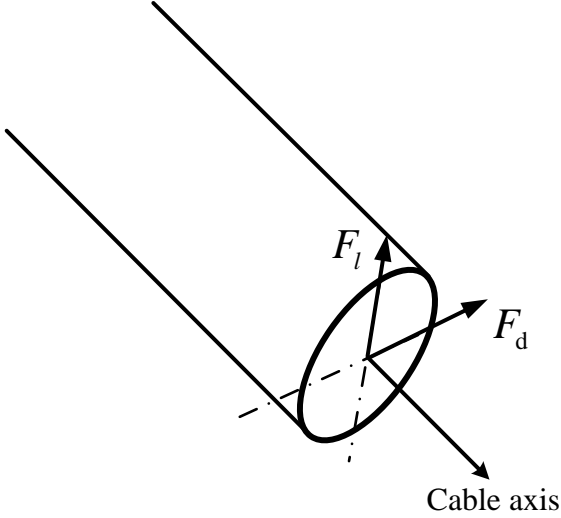
Figure 6-4. Lift and drag forces in the body coordinate

The loading of the cable in Equation (6-7) is modified as:

$$F_v = \frac{1}{2}\rho U_{rel}^2 D[C_l \cos\varphi' + C_d \sin\varphi'] \tag{6-8}$$

where U_{rel} is the resultant wind speed considering the effects of the cable and upper rivulet vibration, and φ' denotes the attacking angle induced by the cable and upper rivulet vibration:

$$U_{rel} = \sqrt{(U\cos\beta + R\dot{\theta}\cos\theta)^2 + (U\sin\beta\sin\alpha + \dot{y} + R\dot{\theta}\sin\theta)^2 + (U\sin\beta\cos\alpha)^2} \tag{6-9}$$

$$\varphi' = \varphi_y + \varphi_\theta \tag{6-10}$$

where φ_y and φ_θ are the attacking angle induced by the cable vibration and the rivulet vibration, respectively.

$$\varphi_y = \arctan\left(\frac{\dot{y}\cos\varphi_0}{U_{N0} + \dot{y}\sin\varphi_0}\right) \tag{6-11}$$

$$\varphi_\theta = \arctan\left[\frac{R\dot{\theta}\cos(\theta - \varphi_0)}{U_{N0} + R\dot{\theta}\sin(\theta - \varphi_0)}\right] \tag{6-12}$$

For an inclined and yawed cable, C_l and C_d of Equation 6-8 are the functions of the inclination angle (α), yaw angle (β), and the relative position of the upper rivulet θ_r, which is defined as the difference between the position of the upper rivulet on the cable and the attacking angle, that is,

$$\theta_r = \theta - \varphi' \tag{6-13}$$

In the equation, the rivulet position θ can be decomposed as two parts: the initial position or neutral position (θ_0) and the dynamic position (θ_v):

$$\theta = \theta_0 + \theta_v \tag{6-14}$$

θ_0 depends on the cable geometry (such as α, β, D) and the wind speed, and θ_v is

assumed to be proportional to the cable vibration, that is,

$$\theta_v = c_\theta y \hspace{4cm} \text{(6-15)}$$

where c_θ is the amplitude ratio between the rivulet and cable vibrations. Both θ_0

and c_θ are usually measured through wind tunnel testing.

Submitting Equations (6-8) to (6-15) into Equation (6-7), the responses of the cable

and the upper rivulet can be calculated by solving the equation using the

Runge-Kutta integration method.

6.2.3 Aerodynamic Coefficients Measured on an Inclined and Yaw Cylinder by Xu et al. (2006)

In this study, three sets of aerodynamic force coefficients measured by Xu et al.

(2006) are adopted to calculate the responses of the cable. They measured these

aerodynamic force coefficients using two types of artificial upper rivulet (Shapes A

and B shown in Figure 6-5) under two sets of inclination and yaw angles. Shape A

was 10 mm in length and 4 mm in height, which was close to that commonly used in

other studies, such as Matsumoto et al. (1992), Gu (2009), and Du et al. (2013).

Shape B was 8 mm in length and 2 mm in height, closer to the upper rivulet

measured in Chapter Four.

Figure 6-6 shows the measured drag and lift coefficients when both inclined and

yawed angles were 45° and the artificial rivulet was Shape A. Figure 6-7 shows the

drag and lift coefficients of the cable with the rivulet having Shapes A and B, in both cases the cable had the inclination angle of 30° and yaw angle of 35°.
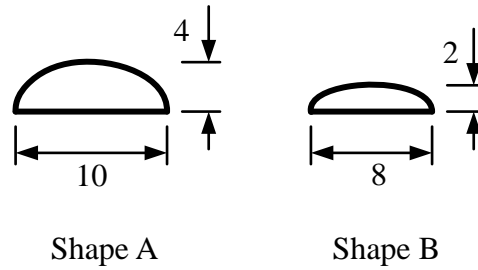
Figure 6-5. Artificial upper rivulets used by Xu et al. (2006) (unit: mm)
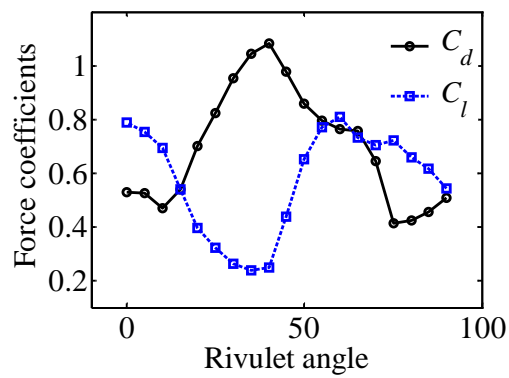
Figure 6-6. Lift and drag coefficients of cable ($\alpha = \beta = 45°$) measured by Xu et al.

(2006)

(a) Shape A   (b) Shape B
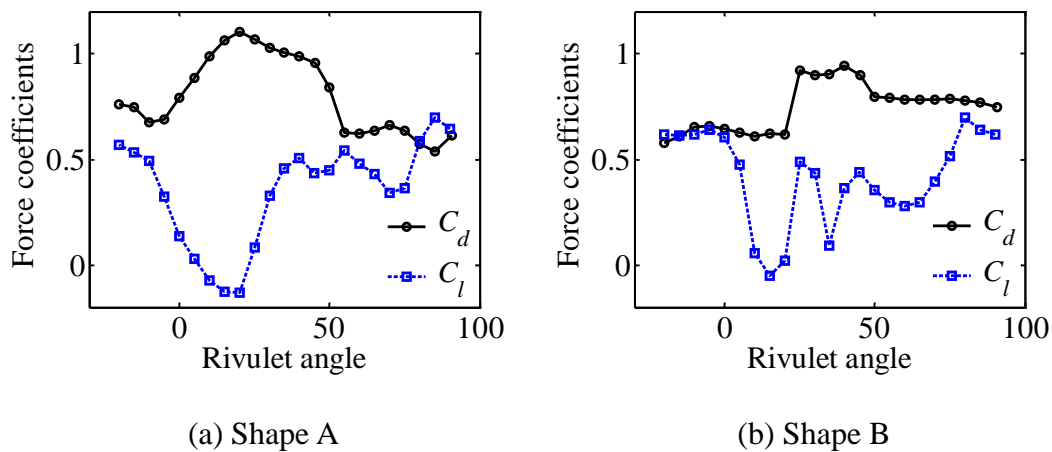
Figure 6-7. Lift and drag coefficients of the cable ($\alpha = 30°$, $\beta = 35°$) measured by

Xu et al. (2006)

It is worth to note that both the lift and the drag force coefficients were measured on the basis of the body coordinate of the cable model.

6.3 Numerical analysis on the model tested by Hikami and Shiraishi (1988)

To verify the effectiveness of the proposed numerical model, it is applied to the cable model tested by Hikami and Shiraishi (1988). The cable's responses are calculated and compared with the wind tunnel test results.

6.3.1 Numerical Results of the RWIV

The cable model was 160 mm in the external diameter, the mass was 10.2 kg/m, the fundamental frequency was 1 Hz, and the structural damping ratio was 0.2%. Both the inclination angle and the yaw angle were 45°. The maximum displacement of the cable was measured approximately 20 cm and the corresponding vibration of the

upper rivulet was approximately 12°. Consequently, the amplitude ratio (c_θ) is calculated as 0.6 °/cm according to Equation (6-15). The initial position of the upper rivulet under different incoming wind speeds was measured and shown in Figure 6-7. The aerodynamic force coefficients shown in Figure 6-4 are adopted to calculate the responses of the cable.
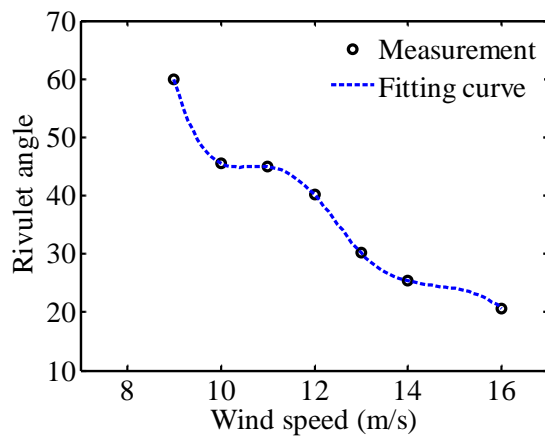
Figure 6-8. Initial position of the upper rivulet (Hikami and Shiraishi 1988)

In the numerical analysis, the initial displacement of the cable model is set as 0.1 cm. The responses of the cable are calculated by solving Equation (6-7). The numerical results are compared with the wind tunnel tests in Figure 6-9. Both results show that the RWIV occurs within a certain range of wind speed. In the wind tunnel tests, the RWIV of the cable occurred in the wind speed range of 9.5 m/s to 14.0 m/s. When the wind speed was above 9.5 m/s, the cable vibration amplitude increased and reached the maximal value of 18.1 cm approximately under the wind speed of 12.0 m/s. After that the amplitude reduced with the increase of wind speed until the RWIV disappeared at the wind speed of 14.0 m/s. The numerical results show that the RWIV occur within the wind speed range of 9.0 m/s to 12.0 m/s, narrower than that of the wind tunnel test. Within the wind speed range of 9.5 m/s to 11.5 m/s, large

amplitude cable vibration occurs and the maximal amplitude is approximately 22.1 cm, larger than the maximal value measured in the wind tunnel test. When the wind speed is above 12.0 m/s, the cable vibration completely disappears. The calculated responses of the cable are velocity- and amplitude-restriction, which captures the main feature of the RWIV. The numerical and experimental results are not exactly consistent. Their difference might be caused by the difference of the rivulet simulation between the wind tunnel tests by Xu et al. (2006) and Hikami and Shiraishi (1988).
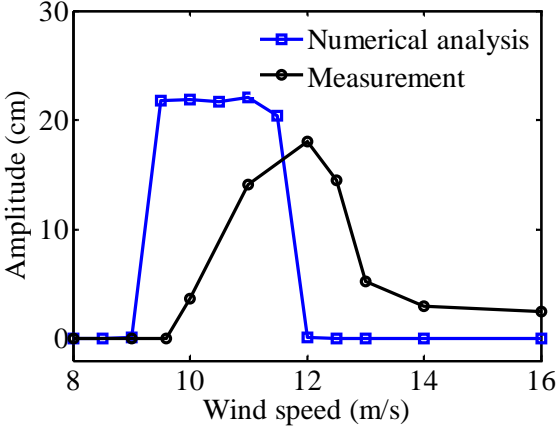
Figure 6-9. Comparison of analytical and experiment results

Figure 6-10 shows the time history of the cable vibration calculated through the proposed analytical model under the wind speed of 11.0 m/s. The vibration amplitude significantly increases during the period of 50 s to 150 s and reaches a steady state after 200 s. The time history of the cable displacement is sinusoidal and the vibration frequency equals to the fundamental frequency of the cable model.
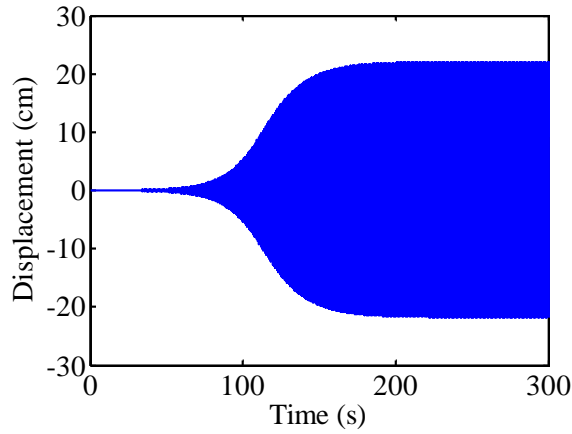
(a)
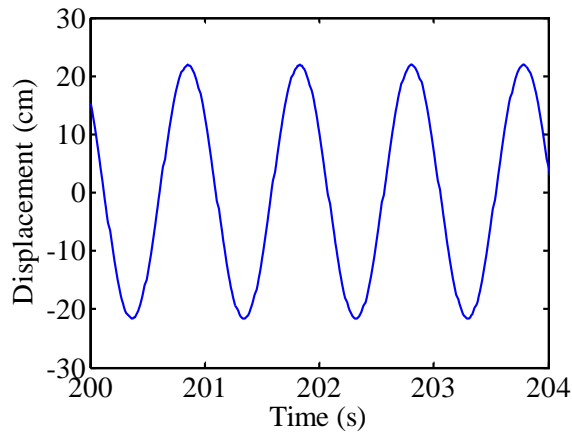
(b)

Figure 6-10. Time history of the cable vibration by numerical analysis

Figure 6-11 shows the time history of the dynamic vertical wind load acting on the cable. The maximum value was approximately 4.5 N, while the minimum was −3.2 N. Figure 6-12 shows the time history of the rivulet angle and the attacking angle induced by the cable and upper rivulet vibrations after the vibration reaches steady state. In Figure 6-12(a), the relative position of the upper rivulet considering the effects of the attacking angle harmonically vibrates between 32° and 58° with the neutral position of 45°. In Figure 6-12(b), the attacking angle varied between −6.5° and 5.6°.
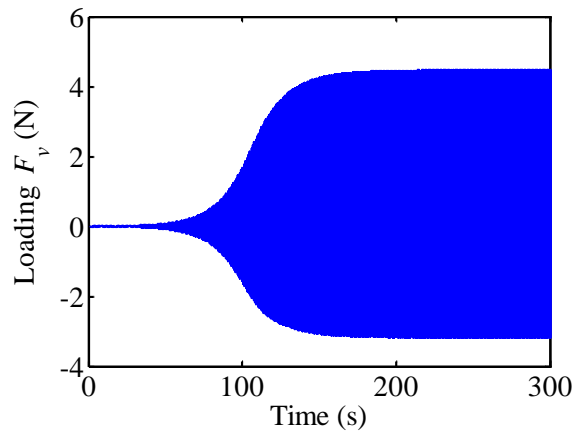
(a)
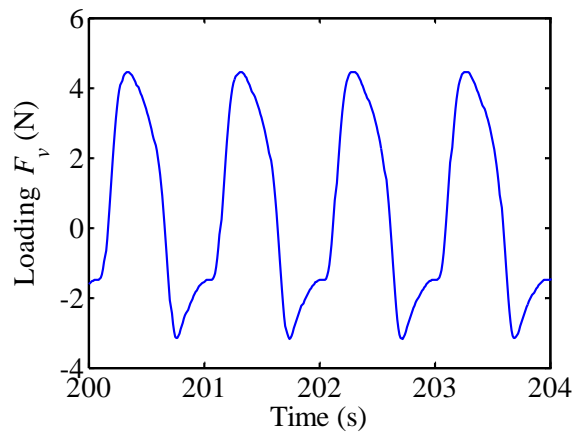
(b)

Figure 6-11. Time history of the calculated vertical wind loads
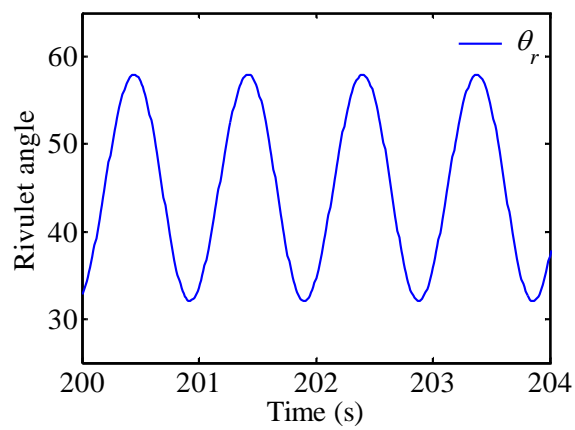
(a)
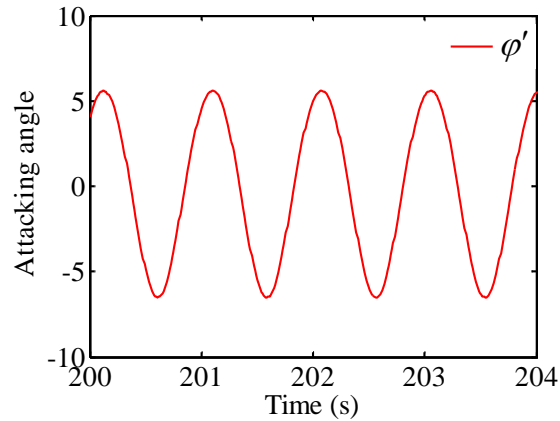
(b)

Figure 6-12. Upper rivulet position and the attacking angle the attacking angle induced by the cable and upper rivulet vibrations

The pattern of the dynamic vertical wind loading is similar to that of the cable displacement. It increases first and then remains constant after 200 s. However, as Figure 6-11(b) shows, it is non-sinusoidal. This is because the wind load is directly related to the rivulet angle and the attacking angle induced by the cable and upper rivulet vibration, as Figure 6-6 and Equation (6-8) indicate. When the upper rivulet moves between 32° and 45°, the lift force coefficient first slowly decreases and then rapidly increases with the increase of the rivulet angle, the drag force coefficient, on the contrary, first increases and then decreases with the increase of the rivulet angle. When the upper rivulet moves between 45° and 58°, the lift force coefficient always rapidly increases and the drag force coefficient always rapidly decreases with the increase of the rivulet angle. This causes the asymmetry of the maximum and minimum dynamic forces. Besides, there are two obvious inflection points when the wind loading is negative. The value of the two inflection points is different because when the upper rivulet moves from 32° to 45°, the attacking angle is negative, the projection of the drag force enhances the vertical loading, on the contrary, when the

131

upper rivulet moves from 45° to 32°, the attacking angle is positive, the projection of the drag force reduces the vertical loading.

Figure 6-13 compares the dynamic component of the upper rivulet (θ_v), the attacking angle induced by the cable vibration (φ_y), and the dynamic component of the relative rivulet position (θ_r^d). The blue solid line is θ_v, which vibrates with the amplitude of 11° in-phase with the cable displacement. The red dash line is φ_y, which vibrates with the amplitude of 6° in-phase with the cable velocity. The black dot dash line is θ_r^d considering the variation of the attacking angle, which approaches to $\theta_v - \varphi_y$ because φ_θ is negligible compared with θ_v and φ_y.
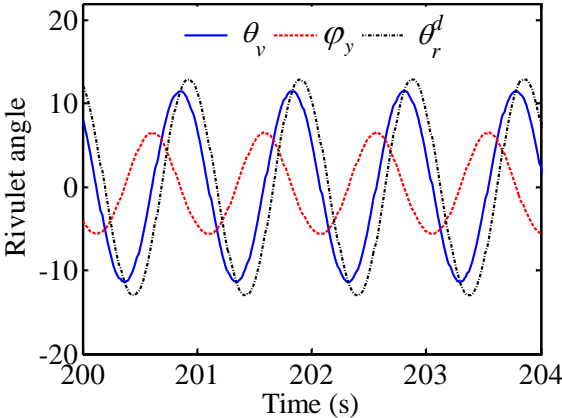
Figure 6-13. Time history of the dynamic position of the upper rivulet, the attacking angle induced by the cable vibration, and the dynamic component of the relative rivulet position

6.3.2 Parametric Analysis

The RWIV is complex and very sensitive to many factors, such as the wind speed

132

and direction, mass, damping, fundamental frequency, surface condition of the cable model, intensity of the rainfall, and so on. To better understand the effects of these parameters on the RWIV, the parametric analyses are carried out using the proposed numerical model. The basic parameters of the numerical model are listed in Table 6-1. The effects of the upper rivulet vibration, structural damping, and frequency of the cable model on the RWIV will be investigated. For different parameters, the cable responses are calculated by solving Equation (6-7).

Table 6-1. Properties of the cable model (Hikami and Shiraishi 1988)

Parameters	Value	Parameters	Value
D	160 mm	α	45°
m	10.2 kg/m	β	45°
f	1.0 Hz	c_θ	0.60 °/cm
ξ_s	0.2%		

(a) Effect of the upper rivulet vibration on the RWIV

Figure 6-14 shows the calculated amplitude of the cable vibration under different wind speeds when the amplitude ratio (θ_c) varied from 0.6 °/cm to −0.6 °/cm. A positive amplitude ratio means that the upper rivulet vibrates in-phase with the cable vibration, a negative amplitude ratio means that the rivulet vibrates anti-phase with the cable vibration (a phase difference of π), and zero indicates the rivulet is fixed on the cable surface without relative vibration to the cable during the RWIV. The calculated results show that the upper rivulet vibration amplitude has no effect on the

133

wind speed range of the RWIV, but has significant effects on the amplitude of the cable vibration. Under the same wind speed, the cable vibration reaches the maximum when the upper rivulet is fixed on the cable surface ($\theta_c = 0$ °/cm). When the upper rivulet is vibrating on the cable surface, no matter in-phase or anti-phase with the cable vibration, the amplitude of the cable vibration reduces with the increase of the upper rivulet vibration. The amplitude of the cable reduces by 50% when the amplitude ratio increases from 0°/cm to 0.6°/cm. Besides, for the same value of amplitude ratio, the amplitude of the cable vibration is slightly larger when the upper rivulet oscillates anti-phase with the cable vibration than that in-phase.
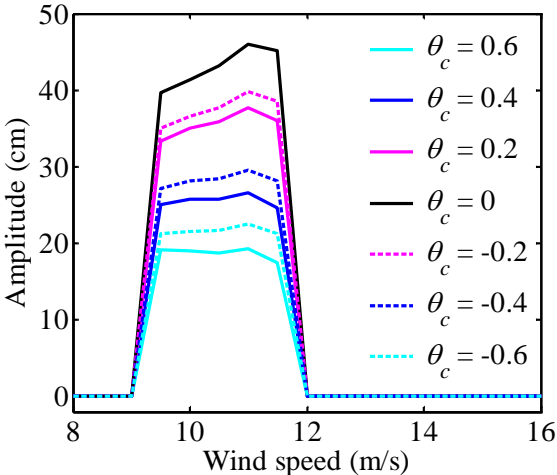
Figure 6-14. Effect of the upper rivulet vibration amplitude ratio on the RWIV

(b) Effect of damping on the RWIV

Figure 6-15 shows the calculated amplitude of the cable vibration with different damping ratios under different wind speeds. Six cases are calculated with the structural damping ratio varying from 0.1% to 1.0%. The numerical results show that the structural damping ratio has a significant effect on both the amplitude and the wind speed range of the RWIV. When the structural damping ratio is equal to or

smaller than 0.6%, the large cable vibration occurs at the wind speed of 9.0 to 12.0 m/s. However, when the structural damping ratio is equal to or greater than 0.8%, the large cable vibration occurs at the wind speed of 9.5 m/s to 12.0 m/s. The structural damping ratio narrows the wind speed range of the RWIV. Besides, under the same wind speed, the cable amplitude decreases under a larger structural damping ratio. Therefore, the structural damping restrains the RWIV, as expected. The amplitude of the cable vibration decreases by 65% in general when the structural damping ratio increases from 0.1 % to 1.0 %.
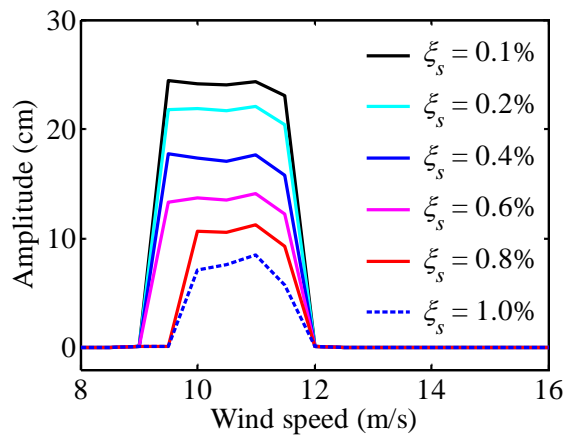
Figure 6-15. Effect of structural damping on the RWIV

(c) Effect of Cable Fundamental Frequency on the RWIV

Figure 6-16 shows the effects of the cable fundamental frequency on the RWIV. Four cases are calculated with the frequency varying from 1 Hz to 4 Hz. The results show that the cable fundamental frequency has effects on the amplitude of vibration and the wind speed range of the RWIV. The amplitude of the vibration decreases by 75% in general when the cable fundamental frequency increases from 1 Hz to 4 Hz. The wind speed range of the RWIV becomes narrow when the cable fundamental frequency is above 3 Hz.
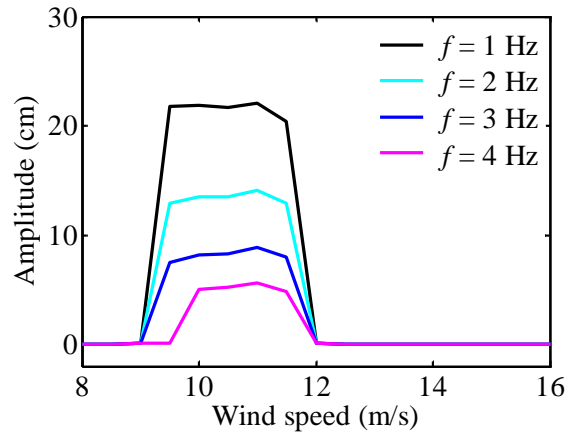
Figure 6-16. Effect of frequency on the RWIV

6.4 Numerical Analysis on the Present Cable Model

The parameters of the cable model are listed in Table 6-2. The water flow rate of the upper rivulet was measured as $Q = 0.7463$ mL/s. In the present wind tunnel test, both the cable and upper rivulet vibration on the cable surface were simultaneously measured using the digital image processing method. The detail of this method please refers to Chapter Four.

Table 6-2. Properties of the present cable model

Parameters	Value	Parameters	Value
D	160 mm	α	32°
m	33.0 kg/m	β	35°
f	1.39 Hz	c_θ	0.71 °/cm
ξ_s	0.06 %		

Figure 6-16 shows the measured amplitude of the RWIV versus the incoming wind

speed. Large cable vibration occurred when the wind speed was above 8.5 m/s and the amplitude increased with the incoming wind speed. The largest cable vibration occurred at the wind speed of 13 m/s with the amplitude of 18.6 cm. The largest wind speed of the experiments was 15 m/s because of the limitation of the wind tunnel.
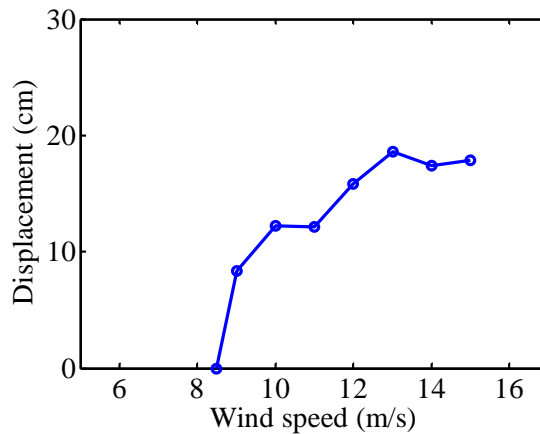
Figure 6-17. Amplitude of the measured RWIV versus the incoming wind speed

Figure 6-18 shows the measured upper rivulet position versus the incoming wind speed during the RWIV. In this figure, the solid line represents the average rivulet position which is treated as the initial position (θ_0). The dash lines represent the angle range of the oscillating upper rivulet under each wind speed. The initial position of the upper rivulet decreases with the reduce of the incoming wind speed, similar as previous studies conducted by Hikami and Shiraishi (1988) and Gu and Du (2005). It steadily decreases from 35° at 8.5 m/s to 16° at 15.0 m/s. The amplitude ratio (c_θ) is calculated as 0.71 °/cm by linear fitting as Figure 6-19 shows.
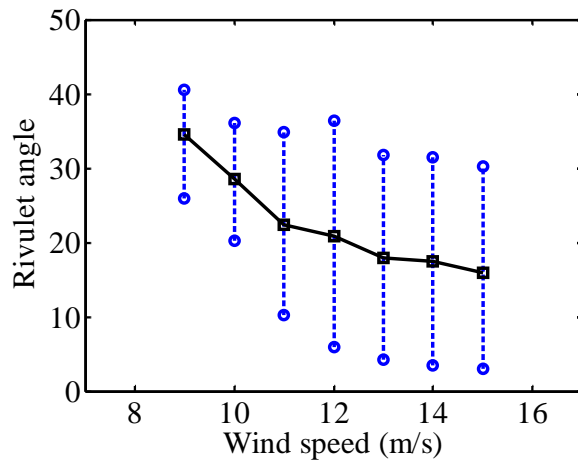
Figure 6-18. Upper rivulet position versus the incoming wind speed
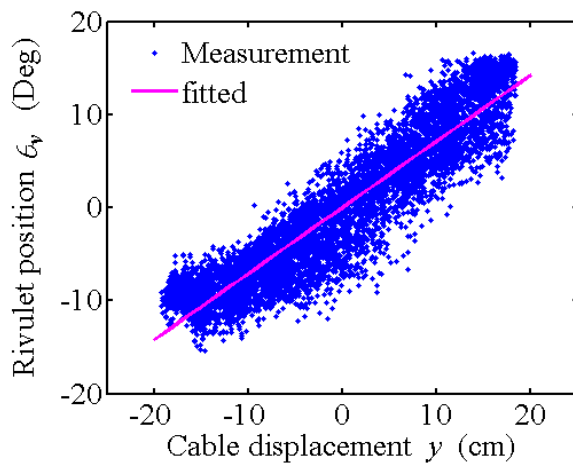
Figure 6-19. Rivulet position versus cable displacement

The proposed numerical model is also applied to the cable. Two cases, namely Case A and Case B, are investigated using the two sets of aerodynamic force coefficients (Shapes A and B, respectively) shown in Figure 6-7. The calculated cable vibration amplitudes are shown in Figure 6-20. The on-set wind speed of Case A is lower than Case B, and the maximum vibration amplitude in Case A is smaller than Case B. For Case A, the cable has large vibrations when the wind speed ranges from 11.0 m/s to 13.5 m/s, with the largest amplitude of 8.4 cm occurring at the wind speed of 12.0

m/s. For Case B, the large cable vibration occurs when the wind speed is over 12.0 m/s. The upper wind speed limit of the RWIV is not obtained. The largest cable vibration occurs under the wind speed of 15.0 m/s with the amplitude of 14.2 cm.

Compared with the wind tunnel test, the large cable vibrations are calculated within a narrower wind speed range for both numerical cases. The on-set wind speed of the RWIV in both numerical cases is higher than that of wind tunnel tests and both have smaller cable vibrations.
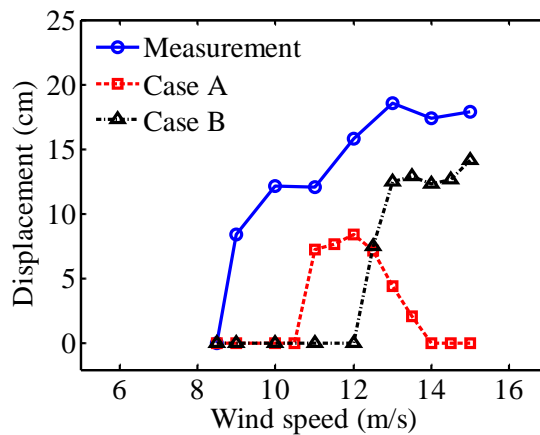
Figure 6-20. Comparison of the cable vibration amplitude between the analytical and experimental results

6.5 Summary

In this chapter, a numerical model was adopted to simulate the RWIV using the aerodynamic force coefficients measured on a three dimensional cable model. Large cable vibrations were calculated within certain wind speed range. The effects of the rivulet movement, structural damping ratio, and cable's fundamental frequency on the RWIV were investigated by parametric studies. The RWIV measured in the wind

tunnel tests and the numerical results were compared. The main conclusions are as follows:

(1) The numerical model can predict the large cable vibrations and the numerical results captured the main features of the RWIV measured in wind tunnel tests.

(2) The movement of the upper rivulet significantly affects the amplitude of the RWIV, in particular, the cable amplitude decreases when the upper rivulet vibration amplitude increases.

(3) The structural damping ratio constrains the occurrence and amplitude of the RWIV.

(4) The cable's frequency significantly affects the amplitude of the RWIV but has less effect on the wind speed range.

(5) The size of the artificial upper rivulet affects the aerodynamic force coefficients and consequently influences the cable vibration, which needs more detailed investigation in the future.

CHAPTER SEVEN

EXCITATION MECHANISM OF RWIV THROUGH

WIND TUNNEL TESTING

7.1 Introduction

Extensive research has been conducted to reveal the excitation mechanism of the RWIV through wind tunnel tests and numerical methods. Several possible excitation mechanisms have been proposed as follows:

(1) The RWIV is a modified galloping. The upper rivulet or the axial flow generates the negative slope in the lift force coefficients, which makes the cable instable (Hikami and Shiraishi 1988; Xu and Wang 2003; Matsumoto et al. 1992, 1995; Wilde and Witkowski 2003; Cao et al. 2003; Xu et al. 2006; Gu and Huang 2008; Gu 2009);

(2) The RWIV is a new type of vortex induced vibration. The interaction between the classical Karman vortex and the axil flow generates a new type of vortex-shedding with a long period (Matsumoto et al. 1995, 1998).

(3) The RWIV is caused by the flow regime modification. The vibrating rivulet, as a disturbance around the transition point of the flow, induces the periodical transition of the flow between pre-critical and critical states, which transfers the energy from the flow to the elastic structure (Cosentino et al. 2003a, b; Seidel and Dinkler 2006).

(4) The RWIV is caused by the swirling flow traveling along the inclined cable. The swirling flow is developed on both sides of the cable, moves obliquely to the centreline, and alternately sheds, generating the exciting forces on the yawed and inclined cable (Yeo and Jones 2008, 2012).

The importance of the upper rivulet in these possible excitation mechanisms of the RWIV has been widely reported. However, the information of the upper rivulet has not been well studied in the previous wind tunnel tests and numerical analyses. Most of these studies regard the rivulet as a solid attachment on the cable surface without considering the effect of the variations of the rivulet's thickness and shape on the aerodynamic forces and the air-rivulet interaction. This assumption is not consistent with the actual rivulet measured by Cosentino et al. (2003a) and Li et al. (2010a).

The current study investigates the upper rivulet in detail through wind tunnel testing and proposes a new excitation mechanism of the RWIV based on the effect of the oscillating upper rivulet on the state of the air boundary layer.

7.2 Wind Tunnel Tests

The wind tunnel test is the subsequent test of Chapter Three. The color of the upper rivulet was adjusted so that more detail information of the upper rivulet could be recorded by the digital camera during the RWIV. The fundamental frequency was identified as 1.37 Hz from the free vibration test. The cable damping ratio was 0.17%. The corresponding Scruton number was calculated as $S_c = 4\pi m \xi_s / \rho D^2 = 21.35$. The water rivulets were simulated by guiding water lines as described in Chapter Three and the flow rate was 7.46×10^{-7} m³/s. The incoming wind speed was 12.1 m/s.

142

Both the upper rivulet and cable vibration were measured using the digital image processing method, as descried in Chapter Four. The upper rivulet's position (θ) is measured anti-clockwise from the cable top as Figure 4-5(b) shows. The downward cable displacement (*y*) is defined as positive. The angle of the upper rivulet measuring from the stagnation point is $\theta_s = \varphi + \pi / 2 - \theta$.

The RWIV was successfully reproduced in the wind tunnel and the time history of the cable vibration is shown in Figure 7-1. The cable vibrates at the fundamental frequency of the cable with the amplitude of 74.2 mm, which corresponds to the non-dimensional amplitude of 0.46 (74.2/160.0).
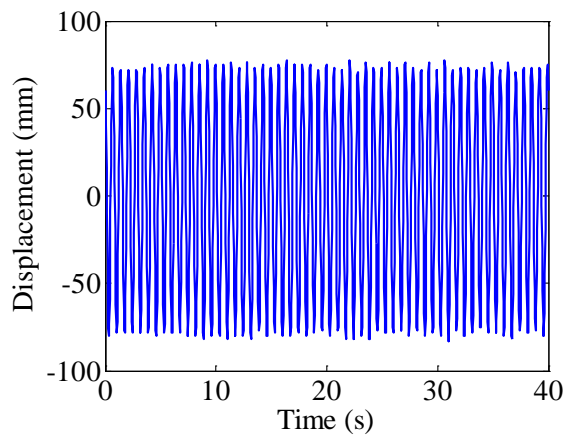
Figure 7-1. Time history of cable vibration

7.3 Characteristic of the Rivulets in the RWIV

The time history of the upper rivulet vibration is shown in Figure 7-2. Since the rivulet position slightly varied along the cable, this figure shows the position averaged along the longitudinal direction. The averaged upper rivulet oscillated

between 6.6° and 33.0°, with a neutral position of 19.8°. The vibration frequency of the averaged upper rivulet was the same as the fundamental frequency of the cable. Figure 7-3 compares the averaged upper rivulet position and the cable displacement. It shows that the upper rivulet oscillated almost in-phase with the cable. When the cable vibrated upward (the displacement becomes smaller in the figure), the upper rivulet moved leeward (the angle becomes smaller). Conversely, when the cable vibrated downward, the rivulet moved upwind. Cosentino et al. (2003a) also observed this phenomenon, in which the mean position of the upper rivulet oscillated between 13° and 25°.
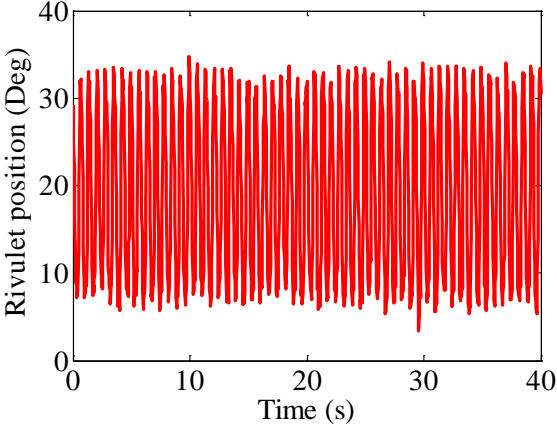
Figure 7-2. Time history of the upper rivulet
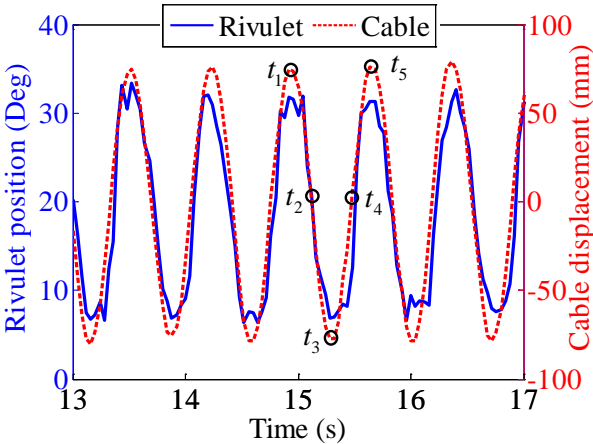
Figure 7-3. Comparison of the upper rivulet and cable oscillation

Images of the upper rivulet during one cycle (t_1 to t_5) are shown in Figure 7-4 to discover the relation between the upper rivulet and the cable vibration. t_1 to t_5 corresponds to the period of 14.92 s to 15.64 s in Figure 7-3.

$t = 14.92$ s (t_1)

$t = 14.96$ s

$t = 15.00$ s

$t = 15.04$ s

$t = 15.08$ s

$t = 15.12$ s (t_2)

$t = 15.16$ s

$t = 15.20$ s
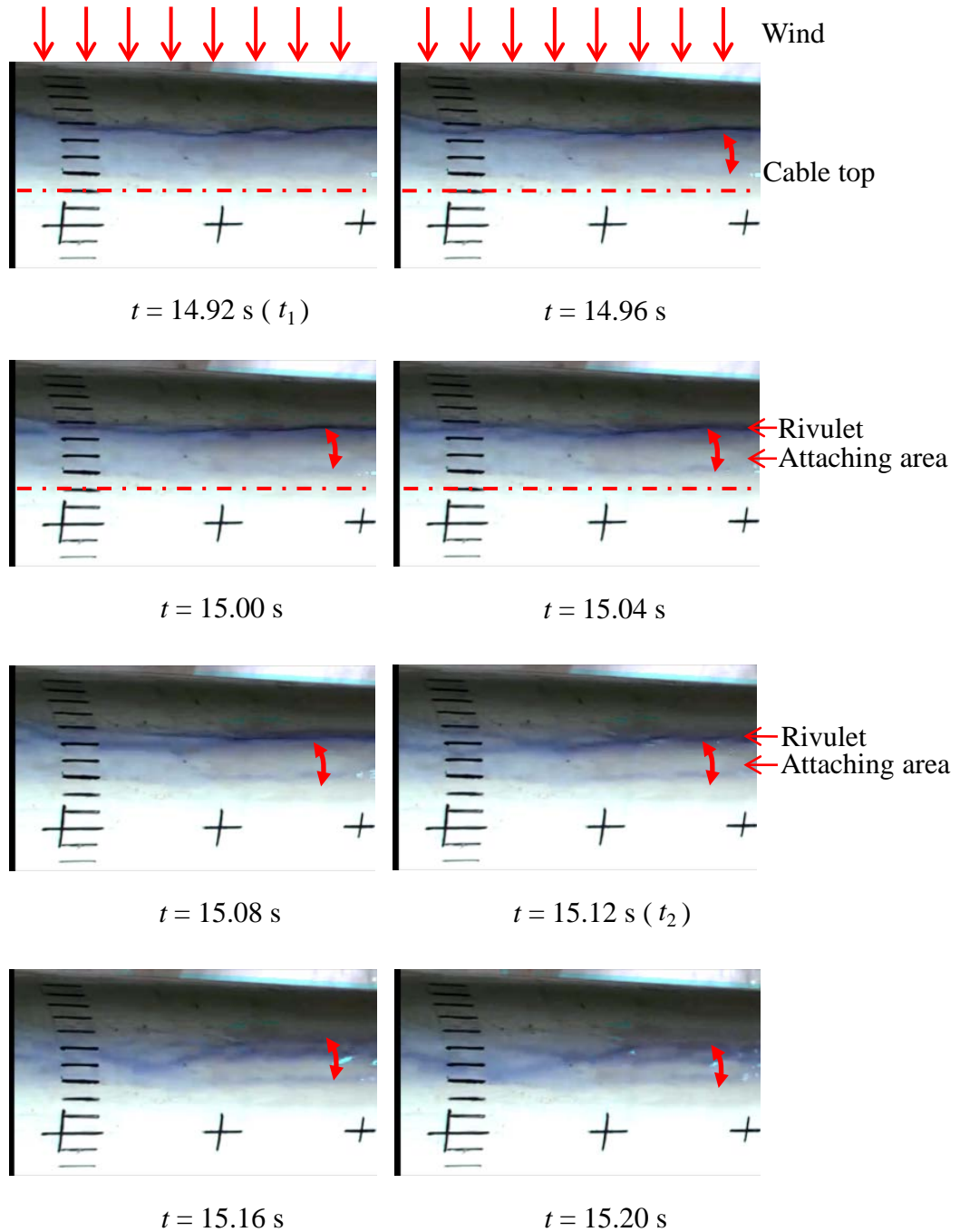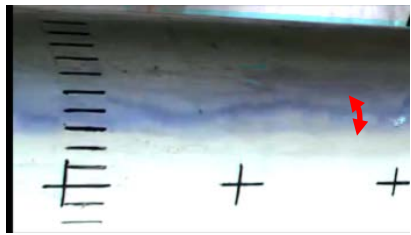
$t = 15.24$ s
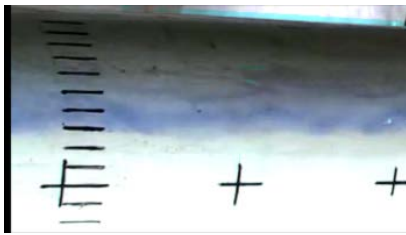
$t = 15.28$ s (t_3)
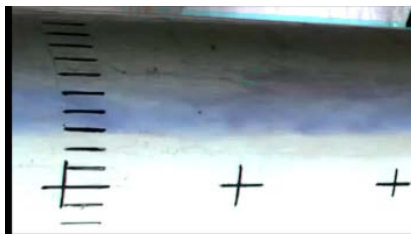
$t = 15.32$ s
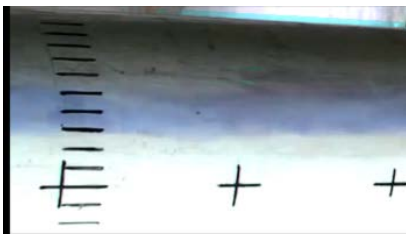
$t = 15.36$ s
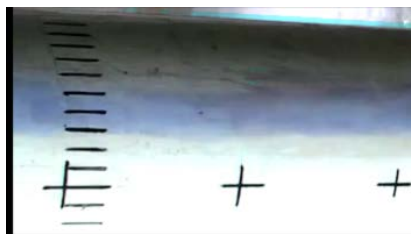
$t = 15.40$ s
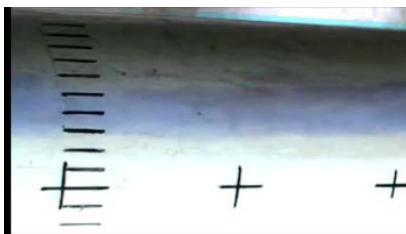
$t = 15.44$ s
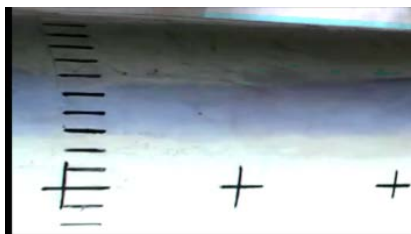
$t = 15.48$ s (t_4)
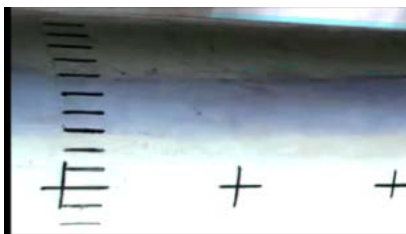
$t = 15.52$ s
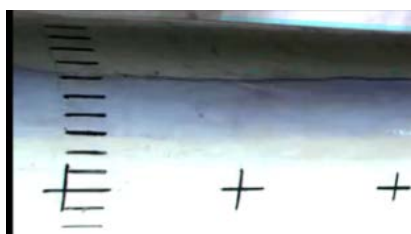
$t = 15.56$ s
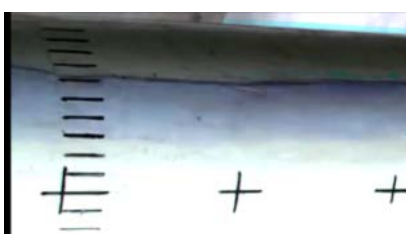
$t = 15.60$ s
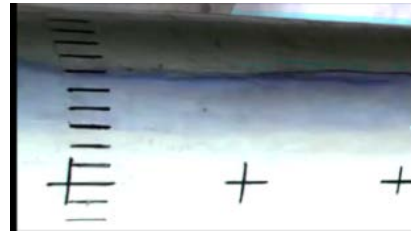
$t = 15.64$ s (t_5)

Figure 7-4. Captured images of the upper rivulet from t_1 to t_5 (⬍ denotes the

attaching area)

At t_1 ($t = 14.92$ s), the cable was located at the lowest position and the upper rivulet was located away from the cable top. The upper rivulet was hump-shaped with a carpet behind and coherent along the cable axis. The cable then vibrated upward from the lowest position. The upper rivulet moved leeward from 14.92 to 15.12 s (t_1 to t_2) and maintained the hump shape and coherence. However, the carpet behind the rivulet was pressed and forced to gather in leeward, forming another smaller hump far behind the rivulet, as shown clearly at $t = 15.12$ s. After the cable and upper rivulet passed their neutral position around t_2 (15.12 s), the upper rivulet began to flatten and the distribution along the cable axis became less coherent as shown at $t = 15.20$ s. During this process, the color intensity of the images became weaker, indicating that the water became thinner. When the cable reached the highest position at t_3 ($t = 15.28$ s), the rainwater spread out, resembling a water carpet with a wide and flat geometry. The rainwater was coherently distributed along the cable axis. The surface of the upper rivulet became smooth and almost stuck on the cable surface.

When the cable vibrated downward, the upper rivulet slid back upwind. From t_3 to t_4, the upper rivulet maintained its flat shape and smooth surface such that its location and movement were almost indistinguishable in the figure (the video

147

provides better contrast and the rivulet is recognizable). After the cable and the upper rivulet crossed their equilibrium positions (from t_4 to t_5), the upper rivulet began to gather and rose to the most upwind position. When the cable reached the lowest position at t_5 ($t = 15.64$ s), the upper rivulet became thickest, as that at t_1.

The above observation shows that the geometry of the upper rivulet is strongly related to the cable vibration. During the one-cycle cable vibration, the upper rivulet varies not only in position but also in thickness, distribution, and shape. The observed in-phase vibrations of the upper rivulet and the cable are consistent with the previous measurement by Cosentino et al. (2003a). However, the variation of the upper rivulet's thickness of the two studies is different. Cosentino et al. (2003a) observed the upper rivulet gathered during the cable descending and the thickest upper rivulet was observed when the cable was close to the equilibrium position. The upper rivulet then spread out when the cable reached the lowest position and became disorganized when the cable vibrated upward.

According to the observation of Figure 7-4, the morphology of the upper rivulet's evolution during one cycle is sketched in Figure 7-5. In this figure, to have a better visualization, the upper rivulet is exaggerated and the cable movement is amplified. θ_0 represents the neutral position of the upper rivulet.
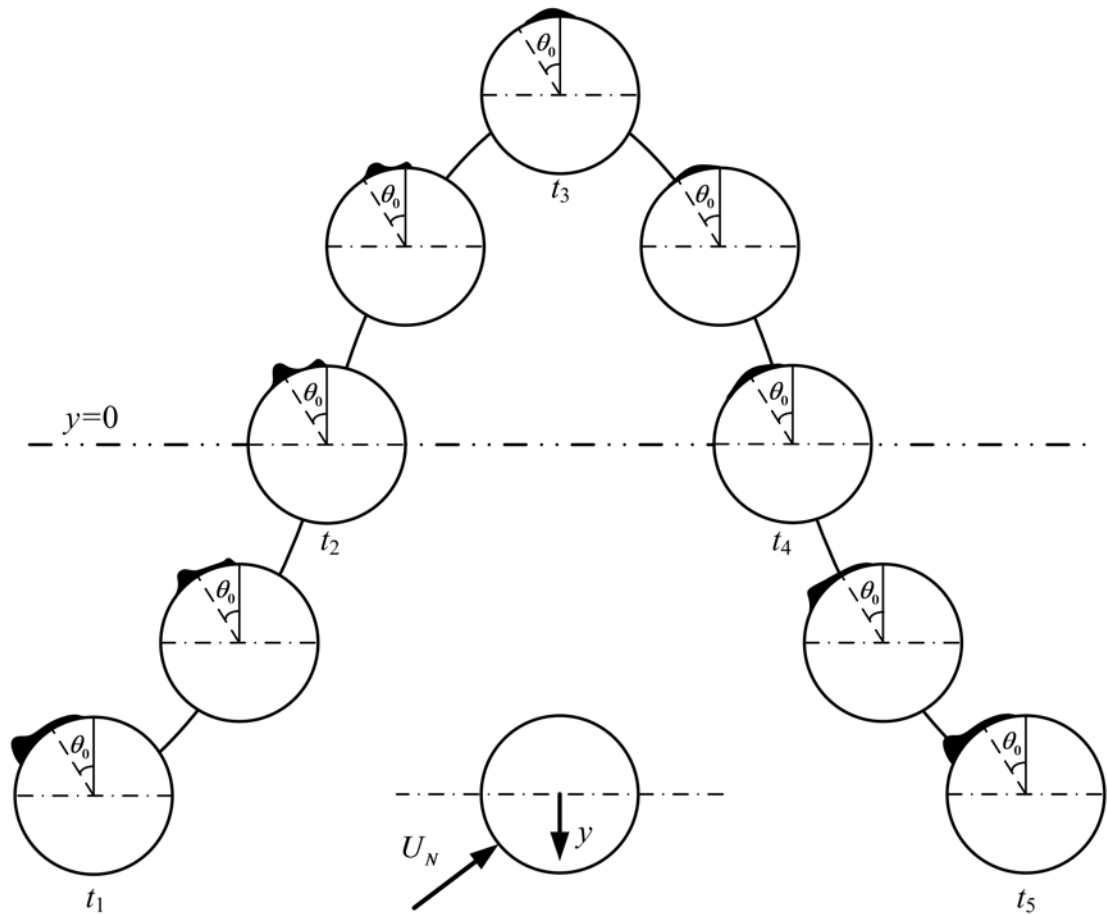
Figure 7-5. Morphology of the upper rivulet evolution during the RWIV

During this process, the upper rivulet reveals the separation state of the boundary layer, similar to the oil in flow visualization using the surface oil flow technique (Kleissl and Georgakis 2012). When the cable vibrates upward, the boundary layer attaches between the two humps. As a result, the wind pressure increases and the water carpet is pushed leeward. However, when the cable vibrates downward, the boundary layer returns to separate at the starting point of the first hump, and the upper rivulet is located within the separated boundary layer. Therefore, the water carpet maintains its wide, thin, and flat geometry during t_3 to t_4 and begins to gather at the first hump after t_4.

149

7.4 Excitation Mechanism of the RWIV

From the above observed upper rivulet and cable vibrations, a new excitation mechanism of the RWIV is proposed on the basis of a flow passing a dry inclined circular cylinder (Flamand and Boujard 2009; Nikitas et al. 2012; Jakobsen et al. 2012).

The upper rivulet induced the boundary layer to attach when the cable vibrated upward. The possible wind flow field at different instants is sketched in Figure 7-6 based on the morphology evolution of the upper rivulet, in a similar way as Devenport (2003) did. In the figure, the upper rivulet is exaggerated for enhanced visibility, the coordinate rotates clockwise so that the normal wind speed is in the horizontal direction, and the lower rivulet is not shown because of its little effect on the RWIV. At t_1 or t_5, when the cable is located at the lowest position, the boundary layer separates at the beginning of the hump, namely the original separation point, as shown in Figure 7-6(a). When the cable vibrates upward (t_1 to t_3), the boundary layer attaches between the two humps, flows along the cable surface, and then separates at a new position far behind the original separation point [Figure 7-6(b)]. When the cable vibrates downward (t_3 to t_5), the boundary layer returns to separate at the original separation point [Figures 7-6(c), (d)].

(a) t_1 or t_5

(b) t_2

(c) t_3

151
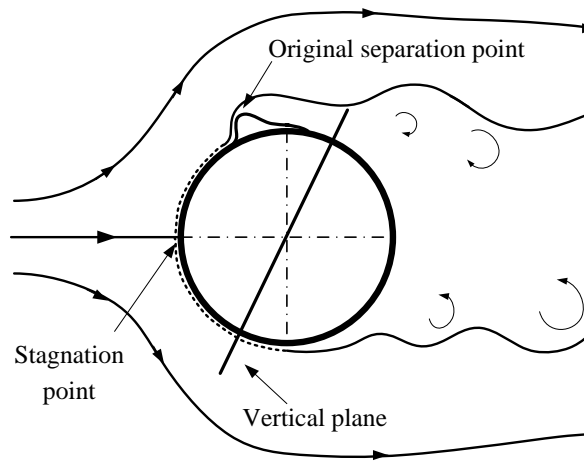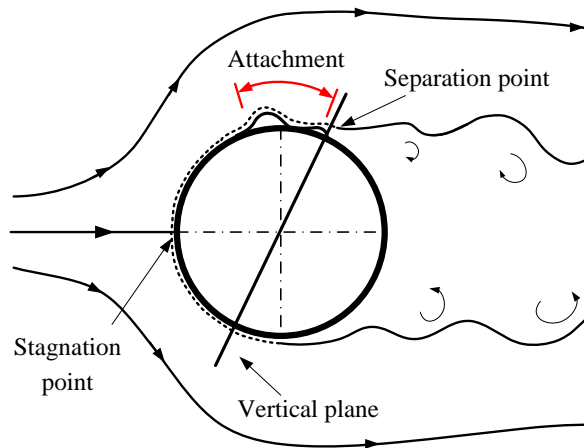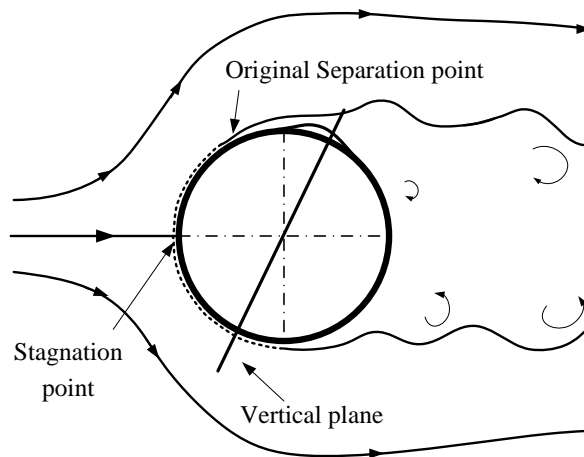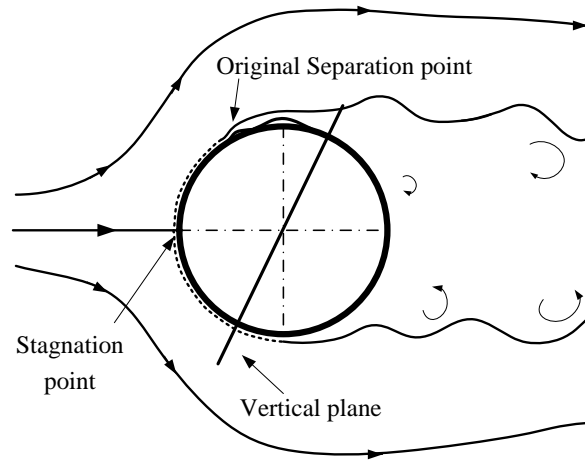
(d) t_4

Figure 7-6. Sketch of a flow passing the cable

The different flow state generates different wind pressure distribution around the cable. In particular, the boundary layer attachment significantly affects the wind pressure distribution around the cable (Zdravkovich 1997). After the transition occurs in the boundary layer, the flow state can be categorized into five flow regimes (Zdravkovich 1997): pre-critical regime [(100k–200k) < R_e < (300k–340k)], one-bubble regime [(300k–340k) < R_e < (380k–400k)], two-bubble regime [(380k–400k) < R_e < (500k–1M)], super-critical regime [(500k–1M) < R_e < (3.5M–6M)], and post-critical regime [(3.5M–6M) < R_e]. In the one-bubble regime, the boundary layer reattaches to one side of the cylinder. This asymmetric reattachment of the boundary layer forms a separation bubble on one side of the cylinder and produces a much larger negative pressure on this side than on the opposite side (Figure 7-7), thereby generating a significant lift force. When the wind is normal to the circular cylinder, the reattachment stochastically occurs on either side in this regime (Zdravkovich 1997). Recently, Larose et al. (2003), Flamand and Boujard (2009), Nikitas et al. (2012), Jakobsen et al. (2012), and Nikitas and Macdonald (2015)

measured the wind pressure around an inclined dry cable in the critical Reynolds number regime. They observed that in the one-bubble regime, the asymmetric boundary layer attachment generated the asymmetric pressure distribution and induced the sudden increase in the lift coefficient. Different from the wind normal to the cable case, for the inclined and yaw cable, asymmetric reattachment always occurs on the same side (Flamand and Boujard 2009) because the boundary layer is highly sensitive to disturbances, surface roughness, and turbulent free stream.
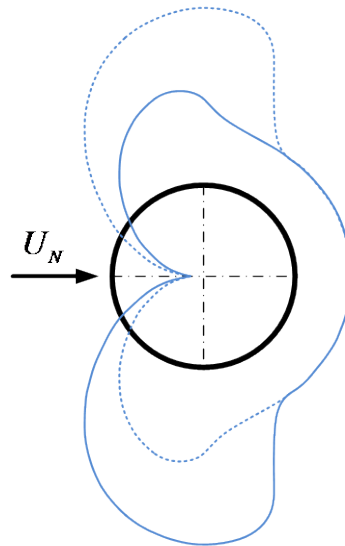
Figure 7-7. Wind pressure distribution in the one-bubble regime (Zdravkovich, 1997) (solid line denotes a reattachment occurring on the lower side; dashed line denotes a reattachment occurring on the upper side)

In this test, the asymmetric attachment occurred at the Reynolds number of 1.3×10^5, in the pre-critical regime and much lower than that in the one-bubble regime of the dry cable. Therefore, this attachment should be induced by the upper rivulet but not the Reynolds number effects as the dry cable.

Given the above properties of the asymmetric flow attachment to the inclined

cylinder, when the cable vibrates upward during the RWIV, the asymmetric boundary layer attachment may also lead to an asymmetric wind pressure and a significant lift force on the cable, even though the reason of the attachment differs from that of the one-bubble regime. Thus, when the cable vibrates upward, the upper rivulet induces the boundary layer to attach to the upper side of the cable, generating a significant upward aerodynamic force. The pressure distribution induced by the asymmetric attachment is assumed to be similar to Figure 7-7 and is sketched in Figure 7-8a. Since the aerodynamic force is upward when the cable vibrates upward, it produces a positive work and excites the cable. When the cable reaches the highest position and starts to vibrate downward, the upper rivulet spreads out and becomes a water carpet. The boundary layer fails to attach and turns to separate at the original separation point. The corresponding pressure distribution becomes symmetric around the cable as that in the pre-critical regime, as Figure 7-8b shows. The aerodynamic force produces negative work as in the pre-critical regime. Finally, when the positive work done by the aerodynamic force is equal to the negative work done by the structural damping during a cycle, the cable vibration reaches a steady state.
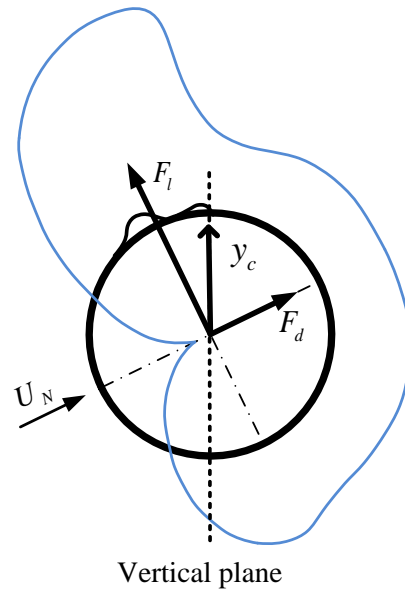
(a) Cable vibrates upward
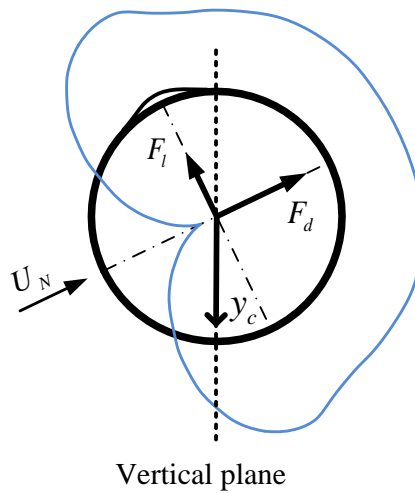
(b) Cable vibrates downward

Figure 7-8. Sketch of pressure distribution on the cable (F_d : drag force; F_l : lift force)

Similar explanations have been proposed by Cosentino et al. (2003a, b) and Seidel and Dinkler (2006). Cosentino et al. (2003a, b) treated the upper rivulet as an obstacle close to the upper boundary layer separation point and modified the flow state from the pre-critical regime to the critical regime. They observed that the

rainwater gathered at the cable top when the cable moved downward and assumed that the gathered upper rivulet modified the flow regime into the one-bubble regime, which generated a downward aerodynamic force and produced a positive aerodynamic work to excite the cable vibration. Seidel and Dinkler (2006) considered the upper and lower rivulets as movable disturbances and assumed that, when a rivulet is located at the separation area, the flow transits from the pre-critical regime to the critical regime, as what happens in the Prandtl tripwire phenomenon.

In summary, the new proposed excitation mechanism explains the large cable vibration with the interaction between the upper rivulet vibration, air boundary layer attachment, and the cable vibration, as shown in Figure 7-9. When the cable vibrates upward, the oscillating upper rivulet, as an obstacle, induces the air boundary layer to asymmetrically attach on the upper side of the cable, generating the significant upward aerodynamic force. The aerodynamic force excites the cable to vibrate at large amplitude. The large cable vibration, in turn, changes the attacking angle of the wind and provides inertial force on the upper rivulet, exciting the upper rivulet to steadily and circumferentially oscillate on the cable surface. Besides, the cable vibration also enhances the coherence of the upper rivulet along the cable and harmonizes the attachment of the air boundary layer along the cable, resulting in a larger resultant force on the cable. When the interaction between the cable, upper rivulet, and boundary layer reaches an equilibrium state, the RWIV of the cable becomes steady.
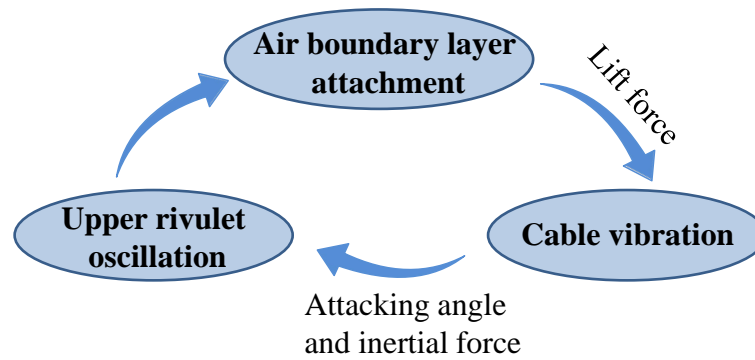
Figure 7-9. Interaction between the upper rivulet, air boundary layer, and the cable

7.5 Effect of Parameters on the RWIV

In Chapter Three, the characteristics of the RWIV has been obtained through wind tunnel testing such as the negligible lower rivulet, negative aerodynamic damping ratio, and effects of initial cable vibration. In this section, the observed results are explained by the proposed mechanism of the RWIV.

7.5.1 Different Roles of the Upper and Lower Rivulets

The upper rivulet was observed significantly affected the vibration of the cable while the lower one had little effects on the RWIV. The reason for the former has been explained, whereas the latter not yet and will be provided here.

Even though both the upper and lower rivulets are symmetrically located on the cable surface with respect to the stagnation point, as reported by Gu and Du (2005) and Lemaitre et al. (2007, 2010), they exhibit different states because of the different gravitational effects. As shown in Figure 7-10(a), the upper rivulet is subjected to gravity g, wind pressure P_u, and reaction of the cable S_u. γ_u and γ_d denote the upstream and downstream contact angle, respectively. The gravity tends to keep the

upper rivulet on the cable surface and causes the water under compression in the vertical direction. Therefore, the upper rivulet is prone to becoming relatively thin and flat and could induce the air boundary layer to attach on the cable surface.

When the cable is static, the upper rivulet randomly induces the air boundary layer to attach on the cable surface. The random attachment, in turn, causes a random excitation on the upper rivulet, making the upper rivulet moving forth and back in a non-stationary manner on the cable surface, as observed in Chapter Five. When the cable is vibrating, the upper rivulet regularly oscillates on the cable surface and periodically induces the air boundary layer to attach, which, in turn, generates the periodical aerodynamic forces to excite the upper rivulet and the cable.

As for the lower rivulet [Figure 7-10(b)], the gravity tends to pull the rainwater away from the cable and causes the water under tension in the vertical direction, making the lower rivulet thicker than the upper one (Li et al. 2010a). Besides, the gravity maintains the contact angles smaller than the critical angle, enhancing the stability of the lower rivulet. As a result, the lower rivulet may be so thick and stable or it is located at the leeward of the separation point that it could not induce the boundary layer attachment and could not generate the significantly aerodynamic forces to excite the rivulet and the cable. Consequently, the lower rivulet remains stationary when the cable is vibrating or static and it exerts minimal effect on the RWIV.

(a) Upper rivulet   (b) Lower rivulet
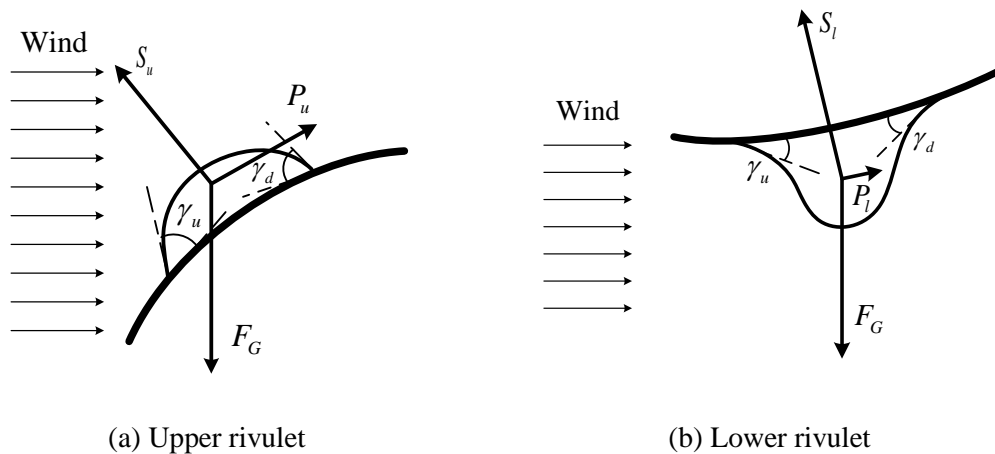
Figure 7-10. Forces on the upper and lower rivulets

7.5.2 Effects of the Cable's Damping and Initial Conditions

The initial condition of the cable has a significant effect on the RWIV, as observed in Chapter Three. This effect is related to the damping of the cable. When the cable has a larger damping ratio, a larger initial vibration is required to excite the RWIV. On the contrary, when the cable has a small damping ratio, a smaller initial vibration is required to excite the RWIV and the large initial vibration can quickly excite the cable to vibrate at a large amplitude.

The effects of the cable's initial condition on the RWIV can be explained by the proposed excitation mechanism. At the beginning, the cable is artificially excited to vibrate. The cable vibration periodically changes the attacking angle, resulting in a periodical wind force and a periodical inertial force on the upper rivulet. Therefore, the initial cable vibration excites the upper rivulet to periodically oscillate on the cable surface. The upper rivulet oscillation excited by the artificial cable vibration is different from that in the RWIV because there is a phase difference between the upper rivulet and cable vibrations. In the RWIV, the upper rivulet oscillates in-phase

159

with the cable. After the artificial excitation, the cable and upper rivulet vibration do not disappear immediately. In this process, the oscillating upper rivulet gradually induces the boundary layer to attach on the cable surface, which generates the aerodynamic forces to excite the cable and the upper rivulet. The aerodynamic forces and the cable vibration regularly adjust the phase difference between the upper rivulet and cable vibrations. After the upper rivulet regularly oscillates almost in-phase with the cable, it steadily induces the boundary to attach and generates steady aerodynamic forces on the cable and on itself. The rivulet and the cable begin to excite each other until reaching an equilibrium state.

For the cable with a large damping ratio, its vibration needs a sufficient aerodynamic force to overcome the structural damping. A larger initial excitation is required because the upper rivulet needs enough time to adjust its motion such that it oscillates in-phase with the cable vibration and steadily induces the boundary layer to attach. Otherwise, the aerodynamic forces induced by the upper rivulet would fail to overcome the structural damping of the cable. In turn, the decaying cable vibration further reduces the inertial force and wind force on the upper rivulet in maintaining the oscillation and shape. Consequently, the cable vibration keeps decaying as the damped free vibration.

For the cable with a small damping ratio, the cable needs smaller initial excitation because the decay of the cable vibration is relatively slow and there is enough time for the upper rivulet to adjust its motion and shape. If the cable is artificially excited to a large vibration at the beginning, the upper rivulet can quickly adjust the phase of the upper rivulet oscillation and its shape, making the cable-rivulet system

self-excited. Consequently, the cable-rivulet can reach an equilibrium state with a significant vibration amplitude.

7.6 Summary

In this chapter, a new excitation mechanism of the RWIV was proposed based on the observed upper rivulet's information and its relationship with the cable vibration. The main conclusions can be drawn as follows:

(1) When the large RWIV of the cable occurs, the upper rivulet circumferentially oscillates on the cable surface. The oscillation is coherent along the entire cable and almost in-phase with the cable vibration.

(2) The excitation mechanism of the RWIV can be explained by the interaction between the cable, air boundary layer, and the upper rivulet. When the cable vibrates upward, the oscillating upper rivulet induces the boundary layer to attach on the upper side of cable, which generates upward aerodynamic force to excite the cable. The cable's vibration, in turn, also harmonizes the upper rivulet oscillation on the cable surface by changing the attacking angle and the inertial force.

CHAPTER EIGHT

NUMERICAL MODEL OF RWIV BASED ON THE NEW

EXCITATION MECHANISM

8.1 Introduction

In previous chapters, the upper rivulet's development and movement during the RWIV have been investigated in a wind tunnel. The relationship between the cable vibration and the upper rivulet has been studied. The variation of the upper rivulet indicates that the upper rivulet modifies the air boundary layer state when the cable moves upward. Based on these, a new excitation mechanism of the RWIV has been proposed.

In this chapter, a numerical model of the aerodynamic forces acting on the cable during the RWIV is established based on the proposed excitation mechanism. Two sets of aerodynamic force coefficients are adopted to simulate the RWIV using the proposed numerical model. Parametric studies are conducted to investigate the effects of different factors on the RWIV. Besides, an energy-based method is introduced to directly estimate the steady amplitude of the RWIV. The cable is assumed to vibrate at different amplitude and the input energy of the vibration system is calculated. The steady amplitude of the cable vibration is solved by setting the input energy equals to zero.

8.2 Numerical Models

An inclined cable suffering yawed wind is taken into consideration. The wind speed and direction are defined in Figure 6-1. The cable is simplified as a rigid cylinder.

A numerical model is established based on the following assumptions:

(1) The upper rivulet contributes to the RWIV, while the lower one has no effect on the RWIV.

(2) The upper rivulet circumferentially vibrates on the cable surface in-phase with the cable vibration during the RWIV.

(3) The amplitude of the upper rivulet vibration is proportional to the cable amplitude under a given wind speed. That is, their amplitude ratio is constant.

(4) The initial position of the upper rivulet depends on the wind speed, which is obtained through wind tunnel testing.

(5) The mass of the rivulet is negligible compared with that of the cable.

(6) The upper rivulet changes the loading on the cable by modifying the boundary layer state when the rivulet is oscillating on the cable surface.

(7) Compared with the cable length, the in-plane cable vibration is relatively small and the out-of-plane vibration is negligible.

(8) Only single mode vibration is considered and the interaction between multi-modes is ignored.

Most of the assumptions are the same as those described in Chapter Six except Item 6. In Chapter Six, the aerodynamic forces are based on quasi-steady assumption that the upper rivulet changes the aerodynamic forces by changing the aerodynamic

configuration of the cable when the upper rivulet is oscillating on the cable surface. However, in the new excitation mechanism, the upper rivulet changes the boundary layer state, generating the excitation aerodynamic forces acting on the cable surface.

8.2.1 Motions of the Cable and Rivulet

In wind tunnel tests, the cable only vibrates in the vertical direction normal to the cable axis and the upper rivulet circumferentially oscillates on the cable surface. Therefore, in the numerical model, both the horizontal and longitudinal vibrations of the cable are ignored. The cable displacement and the rivulet position are defined similarly as shown in Figure 6-2. The downward and normal to the cable axis vibration is set as positive. The rivulet's position is defined as the angle measuring from the cable top in anti-clockwise direction. The governing equation of the cable vibration is

$$\ddot{y} + 2\xi_s \omega \dot{y} + \omega^2 y = F_v / m \qquad (8\text{-}1)$$

where F_v is the sum of the vertical components of the aerodynamic forces and expressed as:

$$F_v = -(F_l \cos \varphi' + F_d \sin \varphi') \qquad (8\text{-}2)$$

The governing equation is the same as the quasi-steady model described in Chapter Six, whereas the aerodynamic forces acting on the cable are different.

8.2.2 Aerodynamic Force

In the quasi-steady model, the aerodynamic forces acting on the cable only depend on the location of the upper rivulet, while it depends on the air boundary layer state (Zdravkovich 1997) in the present model. As described in the previous chapter, the air boundary layer, upper rivulet, and cable vibration are coupled together during the RWIV. The oscillating upper rivulet induces the boundary layer to attach on the upper side of the cable when the cable is ascending, which generates the excitation aerodynamic forces on the cable.

Consentino et al. (2003b) has presented a formula of the aerodynamic forces considering the air boundary layer attachment induced by the upper rivulet:

$$
\begin{aligned}
F_d &= \frac{1}{2}\rho U_{rel}^2 D C_d \\
F_l &= \frac{1}{2}\rho U_{rel}^2 D C_{L,\max}\Psi
\end{aligned}
\tag{8-3}
$$

where the lift force depends on the maximal lift force coefficient $C_{L,\max}$ and the occurrence function Ψ. The latter is defined as

$$
\Psi = \left[0.5 + 0.45\operatorname{atan}(\frac{R\dot{\theta}}{2\times10^{-3}}\times\frac{\pi}{180})\right]\times\exp\left[-(\frac{\theta_s-90°}{10°})^2\right]\times\exp\left[-(\frac{\beta^*}{40°})^4\right]\times\exp\left[-\frac{\ln(\mathrm{Re}_N/10^5)}{0.2}\right]
$$

$$
\tag{8-4}
$$

$C_{L,\max}$ is the lift force coefficient when the strongest air boundary attachment occurs, corresponding to $\Psi=1$. Ψ $(0\leq\Psi\leq1)$ indicates the occurrence possibility or the

intensity of the boundary layer attachment, which depends on four parameters: the

upper rivulet velocity ($R\dot{\theta} = Rc_\theta \dot{y}$) and position from the stagnation point (θ_s),

effective yaw angle (β^*), and the Reynolds number using the wind speed normal to

the cable ($R_{e,N} = U_0 \cos \beta^* / \upsilon$). The second item of the right hand side Equation (8-4)

indicates that the attachment of the air boundary layer occurs when the upper rivulet

is located close to the separation angle (90°). That is, when θ_s is close to 90,

$\exp\left[-(\dfrac{\theta_s - 90°}{10°})^2\right]$ is close to 1. The third item describes the effect of the relative

yaw angle on the attachment of the air boundary layer, which was fitted using the

data reported by Bursnal and Loftin (1951). The last item represents the influence of

the relative Reynold number, which was fitted using the full scale observation data.

However, the experimental results of the present study showed that the on-set

condition of the occurrence of the RWIV is the formation and circumferential

vibration of the upper rivulet. The reason of the cable vibration is the air boundary

layer attachment induced by the upper rivulet. Furthermore, the air boundary layer

attachment only occurs when the cable is ascending and the upper rivulet is

synchronously moving clockwise. The vibration of the upper rivulet plays the most

important role in the RWIV. Consequently, in the present study, Equation (8-4) is

modified as the following equation.

$$\Psi^* = c_u \times \left[0.5 + \mathrm{atan}(\frac{2\pi R\dot{\theta}}{U_N})/\pi\right] \times \exp\left[-(\frac{\beta^* - 30°}{22°})^4\right] \times \exp\left[-\frac{\ln(c_r/90)}{0.3}\right] \qquad (8\text{-}5)$$

where

$$c_r = \frac{U_N^2}{Dg\cos\alpha} \qquad (8\text{-}6)$$

and c_u ($0 \le c_u \le 1$) is the uniform coefficient denoting the coherence of the boundary layer attachment along the cable. When the attachment is ideally uniform along the cable, c_u equals to 1; when the attachment is completely chaotic along the cable, c_u equals to 0. c_r ($0 \le c_u \le 1$) denotes the possibility of the upper rivulet's formation and g is the gravitational acceleration. It indicates the influence of the wind speed and the cable diameter on the formation of the upper rivulet. Equation (8-6) is derived in Appendix A. The two constants '90' and '0.3' are employed such that the RWIV starts at the wind speed of 8.5 m/s and the largest vibration occurs under the wind speed of 13.0 m/s. That is, when $U = 8.5$ m/s, $c_r = 41.5$, $\exp\left[-\frac{\ln(c_r/90)}{0.3}\right] = 0.14$ and when $U = 13.0$ m/s, $c_r = 97.0$, $\exp\left[-\frac{\ln(c_r/90)}{0.3}\right] = 0.98$.

The rivulet velocity of Equations (8-4) and (8-5) is expressed in terms of the cable velocity because the upper rivulet oscillates in-phase with the cable and the amplitude ratio (c_θ) is constant, as described in Chapter Six. The rivulet velocity of the first item of the right hand side of Equation (8-4) is non-dimensionalized by dividing the normal component of the incoming wind speed. The second item the right hand side of Equation (8-4) has been removed because the relative position of the upper rivulet has little effect on the attachment of the air boundary layer. The

initial position of the upper rivulet is adaptive within the wind speed range of the RWIV. It automatically moves to the position around the separation point, not always close to 90° but varying with the wind speed.

The third item of the right hand side of Equation (8-4) has been modified based on the field observations by Ni et al. (2007) and Scott Phelan et al. (2006). They reported that most cable vibration occurred when β^* ranged between 10° and 50° and the largest vibration occurred when the effective yaw angle was approximately 30°. The constant '22' are employed such that when $\beta^* = 10°$ or 50°,

$$\exp\left[-(\frac{\beta^* - 30°}{22°})^4\right] = 0.50.$$

Once the aerodynamic force coefficients are obtained, Equations (8-2), (8-3), and (8-5) to (8-6) are substituted into Equation (8-1). The cable responses can be calculated by solving the equation. Two different sets of force coefficients are used to simulate the RWIV, which are referred to Case 1 and Case 2, respectively.

(a) Case 1

In this case, the aerodynamic force coefficients suggested by Consentino et al. (2003b) are used. That is

$$\begin{aligned} C_d &= 1.0 \\ C_l &= C_{L,\max} \Psi^* \\ C_{L,\max} &= 0.8 \end{aligned} \tag{8-7}$$

The force coefficients were estimated from the wind tunnel testing results and have

been used to calculate the cable responses by Consentino et al. (2003b).

(b) Case 2

In the case, the aerodynamic force coefficients measured by Jakobsen et al. (2012) are used. In their test, both the external diameter ($D = 160$ mm) and the effective yaw angle ($\beta^* = 30°$) of the inclined cable are similar to the present wind tunnel test. They measured the pressure distribution of a stationary inclined cable in the critical Reynolds number range. The aerodynamic forces were calculated by integrating the wind pressure acting on the cable surface. The drag and lift coefficients were respectively calculated as 0.84 and 0 in the pre-critical Reynolds number range, and 0.48 and 0.68 in the one-bubble range. In the pre-critical Reynolds number range, there is no reattachment occurred in the air boundary layer. In the one-bubble range, the flow state has the strongest reattachment of the air boundary layer.

When the upper rivulet perfectly induces the air boundary layer to attach, the aerodynamic forces coefficients are the same as that in the one-bubble range. When the upper rivulet does not induce the air boundary layer to attach, the aerodynamic forces coefficients are the same as that in the pre-critical range. Therefore, they are expressed as:

$$
\begin{aligned}
C_d &= 0.84 - (0.84 - 0.48)\Psi^* \\
C_l &= C_{L,\max}\,\Psi^* \\
C_{L,\max} &= 0.68
\end{aligned}
\tag{8-8}
$$

For both cases, the aerodynamic forces on the cable surface are calculated from

Equation (8-3) and the substituted into Equation (8-1) to calculate the cable responses.

8.3 Numerical Results

Numerical analysis is carried out using the cable model tested in the wind tunnel as described in Chapter Three. The properties of the cable model are assumed: external diameter D = 160 mm, cable mass per unit length m = 33.0 kg/m, in-plane fundamental frequency f_y = 1.39 Hz, damping ratio ξ_s = 0.17%, inclination angle α = 32°, and yaw angle β = 35°.

The uniform coefficient (c_u) is complicated and difficult to calibrate. In the present study, it is estimated from the distribution of the upper rivulet during the RWIV as:

$$c_u = \exp\left[-avg\left(\frac{\sum\limits_{j=1}^{n}\left|\theta_{i,j} - \hat{\theta}_i\right|}{n\,\overline{\theta}} \right) \right] \tag{8-9}$$

where, $\overline{\theta}$ is the amplitude of the averaged upper rivulet angle along the cable axis, $\theta_{i,j}$ denotes the upper rivulet angle at the i-th time step and the j-th longitudinal section from the reference section as shown in Figure 4-12, n is the total sections of the entire testing segment, and $\hat{\theta}_i$ represents the averaged upper rivulet angle at the i-th time step. When the upper rivulet is uniform along the cable axis ($\theta_{i,j} = \hat{\theta}_i$),

$$avg\left(\frac{\sum_{j=1}^{n}\left|\theta_{i,j}-\hat{\theta}_i\right|}{n\,\overline{\theta}}\right)=0,\text{ and } c_u = 1.0,\text{ when the upper rivulet is extremely chaos along}$$

the cable axis, $avg\left(\dfrac{\sum_{j=1}^{n}\left|\theta_{i,j}-\hat{\theta}_i\right|}{n\,\overline{\theta}}\right)\to\infty$, and $c_u = 0$. Finally, c_u is calculated as 0.75

using the data of Chapter Seven ($\overline{\theta}=13°$, $n=50$).

The cable's initial displacement and velocity are set to 1 mm and 0 m/s, respectively. The cable responses are then calculated from Equation (8-1) using the Runge-Kutta integration method. Figure 8-1 compares the calculated amplitudes of the cable vibration and the experimental ones. The detail of the wind tunnel tests please refers to Chapter Three.
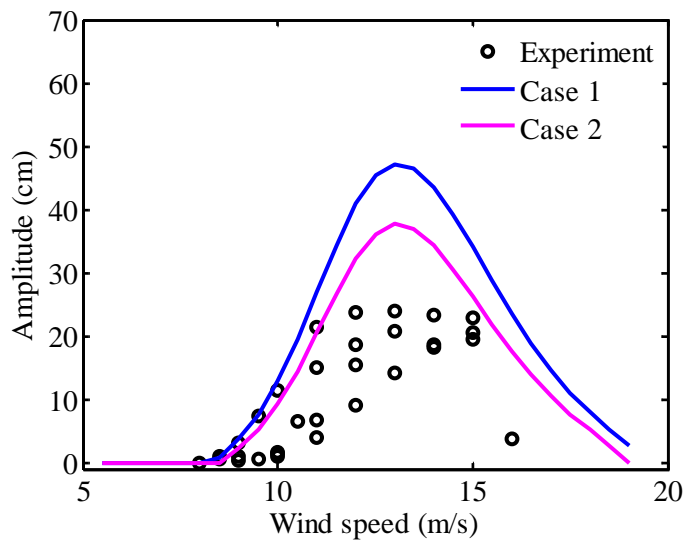
Figure 8-1. Cable displacement versus wind speed

The numerical results show that the large cable vibration occurs when the wind speed is between 8.5 m/s and 19.0 m/s. The amplitude of the cable displacement first

increases, reaches the maximum at U = 13.0 m/s, and then decreases with the increase of the wind speed. The calculated wind speed range of the occurrence of the RWIV agrees well with the wind tunnel testing results. The maximum displacements of the numerical results are larger than the wind tunnel testing results. The difference between the numerical and the wind tunnel testing results might be caused by the ideal assumptions and the constraint of the maximal displacement in the wind tunnel test. The numerical analyses are conducted under the ideal condition that the upper rivulet and the cable vibrations are perfectly coupled, which indicates that the air boundary layer perfectly attaches on the upper side of the cable during the RWIV. However, in the wind tunnel testing, the upper rivulet could not perfectly induce the air boundary layer attachment and there is a more or less phase difference between the upper rivulet and cable vibrations, which significantly reduces the cable vibration amplitude as described in Chapter Five. Therefore, the numerical results overestimate the maximum amplitude of the RWIV.

Figure 8-2 shows a typical time history of the cable displacement calculated from Case 2. During the excitation phase (0 to 200s), the cable vibration keeps growing until the amplitude becomes steady. This cable vibration is very close to a harmonic vibration. The vibration frequency is equal to the fundamental frequency of the cable.
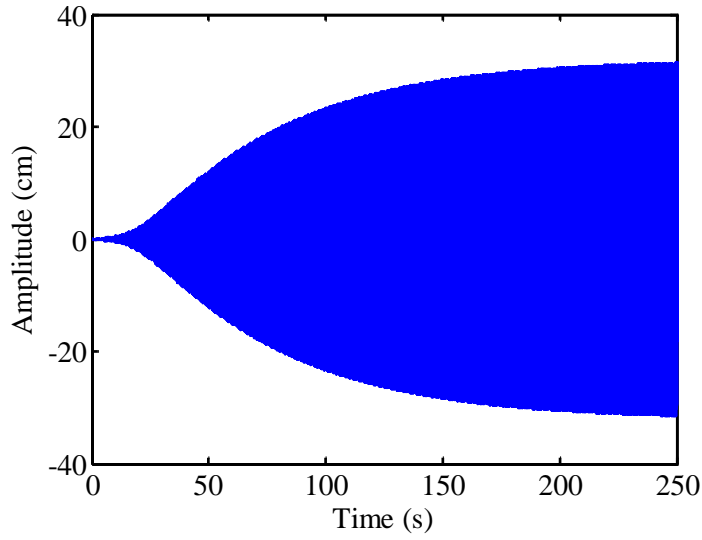
(a)
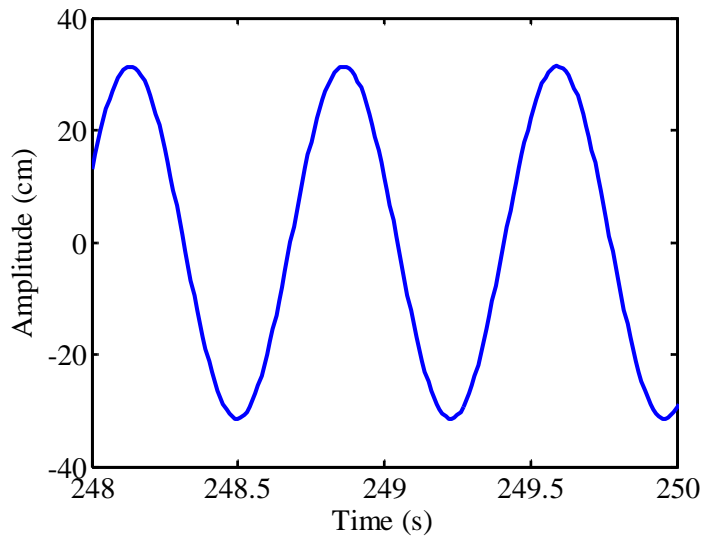
(b)

Figure 8-2. Numerical responses during the excitation phase: $U = 12.0$ m/s

8.4 Parametric Study

In this section, parametric studies are conducted using Case 2 as the basic model, in which the non-uniformity of the air boundary layer attachment along the longitudinal

direction is not considered ($c_u = 1.0$). The effects of different parameters such as the wind speed, yaw angle, phase difference between the rivulet and cable vibration, structural damping ratio, and uniform coefficient on the RWIV are investigated using the proposed numerical model.

8.4.1 Effects of the Yaw Angle and the Wind Speed

The effects of the yaw angle and wind speed on the RWIV are shown in Figure 8-3. The most unfavorable cable vibration occurs within the yaw angle range of 25° to 55°, in which the wind speed range of the occurrence of the RWIV increases as the yaw angle increases. This agrees with the wind tunnel tests (Cosentino 2003a) and the field observations by Zuo et al. (2008) and Zuo and Jones (2010).
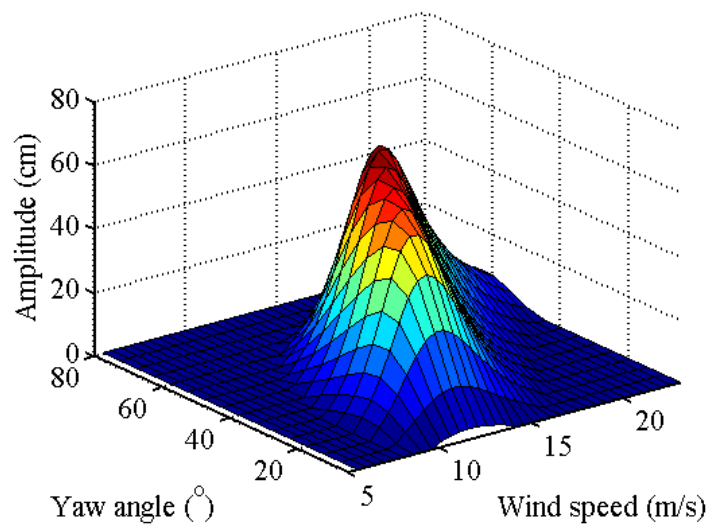
Figure 8-3. Cable amplitude under different yaw angle and wind speed

8.4.2 Effects of the Phase Difference between the Upper Rivulet and the Cable Vibration

Both the experimental and numerical results show that the cable exhibits a harmonic vibration when the vibration reaches a steady state. Therefore, the cable displacement and velocity can be expressed as

$$y = Y \sin \omega t$$
$$\dot{y} = \omega Y \cos \omega t$$

$$(8\text{-}10)$$

where Y is the amplitude of the cable displacement, and ω is the circular frequency of the cable.

If there is a phase difference between the upper rivulet and cable vibrations and the phase difference is positive when the upper rivulet vibrates ahead of the cable, the rivulet position and velocity can be expressed as:

$$\theta = c_\theta y = c_\theta Y \sin(\omega t + \phi) = c_\theta (y \cos \phi + \frac{1}{\omega} \dot{y} \sin \phi)$$
$$\dot{\theta} = c_\theta \dot{y} = c_\theta Y \omega \cos(\omega t + \phi) = c_\theta (\dot{y} \cos \phi - \omega y \sin \phi)$$

$$(8\text{-}11)$$

where ϕ is the phase difference between the upper rivulet and cable vibrations.

Substituting Equations (8-11) and (8-5) into Equation (8-1) and solving the equation, the cable responses can be calculated under different phase difference and wind speeds. The results are shown in Figure 8-4.
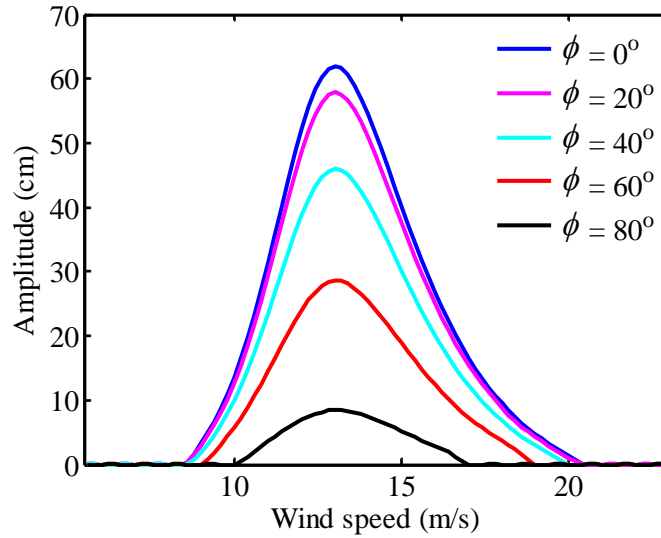
Figure 8-4. Cable amplitude versus the wind speed under different phase difference

The results show that the phase difference has a significant effect on the cable vibration amplitude and the wind speed range of the occurrence of the RWIV. The cable vibration amplitude decreases with the increase of the phase difference, and the decrement is more rapid when the phase difference becomes larger, which is in a good agreement with the observation of wind tunnel tests as described in Chapter Five. The maximal vibration amplitude decreases by 86% when the phase difference reaches 80°. The on-set wind speed increases with the increase of phase difference. The wind speed range of the occurrence of the RWIV becomes narrow as the phase difference increases. In particular, when there is no phase difference, the RWIV occurs within the wind speed of 9.0 to 20.0 m/s, while the wind speed turns to 10.5 to 16.5 m/s when the phase difference reaches 80°.

It is worth to note that, the phase difference should also have influence on the amplitude ratio (c_θ) because the rivulet position is affected by the cable velocity (changing attacking angle) and acceleration (inertial force). However, this influence

has been ignored in the present study. The amplitude ratio is set to be constant as 0.71 °/cm.

8.4.3 Effect of the Cable Diameter

The effect of the cable diameter on the amplitude of the RWIV is investigated by changing parameter D in Equations (8-3) and (8-6). Five cases are calculated when the cable diameter increases from 120 mm to 200 mm with the increment of 20 mm. For comparison, the calculated cable displacement is divided by the cable diameter. Figure 8-5 shows the calculated non-dimensional cable amplitude versus the wind speed for different cable diameters.
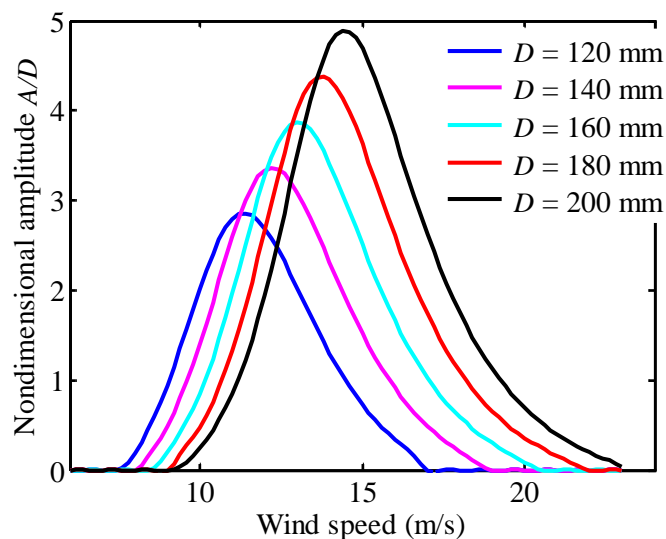
Figure 8-5. Non-dimensional cable amplitude versus the wind speed for different cable diameters

The results show that both the onset wind speed and the wind speed range of the occurrence of the RWIV increase as the cable diameter increases. The maximal non-dimensional amplitude and the corresponding wind speed also increase with the

increase of the cable diameter. For example, the maximal non-dimensional amplitude is approximate 2.8 under the wind speed of 11.5 m/s for the cable with the diameter of 120 mm, while it turns to 4.9 under the wind speed of 14.5 m/s when the cable diameter increases to 200 mm. The on-set wind speed increases from 8.0 m/s to 9.8 m/s when the cable diameter enlarges from 120 mm to 200 mm. The tendency that the on-set wind speed of the RWIV increases with the increase of the cable diameter is clearly revealed from c_r in Equation (8-6). When the cable diameter increases, the wind speed has to increase to overcome the tangential component of the gravity. The reason for the maximal amplitude increasing for the larger cable diameter is because the corresponding wind speed increases and the aerodynamic excitation forces are proportional to the square of the wind speed while the aerodynamic damping is proportional to the wind speed.

8.4.5 Effect of the Structural Damping Ratio

The effect of the structural damping ratio on the RWIV is investigated by changing ξ_s in Equation (8-1). The cable responses are calculated when the damping ratio increase from 0.17% to 0.51%. The results are shown in Figure 8-6. It is obvious that the damping ratio affects not only the cable amplitude but also the wind speed range of the occurrence of the RWIV. The maximal cable amplitude decreased from 62.0 cm to 20.0 cm when the damping ratio increases from 0.17% to 0.51%. In particular, the cable amplitude is more sensitive when the damping ratio is relatively small. The wind speed range of the occurrence of the RWIV also slightly narrows when the damping ratio increases. The tendency coincides with the wind tunnel results observed in Chapter Three.
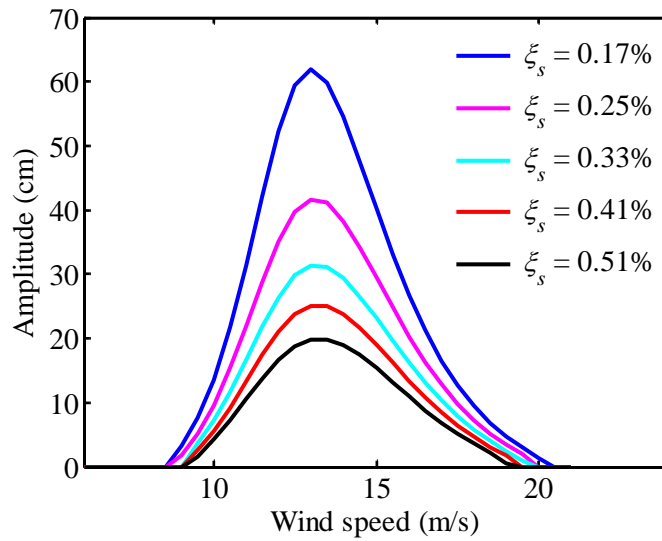
Figure 8-6. Cable amplitude versus the wind speed for different damping ratios

8.4.6 Effect of Uniform Coefficient

The effect of the uniform coefficient on the RWIV is investigated by changing c_u in Equation (8-5). The calculated results are shown in Figure 8-7. It shows that c_u significantly affects the cable amplitude and the wind speed range of the occurrence of the RWIV. The cable amplitude decreases by 90.3% when c_u reduces from 1.0 to 0.2. The wind speed range of the RWIV is from 9.0 to 20 m/s when $c_u = 1.0$, and turns to 10.5 to 16.5 m/s when $c_u = 0.2$. These results agree with the wind tunnel tests of Chapter Four that the uniform upper rivulet results in a larger cable vibration.
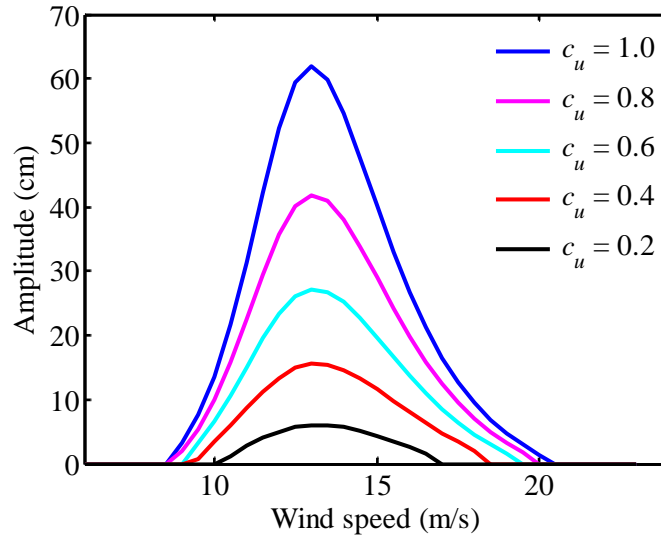
Figure 8-7. Cable amplitude versus the wind speed for different uniform coefficients

8.5 Estimation of the steady amplitude of the RWIV Using an Energy-Based Method

In previous section, the time history of the cable vibration was calculated using the numerical integration method, which is time-consuming. In this section, an energy-based method is proposed to directly estimate the steady amplitude of the RWIV.

During one cycle, the aerodynamic work attributed to the aerodynamic force can be calculated as

$$E_a = \int_0^T F_v \dot{y} dt \qquad (8\text{-}12)$$

where T is the period of the cable vibration.

Substituting Equations (8-2) and (8-3) into Equation (8-12) and separating the lift and drag components, one has

$$E_a = -\frac{1}{2}\rho\int_0^T U_{rel}^2 DC_{L,\max}\Psi^* \cos\varphi'\dot{y}dt - \frac{1}{2}\rho\int_0^T U_{rel}^2 DC_D \sin\varphi'\dot{y}dt$$
$$= E_L + E_D$$

(8-13)

where E_L and E_D represent the work done by the lift and drag forces, respectively.

The cable model is can be treated as a linear single-degree-of-freedom vibration system and only the structural damping consumes energy, which can be calculated as the following equation

$$E_S = -\int_0^T 2m\xi_s \dot{y}^2 dt$$

(8-14)

The stability of the cable can be evaluated by the total work during the cycle, expressed as:

$$E = E_a + E_S$$

(8-15)

Depending on the value of the total work E, the cable vibration can be (1) stable ($E = 0$), (2) increasing ($E > 0$), or (3) decaying ($E < 0$).

Since the cable exhibit a harmonic vibration, the cable velocity in Equations (8-13)

and (8-14) is expressed as Equations (8-10).

The above procedure is applied to Case 2 to estimate the steady vibration amplitude of the RWIV. The non-uniformity of the upper rivulet along the cable axis is not considered ($c_u = 1.0$). Equations (8-5) and (8-8) are substituted into Equation (8-3), which is then substituted into Equations (8-13) and (8-14). For different amplitude Y, the total work is obtained from Equation (8-15). Finally, the steady amplitude of the cable is solved by setting $E = 0$.

Figure 8-8 shows the relation between the work and the vibration amplitude at the wind speed of 12.0 m/s. The structural damping and drag force do a negative work on the system, whereas the lift force does a positive work, all increase in magnitude as the cable vibration amplitude becomes larger. The total input energy (E) initially increases and subsequently decreases with the increase of the cable vibration amplitude. When the amplitude reaches approximately 52.0 cm, the total input energy equals zero, which means the cable vibration reaches a steady state at this amplitude. When the cable vibration amplitude is smaller than the steady amplitude, the positive work done by the lift force can overcome the negative work done by the structural damping and the drag force until the steady state is reached.
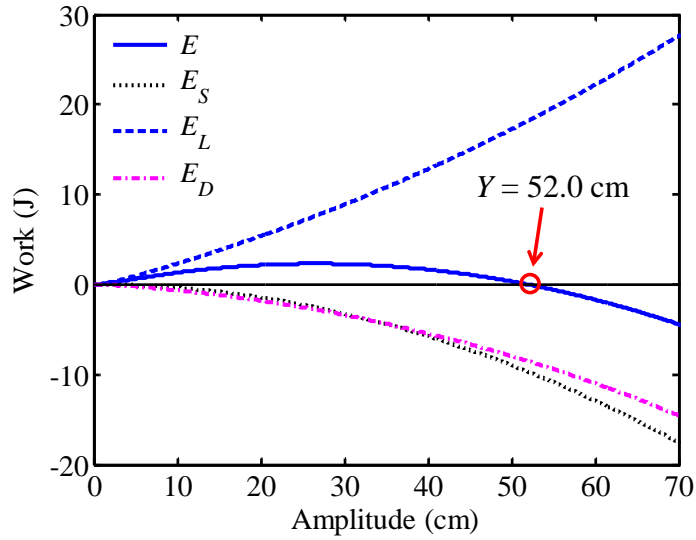
Figure 8-8. Works of the cable versus vibration amplitude (U = 12.0 m/s)

For other wind speeds, the procedures are repeated and the steady vibration amplitudes are shown in Figure 8-9, as compared with the results obtained using the numerical integration approach. Two approaches give consistent results, with the largest difference less than 1.0%.
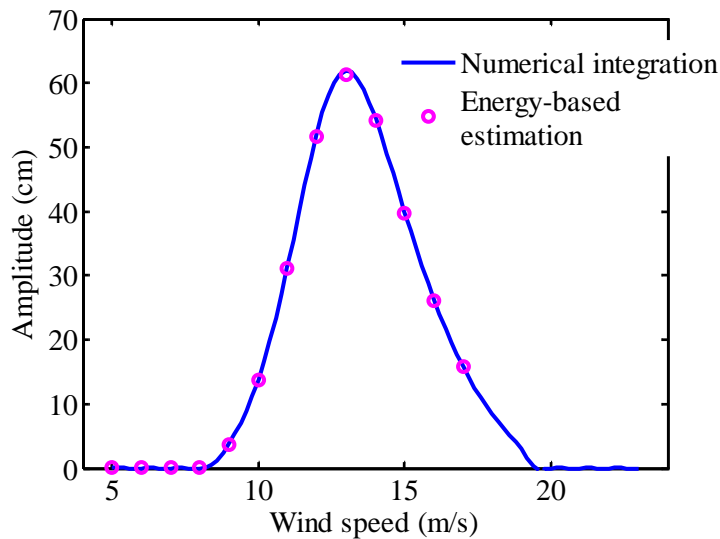
Figure 8-9. Cable vibration amplitude by numerical integration and energy-based approach

8.6 Summary

In this chapter, a numerical model of the aerodynamic forces acting on the cable during the RWIV was established based on the proposed excitation mechanism described in Chapter Seven. Two sets of aerodynamic force coefficients were adopted to calculate the cable responses using the proposed numerical model. The parametric studies have been conducted to investigate the effects of different parameters on the RWIV. The analytical results show that the numerical model is able to successfully capture the main features of the RWIV. A new energy-based method was proposed to estimate the steady amplitude of the RWIV. The main conclusions can be drawn as follows:

(1) The proposed numerical model is effective to simulate the RWIV. Similar results are obtained using the two sets of aerodynamic force coefficients measured by Cosentino et al. (2003b) and Jakobsen et al. (2012), respectively. The calculated RWIVs are velocity- and amplitude- restriction.

(2) Both the on-set wind speed and the wind speed range of the occurrence of the RWIV increase with the increasing yaw angle.

(3) The cable amplitude decreases as the increase of cable damping ratio and the phase difference between the upper rivulet and cable vibrations, coinciding with the wind tunnel results of Chapters Three and Five.

(4) Both the cable amplitude and the on-set wind speed of the RWIV increase when the cable diameter becomes larger.

(5) The uniform coefficient of the upper rivulet also has significant effects on the RWIV. A more uniform upper rivulet oscillation results in a larger cable vibration.

(6) The proposed energy-based method is effective to estimate the steady amplitude

of the RWIV. The largest difference between the numerical analysis and the energy-based estimation is less than 1.0%.

CHAPTER NINE

CONCLUSIONS AND FUTURE RESEARCH

9.1 Conclusions

Wind tunnel tests and numerical analysis have been conducted in this thesis to investigate the excitation mechanism of the RWIV. Large amplitude RWIVs were successfully reproduced in an open-jet wind tunnel and the water rivulets were simulated by guiding real water on the cable top using two plastic pipes. A digital image processing method is proposed to synchronously measure the upper rivulet's movement and thickness and the cable vibration. Using the proposed digital image processing method, the detailed information of the upper rivulet and its relationship with the cable vibration are obtained in the wind tunnel tests. Based on these measurements, a new excitation mechanism of the RWIV is then proposed and a numerical model of the aerodynamic force is established. Finally, the cable responses are calculated using the proposed numerical model to verify its effectiveness. Besides, the parametric studies are conducted to investigate the different factors such as the wind speed, yaw angle, phase gap between the rivulet and cable vibration, and structural damping ratio on the RWIV. The results and findings are summarized as follows:

(1) Guiding water lines using the plastic pipes is effective to reproduce RWIV in wind tunnel tests, similar to spraying real water. The most important on-set condition of the RWIV should be the wettability of the cable surface, which

allows the upper rivulet oscillating on the cable surface.

(2) The upper rivulet plays a critical role in the RWIV, while the lower rivulet has no effect on this phenomenon. The RWIV could occur within a wide range of flow rate. When the water rivulet has the moderate flow rate, corresponding to the moderate rainfall, the stay cable is more prone to large RWIV.

(3) The proposed digital image processing method is efficient and cost-effective to measure the movement and thickness of the upper rivulet along the entire cable. The upper rivulet oscillates circumferentially on the cable surface at the same frequency of the cable when the large RWIV occurs and the averaged upper rivulet position oscillates almost in-phase with the cable vibration.

(4) The thickness of the upper rivulet periodically varies when the rivulet oscillates on the cable surface. The upper rivulet becomes thickest when it reaches the farthest position away from the cable top and the cable simultaneously arrives at the lowest position.

(5) The circumferentially oscillating upper rivulet is strongly coupled with the cable vibration. The cable can vibrate steadily with different amplitudes under the same wind speed and rivulet flow rate. The oscillating upper rivulet significantly reduces the aerodynamic damping of the inclined cable system.

(6) When the cable is ascending, the upper rivulet induces the air boundary layer to attach on top side of the cable surface, which is the main reason of the large cable vibration. A new excitation mechanism of the RWIV is then proposed and explained by the interaction between the upper rivulet oscillation, air boundary layer attachment, and the cable vibration. The upper rivulet's variation and movement induce the air boundary layer to attach on the top side of cable, which generates significant lift aerodynamic forces to excite the cable when the

cable vibrates upward. The cable's vibration, in turn, harmonizes the upper rivulet by changing the attacking angles and the inertial force.

(7) A numerical model of the aerodynamic forces is proposed considering the air boundary layer attachment based on the new excitation mechanism. This model is effective to simulate the RWIV and the calculated RWIVs are velocity- and amplitude- restriction.

(8) The cable amplitude, on-set wind speed, and wind speed range of the occurrence of the RWIV are significantly affected by the wind speed, yaw angle, phase gap between the rivulet and cable vibration, and structural damping ratio.

9.2 Future Research

The proposed digital image processing method, excitation mechanism, and the numerical model of the aerodynamic forces of the RWIV can be further investigated in the following aspects:

(1) The proposed digital image processing method could not obtain the measurement results in real time. An online image processing method and system can be developed to realize the measurement of the upper rivulet and the cable vibration in real-time.

(2) The resolutions of the cable displacement and rivulet position measured by the camera are relatively small. It can be improved by using a high resolution camera.

(3) The directly experimental verification of the proposed excitation mechanism of the RWIV is required. The wind loads acting on the cable surface during the RWIV need to be measured using pressure taps or other facilities.

(4) The effect of the upper rivulet on the aerodynamic forces of a stationary cable is

important to explain the beginning of the RWIV. Wind tunnel tests should be carried out to measure the aerodynamic forces of the inclined cable when there is and without the upper rivulet.

(5) The proposed numerical model of the aerodynamic forces of the RWIV has not been experimentally verified. The parameters in this model need further careful calibration through wind tunnel tests.

(6) Besides, more studies should be conducted to compare the numerical results with the experimental results and verify the effectiveness of this model.

(7) The cable used is rigid, not flexible as the real stayed cables. Therefore the flexible cable model should be tested in a wind tunnel in the future. The rivulet vibration on the real stayed cable could be measured through field measurement.

POSSIBILTY OF THE FORMATION OF THE UPPER

RIVULET

Figure A-1 shows the sectional view of the cable with the upper rivulet and the forces acting on the upper rivulet. Only the aerodynamic forces and the gravity are considered in the formation of the upper rivulet, while the surface tension and coulomb friction between the air, rivulet, and cable are ignored.

<div align="center">
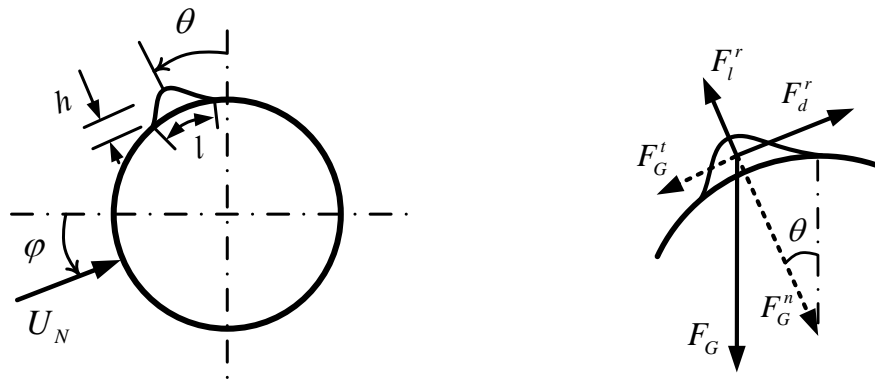
(a) Sectional view of the upper rivulet   (b) Forces acting on the upper rivulet

Figure A-1. Sectional view of the upper rivulet and forces

</div>

h and l in Figure A-1(a) are the thickness and width of the upper rivulet, respectively. θ and φ are defined the same as Chapter Four.

As Figure A-1(b) shows, the aerodynamic force of the upper rivulet can be decomposed into two components: (1) lift force F_l^r in the radial direction of the

cable; and (2) drag force F_d^r in the tangent direction. They are expressed as:

$$F_d^r = \frac{1}{2}\rho U_N^2 h C_d^r$$
$$F_l^r = \frac{1}{2}\rho U_N^2 h C_l^r$$

(A-1)

where C_d^r and C_l^r are the drag and lift force coefficients of the upper rivulet, respectively, which depends on the wind pressure distribution.

The gravity force of the upper rivulet is also decomposed into the tangent (F_G^t) and the radial (F_G^n) components, which are expressed as:

$$F_G^t = c_s \rho_w l h g \cos\alpha \sin\theta$$
$$F_G^n = c_s \rho_w l h g \cos\alpha \cos\theta$$

(A-2)

where c_s is the shape coefficient, defined as the ratio of the cross-sectional area to the product of the rivulet's width (l) and thickness (h). ρ_w is the water density.

The upper rivulet appears when the aerodynamic force acting on the upper rivulet overcomes the tangent component of the gravity. That is

$$\frac{1}{2}\rho U_N^2 h C_d^r \geq c_s \rho_w l h g \cos\alpha \sin\theta$$

(A-3)

The width (l) and thickness (h) of the upper rivulet can be expressed in terms of the

192

cable diameter as follows:

$$
\begin{aligned}
h &= \varepsilon_h D \\
l &= \varepsilon_l D
\end{aligned}
\tag{A-4}
$$

where ε_h and ε_l are the ratios of the rivulet's thickness and width to the cable diameter.

Substituting Equation (A-4) into (A-3), a new criterion of the formation of the upper rivulet is derived as:

$$
\frac{U_N^2}{Dg \cos \alpha} \geq \frac{2c_s \varepsilon_l \rho_w \sin \theta}{\rho C_d^r}
\tag{A-5}
$$

In this formula, parameters c_s, ε_l, θ, and C_d^r depend on the wind pressure around the cable and upper rivulet, which depends on the state of the air boundary layer. However, when the RWIV occur, the distribution of the wind pressure should be invariant and the parameters C_d^r, c_s, θ, ε_h and ε_l can be treated as constant in Equation A-5. In this regard parameter c_r is defined as $\dfrac{U_N^2}{Dg \cos \alpha}$.

REFERENCES

Alam, MD., Zhou, Y., 2007. Turbulent wake of an inclined cylinder with water running. Journal of Fluid Mechanism 589, 261–303.

Bi, J.H., Lu, P., Wang, J., Bao, C., Guan, J., 2014. Numerical simulation and analysis of the effects of water-film morphological changes on the aerodynamic lift of stay cables. Journal of Fluids and Structures 48, 376–392.

Bi, J.H., Wang, J., Shao, Q., Lu, P., Guan, J., Li, Q.B., 2013. 2D numerical analysis on evolution of water film and cable vibration response subject to wind and rain. Journal of Wind Engineering and Industrial Aerodynamics 121, 49–59.

Bosdogianni, A., Olivari, D., 1996. Wind- and rain-induced oscillations of cables of stayed bridges. Journal of Wind Engineering and Industrial Aerodynamics 64, 171–185.

Boujard, O., 2007. Etude du Phénomène de Galop des Câbles Inclinés Secs Appliquée Aux Hhaubans de Ponts, Application au Pont de l'Iroise, PhD Thesis, University of Nantes, France.

Cao, D.Q., Tucker, R.W., Wang, C., 2003. A stochastic approach to cable dynamics with moving rivulets. Journal of Sound and Vibration 268, 291–304.

Chabart, O., Lilien, J.L., 1998. Galloping of electrical lines in wind tunnel facilities. Journal of Wind Engineering and Industrial Aerodynamics 74-76, 967–976.

Chen, W.L., Tang, S.R., Li, H., Hu, H., 2013. Influence of dynamic properties and position of

rivulet on rain-wind-induced vibration of stay cables. Journal of Bridge Engineering 18, 1021–1031.

Cheng, P., Li, H., Fuster, D., Chen, W.L., Zaleski, S., 2015. Multi-scale simulation of rainwater morphology evolution on a cylinder subjected to wind. Computers & Fluids 123, 112–121.

Cheng, S., Larose, G.L., Savage, M.G., Tanaka, H., 2003. Aerodynamic behaviour of an inclined circular cylinder. Wind and Structures 6(3), 197–208.

Cheng, S., Guy, L.L., Mike, G.S., Hiroshi, T., Irwin, P.A., 2008. Experimental study on the wind-induced vibration of a dry inclined cable-Part I: Phenomena. Journal of Wind Engineering and Industrial Aerodynamics 96, 2231–2253.

Choi, H.S., Cheung, J.H., Kim, S.H., Ahn, J.H., 2011. Structural dynamic displacement vision system using digital image processing. NDT & E International 44, 597–608.

Cooper, K.R., 1985. A Note on the Wind-Induced Vibrations of Bundled Bridge Stay Cables, National Research Council of Canada, Note provided to RWDI.

Cosentino, N., Flamand, O., Ceccoli, C., 2003a. Rain−wind-induced vibration of inclined stay cables, Part I: experimental investigation and physical explanation. Wind and Structures 6, 471–484.

Cosentino, N., Flamand, O. and Ceccoli, C., 2003b, Rain−wind-induced vibration of inclined stay cables. Part II: Mechanical modeling and parameter characterization. Wind and Structures 6, 485–498.

Devenport, W.J., 2003. Flow Past a Circular Cylinder, Virginia Tech University, Online 9 Oct. 2003, Available: www.aoe.vt.edu.

Du, X.Q., Gu, M., Chen, S.R., 2013. Aerodynamic characteristics of an inclined and yawed circular cylinder with artificial rivulet. Journal of Fluids and Structures 43, 64–82.

FHWA, 2007. Wind-Induced Vibration of Stay Cables, Report of Federal Highway Administration, FHWA-HRT-05-083.

Flamand O., 1995. Rain–wind-induced vibration of cables. Journal of Wind Engineering and Industrial Aerodynamics 57, 353–362.

Flamand, O., Boujard, O., 2009. A comparison between dry cylinder galloping and rain–wind-induced excitation. 5th European & African Conference on Wind Engineering, Florence, Italy.

Fujino, Y., Warnitchai, P., Pacheco, B.M., 1993. An experimental and analytical study of autoparametric resonance in a 3DOF model of cable-stayed-beam. Nonlinear Dynamics 4, 111–138.

Geurts, C., Vrouwenvelder, T., van Staalduinen, P., Reusink, J., 1998. Numerical modeling of RWIV: Erasmus Bridge. Structural Engineering – An International 8, 9–135.

Gu, M., 2009. On wind–rain-induced vibration of cables of cable-stayed bridges based on quasi-steady assumption. Journal of Wind Engineering and Industrial Aerodynamics 97, 381–391.

Gu, M., Du, X.Q., 2005. Experimental investigation of rain–wind-induced vibration of

cables in cable-stayed bridges and its mitigation. Journal of Wind Engineering and Industrial Aerodynamics 93, 79–95.

Gu, M., Huang, L., 2008. Theoretical and experimental studies on the aerodynamic instability of a two-dimensional circular cylinder with a moving attachment. Journal of Fluids and Structures 24, 200–211.

Gu, M., Liu, C.J., Xu, Y.L., Xiang, H.F., (2002). Response characteristics of wind excited cables with artificial rivulet. Applied Mathematics and Mechanics 23(10), 1176–1187.

Hikami, Y., Shiraishi, N., 1988. Rain−wind-induced vibrations of cables stayed bridges. Journal of Wind Engineering and Industrial Aerodynamics 29, 408–418.

Hu, J., Yan, B., Zhou, S., Zhang, H.Y., 2012. Numerical investigation on galloping of iced quad bundle conductors. IEEE Transactions on Power Delivery 27(2), 784–792.

Irwin, P.A., 1997. Wind vibrations of cables on cable-stayed bridges. Proceedings of Structural Congress XV, Portland, OR, 383–387.

Jakobsen, J.B., Andersen, T.L., Macdonald, J.H.G., Nikitas, N., Larose, G.L., Savage, M.G., McAuliffe, B.R., 2012. Wind-induced response and excitation characteristics of an inclined cable model in the critical Reynolds number range. Journal of Wind Engineering and Industrial Aerodynamics 110, 100–112.

Kleissl, K., Georgakis, C.T., 2012. Comparison of the aerodynamics of bridge cables with helical fillets and a pattern-indented surface. Journal of Wind Engineering and Industrial Aerodynamics 104–106, 166–175.

Larose, G.L., Savage, M.G., Jakobsen, J.B., 2003. Wind tunnel experiments on an inclined and yawed circular cylinder in the critical Reynolds number range. Proceedings of 11th International Conference on Wind Engineering, Lubbock, Texas, USA.

Lee, J.J., Shinozuka, M., 2006. Real-time displacement measurement of a flexible bridge using digital image processing techniques. Experimental Mechanics 46, 105–114.

Lemaitre, C., de Langre, E., Hémon, P., 2010. Rainwater rivulets running on a stay cable subject to wind. European Journal of Mechanics - B/Fluids 29(4), 251–258.

Lemaitre, C., Hémon, P., de Langre, E., 2007. Thin water film around a cable subject to wind. Journal of Wind Engineering and Industrial Aerodynamics 95, 1259–1271.

Li, F.C., Chen, W.L., Li, H., Zhang, R., 2010a. An ultrasonic transmission thickness measurement system for study of water rivulets characteristics of stay cables suffering from wind–rain-induced vibration. Sensors and Actuators A: Physical 159, 12–23.

Li, H., Chen, W.L., Xu, F., Li, F.C., Ou, J.P., 2010b. A numerical and experimental hybrid approach for the investigation of aerodynamic forces on stay cables suffering from RWIV. Journal of Fluids and Structures 26, 1195–1215.

Li, Y.L., Wu, M.X., Chen, X.Z., Wang, T., Liao, H.L., 2013. Wind tunnel study of wake galloping of parallel cables on cable-stayed bridges and its suppression. Wind and Structures 16(3), 249–261.

Li, Y.L., Xu, Y.L., Xiang, H.Y., Chen, B., Shum, K.M., Liao, H.L., 2015. Analysis of rain-wind induced cable vibration using spatially measured aerodynamic coefficients. Advances in Structural Engineering 17(7), 961–977.

Macdonald, J.H.G., Larose, G.L., 2006. A unified approach to aerodynamic damping and drag/lift instabilities, and its application to dry inclined cable galloping, J. Fluid Struct. 22, 229–252.

McComber, P., Paradis, A., 1998. A cable galloping model for thin ice accretions, Atmospheric Research 46, 13–25.

Main, J.A., Jones, N.P., 1999a. Full-scale measurements of stay cable vibration. Proceedings of the 10th International Conference on Wind Engineering, 963–970.

Main, J.A., Jones, N.P., 2000. A comparison of full-scale measurements of stay cable vibration. Advanced Technology in Structural Engineering, 1–8.

Main, J.A., Jones, N.P., Yamaguchi, H., 2001. Characterization of rain–wind-induced stay–cable vibrations from full-scale measurements. In: Proceedings of the Fourth International Symposium on Cable Dynamics, Montreal, Canada, 235–242.

Matsumoto, M., Daito, Y., Kanamura, T., Shigemura, Y., Sakuma, S., Ishizaki, H., 1998. Wind-induced vibration of cables of cable-stayed bridges. Journal of Wind Engineering and Industrial Aerodynamics 74–76, 1015–1027.

Matsumoto, M., Saitoh, T., Kitazawa, M., Shirato, H., Nishizaki, T., 1995. Response characteristics of rain–wind-induced vibrations of stay-cables of cable-stayed bridges. Journal of Wind Engineering and Industrial Aerodynamics 57, 323–333.

Matsumoto, M., Shiraishi, N., Kitazawa, M., Knisely, C., Shirato, H., Kim, Y., Tsujii, M., 1990. Aerodynamic behavior of inclined circular cylinders-cable aerodynamics. Journal of Wind Engineering and Industrial Aerodynamics 33(1–2), 63–72.

Matsumoto, M., Shiraishi, N., Shirato, H., 1992. Rain–wind-induced vibration of cables of cable–stayed bridges. Journal of Wind Engineering and Industrial Aerodynamics 43, 2011–2022.

Matsumoto, M., Shirato, H., Yagi, T., Goto, M., Sakai, S., Ohya, J., 2003a. Field observation of the full-scale wind-induced cable vibration. Journal of Wind Engineering and Industrial Aerodynamics 91(1–2), 13–26.

Matsumoto, M., Yagi, T., Goto, M., Sakai, S., 2003b. Rain–wind-induced vibration of inclined cables at limited high reduced wind velocity region. Journal of Wind Engineering and Industrial Aerodynamics 91, 1–12.

Matsumoto, M., Yagi, T., Sakai, S., Ohya, J., Okada, T., 2005. Steady wind force coefficients of inclined stay cables with water rivulet and their application to aerodynamics. Wind and Structures 8, 107–120.

Matsumoto, M., Yagi, T., Shigemura, Y., Tsushima, D., 2001. Vortex-induced cable vibration of cable-stayed bridges at high reduced wind velocity. Journal of Wind Engineering and Industrial Aerodynamics 89(7–8), 633–647.

Nikitas, N., Macdonald, J.H.G., 2015. Aerodynamic forcing characteristics of dry cable galloping at critical Reynolds numbers. European Journal of Mechanics - B/Fluids 49, 243–249.

Nikitas, N., Macdonald, J.H.G., Andersen, T.L., 2012. Critical Reynolds number and galloping instabilities: experiments on circular cylinder. Experiments in Fluids 52, 1295–1306.

Ni, Y.Q., Wang, X.Y., Chen, Z.Q., Ko, J.M., 2007. Field observations of rain–wind-induced cable vibration in cable-stayed Dongting Lake Bridge. Journal of Wind Engineering and Industrial Aerodynamics 95, 303–328.

Ohshima, K., Nanjo, M., 1987. Aerodynamic stability of the cables of a cable-stayed bridge subject to rain (a case study of the Ajigawa Bridge). Proceedings of the Third US–Japan Bridge Workshop, Tsukuba, Japan, 324–336.

Pacheco, B.M., Fujino, Y., 1993. Keeping cables calm. Civil Engineering–ASCE 63(10), 56–58.

Pankanin, G.L., Kulinczak, A., Berlinski, J. (2007). Investigations of Karman vortex street using flow visualization and image processing. Sensors and Actuators A: Physical 138, 366–375.

Peil, U., Dreyer, O., 2007. RWIVs of cables in laminar and turbulent flow. Wind and Structures 10(1), 83–97.

Poston, R.M., 1998. Cable-stay conundrum. Civil Engineering–ASCE 68(8), 58–61.

Robertson, A.C., Taylor, I.J., Wilson, S.K., Duffy, B.R., Sullivan, J.M., 2010. Numerical simulation of rivulet evolution on a horizontal cable subject to an external aerodynamic field. Journal of Fluids and Structures 26(1), 50–73.

Saito, T., Matsumoto, M., Kitazawa, M., 1994. Rain–wind excitation of cables on cable-stayed Higashi–Kobe Bridge and cable vibration control. Proceedings of Conference on Cable-Stayed and Suspension Bridges, 507–514.

Scott Phelan, R., Sarkar, P., Mehta, K., 2006. Full-scale measurements to investigate rain–wind induced cable-stay vibration and its mitigation. Journal of Bridge Engineering, 293–304.

Seidel, C., Dinkler, D., 2006. Rain–wind-induced vibrations-phenomenology, mechanical modeling and numerical analysis. Computers & Structures 84, 1584–1595.

Taylor, I.J., Robertson, A.C., 2011. Numerical simulation of the airflow–rivulet interaction associated with the rain–wind-induced vibration phenomenon. Journal of Wind Engineering and Industrial Aerodynamics 99, 931–944.

Taylor, I.J., Robertson, A.C., 2015. Numerical investigation of the coupled interaction between an unsteady aerodynamic flow field and a water film coating on a circular cylinder. Journal of Fluids and Structures 54, 312–331.

Taylor, I.J., Robertson, A.C., Wilson, S.K., Duffy, B.R., Sullivan, J.M., 2010. New developments in rain–wind-induced vibrations of cables. Proceedings of the ICE - Structures and Buildings 163(2), 73–86.

Tokoro, S., Komatsu, H., Nakasu, M., Mizuguchi, K., Kasuga, A., 2000. A study on wake-galloping employing full aeroelastic twin cable model. Journal of Wind Engineering and Industrial Aerodynamics 88, 247–261.

Verwiebe, C., Rucheweyh, H., 1998. Recent research results concerning the exciting mechanisms of RWIVs. Journal of Wind Engineering and Industrial Aerodynamics 74–76, 1005–1013.

Wang, L.Y., Xu, L.Y., 2003. Analytical study of wind–rain-induced cable vibration: 2DOF

model. Wind and Structures 6, 291–306.

Wang, Y., Chen, Q., Zhang, B.M., 1999. Image enhancement based on equal area dualistic sub-image histogram equalization method, IEEE Transactions on Consumer Electronics 45, 68–75.

Wang, Z.J., Zhou, Y., Huang, J.F., Xu, Y.L., 2005. Fluid dynamics around an inclined cylinder with running water rivulets. Journal of Fluids and Structures 21, 49–64.

Wilde, K., Witkowski, W., 2003. Simple model of rain–wind-induced vibrations of stayed cables. Journal of Wind Engineering and Industrial Aerodynamics 91, 873–891

Williamson, C.H.K., Govardhan, R., 2008. A brief review of recent results in vortex-induced vibrations. Journal of Wind Engineering and Industrial Aerodynamics 96, 713–735.

Xia, Y., Fujino, Y., 2006. Auto-parametric vibration of a cable-stayed-beam structure under random excitation. Journal of Engineering Mechanics 132, 279–286.

Xu, Y.L., 2013. Wind Effects on Cable-Supported Bridges, John Wiley & Sons Singapore Pte. Ltd., 2 Clementi Loop, Singapore.

Xu, Y.L., Li, Y.L., Shum, K.M., Kwok, K.C.S., Hitchcock, P.A., 2006. Aerodynamic coefficients of inclined circular cylinders with artificial rivulet. Advances in Structural Engineering 9(2), 265–278.

Xu, Y.L., Wang, L.Y., 2001. Analytical study of wind–rain-induced cable vibration. Proceedings of the Fifth Asia-Pacific Conference on Wind Engineering, Kyoto, Japan, 109–112.

Xu, Y.L., Wang, L.Y., 2003. Analytical study of wind–rain-induced cable vibration: SDOF model. Journal of Wind Engineering and Industrial Aerodynamics 91, 27–40.

Yamaguchi, H., 1990. Analytical study on growth mechanism of rain vibration of cables. Journal of Wind Engineering and Industrial Aerodynamics 33(1–2), 73–80.

Yeo, D.H., Jones, N.P., 2008. Investigation on 3-D characteristics of flow around a yawed and inclined circular cylinder. Journal of Wind Engineering and Industrial Aerodynamics 96, 1947–1960.

Yeo, D.H., Jones, N.P., 2012. Aerodynamic forces induced by vertically oscillating incoming flow on a yawed horizontal circular cylinder. Journal of Wind Engineering and Industrial Aerodynamics 104–106, 188–195.

Yoshimura, T., 1992. Aerodynamic stability of four medium span bridges in Kyushu district. Journal of Wind Engineering and Industrial Aerodynamics 41, 203–213.

Zdravkovich, M.M., 1997. Flow Around Circular Cylinders, 1. Fundamentals, Oxford University Press, Oxford, UK.

Zhan, S., Xu, Y.L., Zhou, H.J., Shum, K.M., 2008. Experimental study of wind–rain-induced cable vibration using a new model setup scheme. Journal of Wind Engineering and Industrial Aerodynamics 96, 2438–2451.

Zhou, X.Q., Xia, Y., Wei, Z.L., Wu, Q.X., 2012. A videogrammetric technique for measuring the vibration displacement of stay cables. Geo-Spatial Information Science 15, 135–141.

Zuo, D.L., Jones, N.P., Main, J.A., 2008. Field observation of vortex- and rain–wind-induced

stay-cable vibrations in a three-dimensional environment. Journal of Wind Engineering and Industrial Aerodynamics 96, 1124–1133.

Zuo, D., Jones, N.P., 2010. Interpretation of field observations of wind- and rain−wind-induced stay cable vibrations. Journal of Wind Engineering and Industrial Aerodynamics 98, 73–87.